

Non-invasive hemodynamic monitoring by electrical impedance tomography

THÈSE N° 7444 (2017)

PRÉSENTÉE LE 23 FÉVRIER 2017

À LA FACULTÉ DES SCIENCES ET TECHNIQUES DE L'INGÉNIEUR
LABORATOIRE DE TRAITEMENT DES SIGNAUX 5
PROGRAMME DOCTORAL EN GÉNIE ÉLECTRIQUE

ÉCOLE POLYTECHNIQUE FÉDÉRALE DE LAUSANNE

POUR L'OBTENTION DU GRADE DE DOCTEUR ÈS SCIENCES

PAR

Martin PROENÇA

acceptée sur proposition du jury:

Dr S. Carrara, président du jury
Prof. J.-Ph. Thiran, Dr M. Lemay, directeurs de thèse
Prof. A. Adler, rapporteur
Prof. S. Rimoldi, rapporteur
Dr J.-M. Vesin, rapporteur



ÉCOLE POLYTECHNIQUE
FÉDÉRALE DE LAUSANNE

Suisse
2017

Perplexity is the beginning of knowledge.
— Khalil Gibran

To my parents and sister.

Abstract

The monitoring of central hemodynamic parameters such as cardiac output (CO) and pulmonary artery pressure (PAP) is of paramount clinical importance to assess the health status of the cardiovascular system. However, their measurement requires the insertion of a pulmonary artery catheter, a highly invasive procedure associated with non-negligible morbidity and mortality rates. In this thesis, we investigated the clinical potential of electrical impedance tomography (EIT) – a radiation-free medical imaging technique – as a non-invasive alternative for the measurement of CO and PAP.

In a first phase, we investigated the potential of EIT for the measurement of CO. This measurement is implicitly based on the hypothesis that the *EIT heart signal* (the ventricular component of the EIT signals) is induced by ventricular blood volume changes. This hypothesis has never been formally investigated, and the exact origins of the EIT heart signal remain subject to interpretation. Therefore, using a model, we investigated the genesis of this signal by identifying its various sources and their respective contributions. The results revealed that the EIT heart signal is dominated by cardioballistic effects (heart motion). However, although of prominently cardioballistic origin, the amplitude of the signal has shown to be strongly correlated to stroke volume ($r = 0.996$, $p < 0.001$; error of 0.57 ± 2.19 mL). We explained these observations by the quasi-incompressibility of myocardial tissue and blood. We further identified several factors and conditions susceptible to affect the accuracy of the measurement. Finally, we investigated the influence of the EIT sensor belt position on the measured heart signal. We observed that small belt displacements – likely to occur in clinical settings during patient handling – can induce errors of up to 30 mL on stroke volume estimation.

In a second phase, we investigated the feasibility of a novel method for the non-invasive measurement of PAP by EIT. The method is based on the physiological relation linking the PAP to the velocity of propagation of the pressure waves in the pulmonary arteries. We hypothesized that the variations of this velocity, and therefore of the PAP, could be measured by EIT. In a bioimpedance model of the human thorax, we demonstrated the feasibility of our method in various types of pulmonary hypertensive disorders. Our EIT-derived parameter has shown to be particularly well-suited for predicting early changes in pulmonary hemodynamics due to its physiological link with arterial compliance. Finally, we validated experimentally our method in 14 subjects undergoing hypoxia-induced PAP changes. Significant correlation coefficients ($r \in [0.70, 0.98]$, average: 0.89) and small standard errors of the estimate ($SEE \in [0.9, 6.3]$ mmHg, average: 2.4 mmHg)

were found between our EIT-derived systolic PAP and reference systolic PAP values obtained by Doppler echocardiography.

In conclusion, there is a promising outlook for EIT in non-invasive hemodynamic monitoring. Our observations provide novel insights for the interpretation and understanding of EIT heart signals, and detail the physiological and metrological requirements for an accurate measurement of CO by EIT. Our novel PAP monitoring method, validated *in vivo*, allows a reliable tracking of PAP changes, thereby paving the way towards the development of a new branch of non-invasive hemodynamic monitors based on the use of EIT.

Keywords: non-invasive hemodynamic monitoring, electrical impedance tomography, cardiac output, pulmonary artery pressure, cardiovascular diseases.

Résumé

Le monitoring de paramètres hémodynamiques centraux tels que le débit cardiaque (DC) et la pression artérielle pulmonaire (PAP) est d'une importance clinique primordiale pour évaluer l'état du système cardiovasculaire. Cependant, leur mesure nécessite l'insertion d'un cathéter artériel pulmonaire, une procédure hautement invasive et associée à des taux de morbidité et mortalité non-négligeables. Dans cette thèse, nous avons étudié le potentiel clinique de la tomographie d'impédance électrique (TIE) – une technique d'imagerie médicale sans radiation – comme alternative non-invasive pour la mesure du DC et de la PAP.

Dans un premier temps, nous avons étudié le potentiel de la TIE pour la mesure du DC. Cette mesure est implicitement basée sur l'hypothèse selon laquelle le signal TIE du coeur (la composante ventriculaire des signaux TIE) est induit par des changements de volume sanguin ventriculaire. Cette hypothèse n'a jamais été formellement examinée, et les origines exactes du signal TIE du coeur demeurent, à ce jour, sujettes à interprétation. Pour cette raison, au moyen d'un modèle, nous avons étudié la genèse de ce signal en identifiant ses diverses sources et leurs contributions respectives. Les résultats ont révélé que le signal TIE du coeur est dominé par des effets cardiobalistiques (mouvements cardiaques). Cependant, bien que principalement d'origine cardiobalistique, l'amplitude du signal s'est montrée fortement corrélée au volume d'éjection systolique ($r = 0.996$, $p < 0.001$; erreur de 0.57 ± 2.19 mL). Nous avons expliqué ces résultats par la quasi-incompressibilité du tissu du myocarde et du sang. Nous avons également identifié plusieurs facteurs et pathologies susceptibles d'affecter la précision de la mesure. Enfin, nous avons étudié l'influence de la position de la ceinture de TIE sur le signal cardiaque mesuré. Nous avons observé que de petits déplacements de la ceinture – probables en milieu clinique lors de la manutention du patient – peuvent produire des erreurs allant jusqu'à 30 mL sur l'estimation du volume d'éjection systolique.

Dans un second temps, nous avons étudié la faisabilité d'une nouvelle méthode pour la mesure non-invasive de la PAP par TIE. La méthode se base sur la relation physiologique liant la PAP à la vitesse de propagation des ondes de pression dans les artères pulmonaires. Nous avons fait l'hypothèse que les variations de cette vitesse, et donc de la PAP, peuvent être mesurées par TIE. Nous avons démontré la faisabilité de notre méthode dans un modèle de bio-impédance du thorax humain pour divers types d'hypertensions pulmonaires. Le paramètre que nous estimons par TIE s'est montré particulièrement bien adapté pour la prédiction de changements précoces dans l'hémodynamique pulmonaire,

en raison de son lien physiologique à la compliance artérielle. Enfin, nous avons validé expérimentalement notre méthode dans 14 sujets soumis à des variations de PAP induites par hypoxie. Des coefficients de corrélation significatifs ($r \in [0.70, 0.98]$, moyenne : 0.89) et des erreurs-types d'estimation petites ($S_e \in [0.9, 6.3]$ mmHg, moyenne : 2.4 mmHg) ont été obtenus entre nos estimations de PAP systolique et les valeurs de PAP systolique de référence obtenues par échocardiographie Doppler.

En conclusion, les perspectives de la TIE pour le monitoring hémodynamique non-invasif sont prometteuses. Nos observations apportent de nouveaux éléments quant à l'interprétation et la compréhension des signaux TIE du coeur, et détaillent les conditions physiologiques et métrologiques nécessaires à une mesure précise du DC par TIE. Notre nouvelle méthode de monitoring de la PAP, validée *in vivo*, permet un suivi fiable des variations de PAP, ouvrant ainsi la voie au développement d'une nouvelle branche de moniteurs hémodynamiques non-invasifs basés sur l'utilisation de la TIE.

Mots-clefs : monitoring hémodynamique non-invasif, tomographie d'impédance électrique, débit cardiaque, pression artérielle pulmonaire, maladies cardiovasculaires.

Remerciements

Une thèse ne s’accomplit jamais seul. J’aimerais donc profiter de ces quelques lignes pour remercier chaleureusement ceux qui m’ont guidé et soutenu tout au long du chemin.

- En premier lieu, je tiens à remercier mon superviseur à l’EPFL, Prof. Jean-Philippe Thiran, sans qui cette thèse n’aurait tout simplement pas pu se faire. Après m’avoir déjà supervisé pour mon projet de Master – déjà dans le domaine de l’EIT –, tu m’as renouvelé ta confiance pour quatre années de plus. Cette confiance, tu me l’as accordée en acceptant ce concept de “thèse à distance”, me permettant ainsi de réaliser mes recherches dans le monde industriel avec une liberté de recherche difficilement égalable. Un grand merci, Jean-Philippe !
- J’aimerais ensuite remercier mon superviseur au CSEM, Dr Mathieu Lemay. Je ne pense pas qu’il soit donné à tous les thésards de pouvoir avoir des liens aussi amicaux et une relation de travail aussi bonne avec leur superviseur. Des conseils avisés, une rigueur scientifique, des discussions et des commentaires directs et (presque) toujours constructifs (“Tes figures sont moches”). Le tout arrosé d’une fine couche d’humour et de bonne humeur. Merci Mathieu. Mais ne va pas croire que ces remerciements effacent la dette de 149’999 burgers que tu me dois encore. Un pari est un pari.
- Les médecins Prof. Stefano Rimoldi, Dr méd. Emrush Rexhaj et PD Dr méd. Thomas Riedel à l’Inselspital (Berne) pour m’avoir ouvert les portes du monde clinique et permis d’enregistrer de précieuses données. Un merci tout particulier à Emrush pour sa patience et son optimisme indéfectibles.
- Je tiens également à remercier Prof. Andy Adler (Université Carleton, Canada) – une véritable référence dans le domaine de l’EIT – pour son aide et ses conseils précieux : une vraie machine à générer des idées et des solutions. Merci Andy !
- Merci également aux Dr Sandro Carrara et Dr Jean-Marc Vesin (EPFL) pour avoir accepté de se porter membres du jury de ma thèse.
- Un grand merci aussi au Dr Philippe Reymond (EPFL) pour m’avoir permis d’utiliser ses modèles anatomique et circulatoire des larges artères pulmonaires.
- Merci enfin aux diverses personnes avec lesquelles j’ai eu l’occasion de collaborer au cours de ma thèse, notamment pour l’acquisition de données EIT et IRM. Je pense

Acknowledgements

en particulier au Prof. Fernando Suárez-Sipmann (Université d'Uppsala, Suède), Dr méd. Stephan Böhm et Peter Krammer (Swisstom AG, Landquart), Dr Bartłomiej Grychtol (PAMB-Fraunhofer, Allemagne) et Dr Martin Bühler (ETHZ).

Je voudrais ensuite remercier toute "l'équipe" du CSEM, tous ceux qui de près ou de loin m'ont permis de réaliser ma thèse dans une ambiance vraiment exceptionnelle.

- Mon chef, Dr Mattia Bertschi, pour m'avoir permis de réaliser mes recherches dans des conditions de travail optimales, avec son lot – toujours bienvenu ! – de projets hors-thèse pour "se changer les idées". Merci Mattia !
- Mon "compagnon de route", (soon-to-be-Dr) Fabian Braun, pour nos longues heures de cogitation, de perplexité, de hauts, de bas, d'échanges d'idées, de questionnements, et surtout d'entraide. Un énorme merci, Fabuuu !
- Mon catalan préféré, Dr Josep Solà, pour ses désormais fameuses "piqûres de motivation", son aide et ses conseils ô combien précieux, et ses connaissances infaillibles de la physiologie cardiovasculaire. Gràcies Josep !
- Mes collègues Dr Philippe Renevey, (soon-to-be-Dr) Michael Rapin et Dr Ricard Delgado-Gonzalo, pour leurs contributions, sous diverses formes, allant du simple conseil aux explications techniques, en passant par la relecture de certains passages.
- Et de manière générale, un gros merci à tous mes collègues de bureau / de café (dédicace spéciale à Stephan Dasen), qui avec leurs encouragements ("Tu finis quand ta thèse ?") et leur humour, ont toujours su me redonner du punch quand la motivation venait à manquer.

Et finalement, un merci tout particulier à ma famille : à ma mère Nicole et ma soeur Inès, pour leur soutien indéfectible, et à mon père José, parti trop tôt, mais non sans avoir éveillé en moi la fibre scientifique.

Neuchâtel, le 2 novembre 2016

Martin

Contents

I	Introduction and background	1
1	Introduction	3
1.1	Motivation and problem statement	3
1.1.1	Monitoring of hemodynamic parameters	3
1.1.2	Pulmonary artery catheter: benefits and risks	3
1.1.3	Clinical need for non-invasive alternatives	4
1.1.4	Non-invasive monitoring by electrical impedance tomography	5
1.2	Objectives	6
1.3	Organization of the manuscript	6
2	Concepts on cardiovascular physiology	7
2.1	Overview of the cardiovascular system	7
2.2	Key cardiovascular parameters	9
2.2.1	Blood pressure	9
2.2.2	Cardiac output	9
2.2.3	Vascular resistance	9
2.2.4	Vascular compliance	10
2.2.5	Regulation aspects of the systemic circulation	11
2.3	Particularities of the pulmonary circulation	13
2.3.1	Factors influencing pulmonary vascular resistance	13
2.3.2	Consequences of a well-distributed pulmonary vascular compliance	13
2.4	Cardiovascular pathologies	16
2.4.1	Circulatory shock	17
2.4.2	Pulmonary hypertension	19
2.5	Pulse wave velocity	24
2.5.1	Relation to arterial stiffness and compliance	24
2.5.2	Clinical significance	25
2.5.3	Typical values	25
2.5.4	Measurement principle	26

Contents

3	State of the art in cardiovascular monitoring techniques	29
3.1	Cardiac output	29
3.1.1	Gold standards	29
3.1.2	Partial rebreathing methods	29
3.1.3	Pulse contour methods	30
3.1.4	Ultrasound methods	31
3.1.5	Impedance-based methods	31
3.1.6	Limitations of current CO monitoring techniques	32
3.2	Pulmonary artery pressure	32
3.2.1	Gold standard	32
3.2.2	Implantable hemodynamic monitors	33
3.2.3	Ultrasound methods	33
3.2.4	Phonocardiography-based methods	34
3.2.5	Limitations of current PAP monitoring techniques	34
4	Concepts on electrical impedance tomography	35
4.1	Thoracic imaging by EIT	35
4.1.1	Working principle	35
4.1.2	Factors affecting thoracic bioimpedance	36
4.1.3	Separation of the respiratory- and cardiovascular-related components	36
4.2	EIT for bedside monitoring of the cardiorespiratory system	36
4.2.1	Current situation and challenges	36
4.2.2	Clinical outlook	37
4.3	Technical aspects of EIT	38
4.3.1	Measurement of bioimpedance	38
4.3.2	Stimulation and measurement patterns	39
4.3.3	Image reconstruction	40
4.4	Commercially available EIT systems	44
II	Cardiac output by electrical impedance tomography	47
5	Influence of heart motion on the EIT-based measurement of CO	49
5.1	Introduction	50
5.1.1	Objectives	50
5.1.2	Measurement principle and study goal	50
5.2	Methods	52
5.2.1	Influence of heart motion: three scenarios	52
5.2.2	Dynamic bioimpedance model creation	53
5.2.3	EIT simulations	57
5.2.4	Automatic extraction of $\Delta\sigma$ in EIT image sequences	58
5.2.5	Simulated SV values	58

5.2.6	Analysis protocol	59
5.3	Results	59
5.3.1	Contribution of heart motion to the genesis of $\Delta\sigma$ (Analysis 1) . .	61
5.3.2	Impact of heart motion on the morphology of $\Delta\sigma$ (Analysis 2) . .	61
5.3.3	Impact of heart motion on EIT-based SV estimation (Analysis 3) .	61
5.4	Discussion	63
5.4.1	Contribution of heart motion to the genesis of $\Delta\sigma$	63
5.4.2	Impact of heart motion on the morphology of $\Delta\sigma$	63
5.4.3	Impact of heart motion on EIT-based SV estimation	64
5.4.4	Implications of our observations	64
5.4.5	Limitations and future work	65
5.4.6	Summary and conclusion	66
6	Influence of belt position and displacement on the EIT-based measurement of CO	69
6.1	Introduction	71
6.2	Methods	72
6.2.1	Thoracic bioimpedance model	72
6.2.2	Bioimpedance simulations and EIT reconstruction	72
6.2.3	Analysis protocol	73
6.3	Results	74
6.3.1	Sources contributing to $\Delta\sigma$	75
6.3.2	Influence of belt displacement on EIT-based SV estimation	75
6.4	Discussion	75
III	Pulmonary artery pressure by electrical impedance tomography	77
7	Model-based feasibility study on the EIT-based measurement of PAP	79
7.1	Introduction	80
7.1.1	Objectives	80
7.1.2	Measurement principle	80
7.1.3	Previous work and study goal	81
7.2	Methods	81
7.2.1	Thoracic bioimpedance model	82
7.2.2	Simulation of pathologies	90
7.2.3	EIT simulations and PTT estimation	96
7.3	Results	99
7.4	Discussion	100
7.4.1	EIT-based PAP monitoring	100
7.4.2	Model assumptions validity, limitations, and future work	102
7.4.3	Summary and conclusion	104

Contents

8	Experimental study on the EIT-based measurement of PAP	105
8.1	Introduction	106
8.1.1	Objectives	106
8.1.2	Measurement principle	106
8.2	Materials and methods	106
8.2.1	Subjects and experimental protocol	106
8.2.2	Echocardiographic measurements	108
8.2.3	EIT measurements and image reconstruction	108
8.2.4	EIT data processing	109
8.3	Results	109
8.3.1	EIT data processing	109
8.3.2	EIT-based PAP monitoring	110
8.4	Discussion	112
8.4.1	Unsupervised and non-invasive PAP monitoring	112
8.4.2	Limitations and future work	120
8.4.3	Summary and conclusion	120
IV	Conclusions	123
9	Synthesis	125
9.1	On the EIT-based monitoring of cardiac output	125
9.1.1	Influence of heart motion	125
9.1.2	Influence of belt position and displacement	126
9.1.3	Summary	127
9.2	On the EIT-based monitoring of pulmonary artery pressure	127
9.2.1	Feasibility of a novel non-invasive method	127
9.2.2	<i>In vivo</i> evaluation	128
9.2.3	Summary	129
9.3	Perspectives in intensive care units	130
9.4	Original contributions	130
9.5	Limitations and future work	131
9.5.1	EIT-based CO monitoring	131
9.5.2	EIT-based PAP monitoring	132
9.6	Conclusion	133
A	Anatomical and circulatory models of the pulmonary arterial tree	135
A.1	Anatomical model	135
A.1.1	Volume-filling branching algorithm	135
A.1.2	Geometry and morphometry of the tree	136
A.2	Circulatory models	137
A.2.1	Non-linear model for the large arteries	138
A.2.2	Linear model for the small arteries	140

Bibliography	159
Curriculum Vitae and publication list	161

List of Figures

1.1	Pulmonary artery catheter inserted into the pulmonary arteries	4
2.1	Schematic representation of the cardiovascular system	8
2.2	Regulation of arterial blood pressure	12
2.3	Pressure-flow relationship in the systemic and pulmonary circulations	14
2.4	Relationship between pulmonary vascular resistance and lung volume	14
2.5	Relationship between pulmonary vascular resistance and compliance	16
2.6	Relationship between mean pulmonary artery pressure and pulmonary pulse wave velocity	26
2.7	Measurement of the pulmonary pulse transit time	27
4.1	Conductivity changes measured by EIT in a healthy subject	37
4.2	Concept of bedside EIT monitoring	38
4.3	Path of electrical currents through a suspension of cells	39
4.4	Adjacent stimulation and measurement pattern: example for a 16-electrode configuration	40
5.1	Rationale for CO monitoring by EIT	51
5.2	Overview of the simulation and analysis process for CO by EIT	52
5.3	Segmented frame of the 2.5D dynamic model and reference MRI-derived left ventricular volume	54
5.4	Segmented ventricular region in MRI scans	55
5.5	Mesh of the 2.5D dynamic bioimpedance model	56
5.6	Pulmonary and aortic conductivity changes over the cardiac cycle	57
5.7	Automatic segmentation of the ventricular region in EIT images	58
5.8	Examples of reconstructed EIT images at end systole	60
5.9	Left ventricular volume estimation from $\Delta\sigma$	62
5.10	Stroke volume estimation from $\Delta\sigma_{\max}$	62
5.11	Conductivity change in the heart region between end diastole and end systole	64
6.1	4D thoracic bioimpedance model (all belts)	73
6.2	RMS images when simulating all structures or the lungs only	74

List of Figures

7.1	Measurement principle of the pulmonary pulse transit time by EIT	81
7.2	4D thoracic bioimpedance model (transversal belt)	83
7.3	Radius of all generated arterial segments in the left pulmonary tree as a function of their order	84
7.4	Length of all generated arterial segments in the left pulmonary tree as a function of their order	85
7.5	Number of generated arterial segments in the left pulmonary tree as a function of their order	85
7.6	Anatomical model of the pulmonary arterial tree	86
7.7	Structure of the global circulatory model of the pulmonary circulation .	87
7.8	Schematic representation of the pulmonary arterial tree, by analogy with electrical circuits	89
7.9	Assessment of the volume fraction of extra-capillary blood vessels in each pulmonary voxel	91
7.10	Example of reconstructed EIT frame	97
7.11	Overview of the pulmonary pulse transit time estimation method	98
7.12	EIT-derived pulmonary PTT for different levels of PAP and for different pathologies.	99
7.13	Example of a pressure wave propagating through the arterial tree and its corresponding average EIT signal in the pulmonary ROI	100
7.14	Example of distal pressure waveforms and their corresponding average EIT signals in the pulmonary ROI	101
8.1	Overview of the experimental protocol for PAP estimation by EIT	107
8.2	Experimental setup for PAP estimation during induced hypoxia	107
8.3	Experimental protocol for inducing PAP variations	108
8.4	ECG-gated ensemble averaging of EIT signals	110
8.5	Examples of EIT ensemble average signals in the lung and heart regions	111
8.6	Examples of maps depicting the pixel-wise modulus and phase shift of the first cardiac harmonic	111
8.7	Examples of pulse arrival time estimation in EIT pulmonary signals . . .	112
8.8	EIT-based PAP monitoring: subject-wise experimental results	116
8.9	EIT-based PAP monitoring: global experimental results	117
9.1	Perspectives of EIT in intensive care units for hemodynamic monitoring	129
A.1	Schematic illustration of the volume-filling branching algorithm	136
A.2	Model of a non-tapering arterial segment and its electrical analog	138
A.3	Model of a large arterial segment (tapering tube)	139
A.4	Boundary conditions for 1D distributed parameter models	140
A.5	Electrical representation of the 3-element Windkessel model	140

List of Tables

2.1	Hemodynamic definitions of pulmonary hypertension	20
4.1	Commercial EIT systems	45
5.1	Conductivity value of tissues at 100 kHz	56
5.2	Simulated SV values	61
7.1	Normal and pathology-specific values of the hemodynamic parameters of the model	93
8.1	EIT-based PAP monitoring: experimental results for all subjects	118

List of Acronyms

BP	Blood pressure
BR	Breath rate
CO	Cardiac output
CTEPH	Chronic thromboembolic pulmonary hypertension
CVP	Central venous pressure
ECG	Electrocardiogram/-ph/-phy
EIT	Electrical impedance tomography
HAPE	High-altitude pulmonary edema
HPV	Hypoxic pulmonary vasoconstriction
HR	Heart rate
ICG	Impedance cardiography
ICU	Intensive care unit(s)
LVV	Left ventricular volume
MAD	Median absolute deviation
MAP	Mean arterial pressure
MRI	Magnetic resonance imaging
PAC	Pulmonary artery catheter
PAH	Pulmonary arterial hypertension
PAP	Pulmonary artery pressure
PAT	Pulse arrival time
PEP	Pre-ejection period
PH	Pulmonary hypertension
PH-LHD	Pulmonary hypertension due to left heart disease
PSNS	Parasympathetic nervous system
PTT	Pulse transit time
PP	Pulse pressure
PWV	Pulse wave velocity
RAP	Right atrial pressure
ROI	Region of interest
SNR	Signal-to-noise ratio
SNS	Sympathetic nervous system
SPAP	Systolic pulmonary artery pressure
SpO ₂	Peripheral capillary oxygen saturation

List of Tables

SV	Stroke volume
TR	Tricuspid regurgitation
VTI	Velocity time integral

Introduction and background **Part I**

1 Introduction

1.1 Motivation and problem statement

1.1.1 Monitoring of hemodynamic parameters

The circulation of blood in the body is vital. This function is performed by the *cardiovascular system*, which comprises the heart and blood vessels. Similarly to an hydraulic circuit controlled by parameters such as pressure and flow rate, the cardiovascular system is governed by so-called *hemodynamic* parameters (from Greek *haima*, “blood”, and *dynamis*, “power”). Being able to reliably measure hemodynamic parameters is therefore of paramount clinical importance to assess the health of the cardiovascular system. However, since most hemodynamic parameters are *central* (as opposed to *peripheral*), their measurement often represents a great technical challenge. In particular, the measurement of parameters such as *cardiac output* (CO) or *pulmonary artery pressure* (PAP) still requires, to this day, a highly invasive procedure known as right heart catheterization, which consists in the insertion of a so-called *pulmonary artery catheter* (PAC) into the pulmonary arteries via the right cardiac chambers (Figure 1.1).

1.1.2 Pulmonary artery catheter: benefits and risks

Introduced in 1970 [162] and commercialized soon after, the PAC quickly became extensively used in operating rooms and intensive care units, not only as a diagnostic tool, but also for the determination and guidance of therapy in critically ill and hemodynamically unstable patients [38, 107]. However, in 1996, a prospective cohort study by Connors *et al* [34] in 5,735 patients demonstrated a 24 % increased 30-day mortality in patients who underwent right heart catheterization during the first 24 hours of care in an intensive care unit, in comparison with non-catheterized patients. Their findings were further confirmed over the next decade, when several randomized control trials failed to demonstrate any decrease in morbidity and mortality following the use of

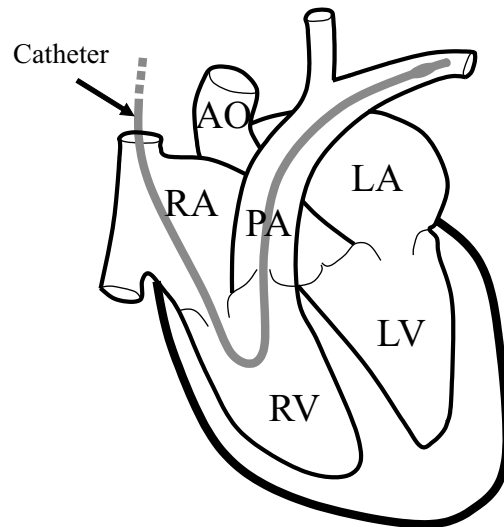


Figure 1.1 – Pulmonary artery catheter inserted into the pulmonary arteries via the right cardiac chambers for the measurement of central hemodynamic parameters such as CO and PAP. RA: right atrium; RV: right ventricle; LA: left atrium; LV: left ventricle. PA: pulmonary artery; AO: aorta. Adapted from [86].

the PAC in critically ill and hemodynamically unstable patients [67, 143, 147]. The risks associated with the insertion and maintenance of the PAC (*e.g.* pulmonary artery rupture), as well as measurement inaccuracies (particularly for CO) and the difficulty for the clinicians to correctly interpret the data measured, are some of the explanations that have been proposed to interpret these outcomes [107]. Since then, the use of the PAC has been strongly reduced and right heart catheterization is only performed when the benefits/safety ratio is considered clearly favorable by the clinicians.

1.1.3 Clinical need for non-invasive alternatives

The controversy associated with the use of the PAC has paved the way for the introduction of non-invasive alternative solutions to monitor central hemodynamics, in particular for CO and PAP.

For instance, although non-invasive continuous CO monitors generally cannot provide absolute values, they are of particular importance in events of circulatory shock – a common and potentially fatal condition affecting about one third of patients in intensive care units – where beat-to-beat *trends* in CO (rather than absolute values) have a strong impact for guiding and optimizing the therapy [106, 169]. Continuous CO monitors are also useful as complementary solutions to the PAC, by providing beat-to-beat readings in-between PAC measurements, possibly using the latter for intermittent recalibration [36, 131]. However, the reliability of current non-invasive beat-to-beat CO

1.1. Motivation and problem statement

monitors is strongly limited by their sensitivity to physiological phenomena unrelated to CO, thus requiring frequent recalibration maneuvers, whenever changes in the patient's hemodynamic status may have occurred [91, 131, 177].

For monitoring PAP, the PAC remains the only solution for reliable beat-to-beat measurement. Non-invasive and continuous PAP monitors could therefore prove themselves particularly useful, for instance in patients undergoing acute changes in pulmonary hemodynamics but for whom the placement of a PAC was not indicated. Furthermore, in patients requiring right heart catheterization, such devices would allow extending the monitoring after removal of the PAC, as the latter should be left in place as briefly as possible to minimize the risks of complications [38, 184]. In patients with chronic pulmonary hypertension (sustained and abnormally elevated PAP), a condition affecting at least 0.3 % of the general population [160] and more than 60 % of patients with moderate or severe heart failure [58], reliable non-invasive means of assessing changes in PAP at regular intervals of days or weeks have shown to improve patient outcomes and allow anticipating worsening conditions, as increases in PAP occur days or weeks before the onset of symptoms [1, 111]. However, the currently existing reliable and non-invasive PAP measuring techniques – based on Doppler ultrasounds – are unsuited for frequent or continuous monitoring. They depend on medical doctors to perform the measurement and are inapplicable in 20–50 % of patients due to unmeasurable tricuspid regurgitation [37, 40].

In summary, reliable and non-invasive solutions for the continuous monitoring of CO and PAP are currently still lacking.

1.1.4 Non-invasive monitoring by electrical impedance tomography

Electrical impedance tomography (EIT) is a non-invasive and radiation-free medical imaging technique for continuous monitoring at the bedside [73]. The main strength of EIT resides in its ability to monitor changes in the intra-thoracic distribution of electrical impedance with a high time resolution. In particular, impedance changes induced by respiratory and cardiovascular activity (*e.g.* changes in air volume in the lungs or in blood volume in the heart) can be monitored in real-time, providing valuable functional information about the cardiorespiratory system.

Significant advances have been achieved in EIT research in recent years, in particular for the monitoring and guidance of mechanical ventilation [6, 51, 52]. In parallel, over the last two decades, the clinical potential of EIT for the monitoring of central hemodynamic parameters has been a growing focus of attention [104, 120, 129, 157]. For instance, changes in blood volume during ventricular ejection have shown to produce variations in EIT images in the heart region, suggesting the possibility of tracking changes in CO [129, 174]. Similarly, changes in the pulsatility of the pulmonary arteries have shown

Chapter 1. Introduction

to produce variations in EIT images in the pulmonary region, suggesting the possibility of assessing PAP-related information [155].

In this context, the purpose of the present thesis is to investigate the clinical potential of EIT as a hemodynamic monitor for the non-invasive measurement of CO and PAP.

1.2 Objectives

More specifically, the present thesis aims at fulfilling the following objectives:

- a) To determine the influence of heart motion on the accuracy of the EIT-based measurement of CO;
- b) To determine the influence of sensor belt position and displacement on the accuracy of the EIT-based measurement of CO;
- c) To propose and determine the feasibility of a novel method for the EIT-based measurement of PAP;
- d) To validate and determine the accuracy of the proposed method for the EIT-based measurement of PAP *in vivo*.

1.3 Organization of the manuscript

This manuscript is organized into four parts. Part I introduces the problem and motivation behind the present thesis (Chapter 1), as well as the physiological (Chapter 2) and technical (Chapters 3 and 4) background related to it. Part II investigates, via simulations, the accuracy of EIT-based CO estimation, while quantifying the influence of heart motion (Chapter 5) and EIT sensor position and displacement on the measurement (Chapter 6). Part III proposes a novel method to estimate the PAP by EIT, evaluates it in various forms of pulmonary hypertension via simulations (Chapter 7), and validates it experimentally *in vivo* (Chapter 8). Finally, Part IV concludes this dissertation with a synthesis and suggestion of future work (Chapter 9). In Appendix A, models relevant to the work performed in this thesis are described.

2 Concepts on cardiovascular physiology

The purpose of this chapter is to provide an overview of the physiological concepts related to the work performed during this thesis.

2.1 Overview of the cardiovascular system

The cardiovascular system is a circulatory system comprising the heart and the blood vessels (Figure 2.1). It can be divided into two circulations: the *systemic* circulation, perfused by the left heart, and the *pulmonary* circulation, perfused by the right heart.

The systemic circulation receives oxygenated blood from the pulmonary circulation and transports it (along with other substances, such as nutrients and hormones) from the left heart to the peripheral tissues of the body (organs and muscles) via the systemic arteries. The oxygen is then *diffused* from the blood into the tissues via the systemic capillaries. Conversely, metabolic waste products (such as carbon dioxide) are diffused from the tissues into the blood. The partly deoxygenated blood then returns to the heart via the systemic veins.

The pulmonary circulation receives partly deoxygenated blood from the systemic circulation and transports it from the right heart to the lungs via the pulmonary arteries. Oxygen brought by respiration into the pulmonary alveoli is then diffused into the blood via the pulmonary capillaries. Conversely, carbon dioxide is diffused from the blood into the alveoli in order to be expelled. The reoxygenated blood returns to the heart via the pulmonary veins and reenters the systemic circulation.

Understanding the circulatory aspects of the cardiovascular system requires introducing the key parameters that control it from a hemodynamic viewpoint: blood pressure, cardiac output, vascular resistance, and vascular compliance.

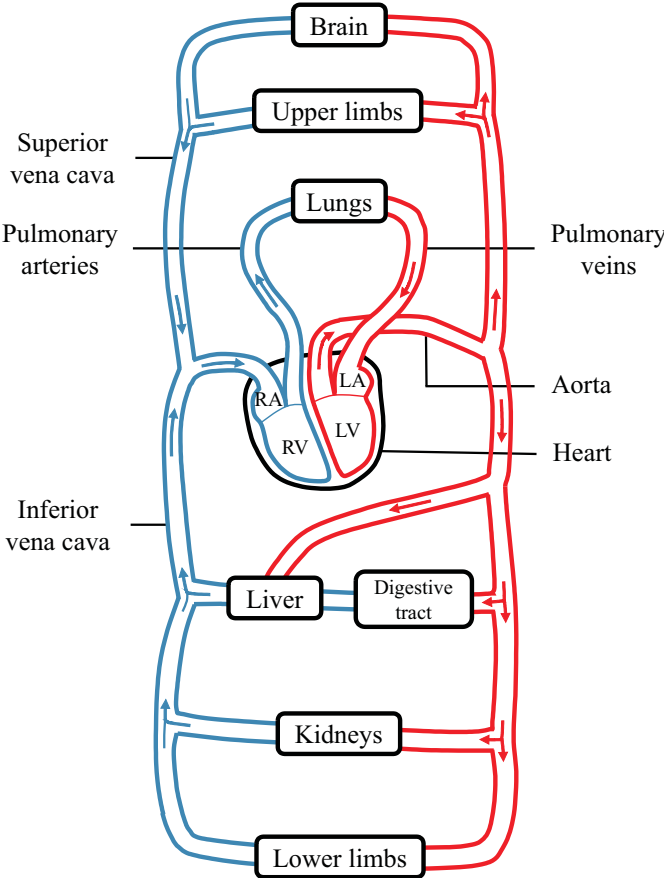


Figure 2.1 – Schematic representation of the cardiovascular system. The arrows indicate the direction of blood flow. The left ventricle (LV) pumps oxygenated blood (red color) via the aorta into the systemic circulation. After its passage through the systemic capillaries, the partly deoxygenated blood (blue color) returns to the heart via the venae cavae. It is then pushed by the right atrium (RA) into the right ventricle (RV), before being expelled towards the lungs via the pulmonary arteries. After its passage through the pulmonary capillaries, the reoxygenated blood returns to the heart via the pulmonary veins. It is then pushed by the left atrium (LA) into the LV, and the whole cycle starts again. Adapted from [97].

2.2 Key cardiovascular parameters

2.2.1 Blood pressure

From a hemodynamic viewpoint, the heart works as a cyclic pump: the ventricles eject blood during *systole* and refill during *diastole*. Arterial blood pressure (BP) is therefore *pulsatile*, and is usually expressed in terms of its systolic (maximum) and diastolic (minimum) values. In a resting adult, BP oscillates between ~ 120 mmHg and ~ 80 mmHg, conventionally written 120/80 mmHg [97]. BP is commonly expressed in millimeters of mercury ($1 \text{ mmHg} \approx 133 \text{ Pa}$) and relative to atmospheric pressure (760 mmHg): thus a BP of 100 mmHg is 100 mmHg *above* atmospheric pressure. In the pulmonary arteries, BP is commonly referred to as pulmonary artery pressure (PAP) and is much lower than systemic BP (approximately by a 7-fold factor) [97]. In a resting adult, a normal value for PAP is typically 21/9 mmHg [88].

2.2.2 Cardiac output

In the large veins, BP is close to atmospheric pressure and therefore a gradient of pressure exists between the arterial and venous trees and allows the blood to flow. At each heartbeat, the small amount of blood ejected by each ventricle into the arteries – the so-called stroke volume (SV) – is driven by this pressure gradient from the arteries down to the capillaries and the veins, and back to the heart. Cardiac output (CO) is defined as the amount of blood ejected by one ventricle in one minute. Thus, CO is the product of SV and heart rate (HR), and is commonly expressed in liters per minute (L/min):

$$\text{CO} = \text{SV} \cdot \text{HR}. \quad (2.1)$$

In a resting adult, a normal value for CO is typically 4-7 L/min [97]. As the systemic and pulmonary circulations form a closed-loop system, CO is virtually equal in both circulations.

2.2.3 Vascular resistance

BP and CO are related through the concept of *vascular resistance*. By analogy with Ohm's law in electrical circuit theory (resistance equals voltage divided by current), the resistance R opposing the flow between two locations in the vasculature is:

$$R = \frac{\Delta P}{\text{CO}}, \quad (2.2)$$

where ΔP is the mean pressure gradient between both locations. When involving

Chapter 2. Concepts on cardiovascular physiology

central and global parameters in equation (2.2), we find one of the main relations of the cardiovascular system:

$$\text{MAP} = \text{CO} \cdot R_t + \text{CVP}, \quad (2.3)$$

where MAP stands for mean arterial pressure (the mean component of BP), CVP stands for central venous pressure, and R_t for total vascular resistance.

Through Poiseuille's law, vascular resistance in a vessel of radius r and length l is known to be proportional to l/r^4 , and thus mainly to $1/r^4$ [180]. Therefore resistance is low in large vessels, and becomes exponentially larger as the vessels narrow. In the systemic circulation, the large arteries only account for $\sim 2\%$ of R_t , whereas $\sim 60\%$ of R_t is due to the smallest arteries and the arterioles (often called, quite pertinently, resistance vessels) [97]. In the pulmonary circulation, this effect is less marked and R_t is much lower ($\sim 1/7$ th of systemic), hence the aforementioned 7-fold factor between systemic BP and PAP [97, 121]. This lower pulmonary R_t is due to the fact that pulmonary vessels are shorter and wider than their systemic counterparts (thus l/r^4 is smaller) [97].

The relation between pressure and flow in the cardiovascular system is of course more complex than equation (2.2) or (2.3), which only accounts for their average values. Both pressure and flow are pulsatile, and their relation is governed by equations of fluid dynamics (see Section A.2). A key parameter in their relation is *vascular compliance*.

2.2.4 Vascular compliance

If the arteries were perfectly rigid, blood flow would drop to zero during diastole as the heart only ejects blood during systole. This potential problem is avoided thanks to the distension capability, or *distensibility*, of the arteries, caused by the presence of a protein known as elastin in their wall [180]. By distending when subjected to a local pressure increase ΔP , the arteries allow the temporary storage of a small volume of blood ΔV [97]. As elastin stores mechanical energy (tension) when stretched, arterial BP does not drop to zero during diastole as it does in the ventricles; it keeps driving the blood towards the periphery. This *capacitive* capability of the arteries (by analogy with capacitors in electrical circuits), or blood vessels in general, is precisely what vascular compliance (C) characterizes:

$$C = \frac{\Delta V}{\Delta P}. \quad (2.4)$$

When involving central and global parameters in equation (2.4), we find a second

important relation of the cardiovascular system:

$$\begin{aligned} \text{PP} &= \frac{\text{SV} - V_{\text{runoff}}}{C_t} \\ &\approx \frac{\text{SV}}{C_t}, \end{aligned} \tag{2.5}$$

where PP is the pressure pulse (the pulsatility-related component of BP, defined as systolic minus diastolic BP), V_{runoff} is the volume of blood drained away during ejection, and C_t is total vascular compliance [97]. In the systemic arterial tree, $\sim 80\%$ of C_t is provided by the aorta alone [149]. The systemic arteries become increasingly stiffer and muscular as one moves away from the heart. Conversely, the pulmonary arteries do not exhibit increased stiffness between central and peripheral sites [121]. Pulmonary arterial compliance is distributed over the entire tree [149]. This particularity stands at the basis of several remarkable characteristics of the pulmonary circulation, as will later be seen in Section 2.3.

2.2.5 Regulation aspects of the systemic circulation

Figure 2.2 illustrates the mechanisms involved in the regulation of arterial BP and the various parameters related to it.

As seen from equations (2.3) and (2.5), one of the main factors affecting the regulation of BP is CO, and therefore HR and SV. HR is controlled by the autonomic nervous system, which is subdivided into the sympathetic nervous system (SNS) and the parasympathetic nervous system (PSNS). Activation of the SNS increases HR, *e.g.* during exercise, emotional stress, or hemorrhagic shock, whereas activation of the PSNS decreases it [97]. On the other hand, changes in SV are mainly induced by three factors [86]:

- a) *Preload*. In case of an increased venous return (venous flow returning to the heart), ventricular filling increases. The increase in volume leads to an increased tension in the cardiac muscle (by stretching the cardiac myocytes). The resulting increase in ejection force allows the heart to eject the additional volume, thereby increasing SV.
- b) *Afterload*. Afterload describes the load “seen” by the heart, against which it must eject blood. Afterload is closely related to R_t (or MAP). An increased afterload leads to a decreased SV.
- c) *Inotropy*. Cardiac inotropy (contractility) is controlled by the autonomic nervous system. The SNS increases cardiac inotropy, which allows the heart to eject more blood and increases SV. Conversely, the PSNS decreases SV via the opposite mechanism.

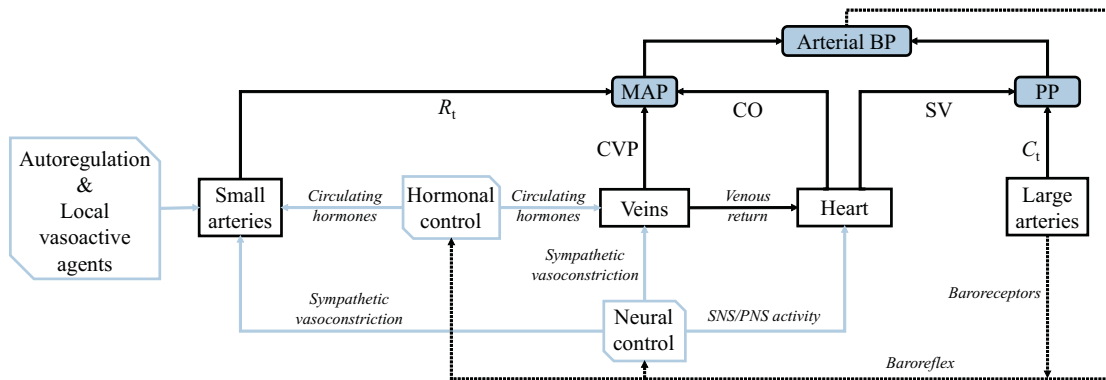


Figure 2.2 – Regulation of arterial BP in the systemic circulation. The figure is explained in detail in the text. For simplicity, R_t is entirely attributed to the small arteries in the figure, whereas C_t is entirely attributed to the large arteries. Also, the dependence of SV on ventricular *afterload*, which would take the form of a feedback arrow from R_t (or MAP) to “Heart”, is not depicted. BP: blood pressure; MAP: mean arterial pressure; PP: pulse pressure; CO: cardiac output; SV: stroke volume; CVP: central venous pressure; R_t : total vascular resistance; C_t : total vascular compliance; (P)SNS: (para)sympathetic nervous system.

The SNS is also involved – along with circulating vasoactive hormones such as adrenaline, angiotensin II and vasopressin – for the control of *vascular tone* (the tension exerted by the vascular smooth muscle) [97]. Vascular tone determines R_t and venous return, and thus its continuous adjustment plays an important role in the regulation of BP. Increasing vascular tone – and thus R_t – occurs through the *vasoconstriction* (narrowing) of blood vessels, mainly the small arteries (resistance vessels). Venous return is increased by peripheral venous vasoconstriction, which displaces the blood towards the central veins, thereby increasing CVP and SV. These neural and hormonal factors are *extrinsic* mechanisms in the control of vascular tone. Two *intrinsic* factors allow the local regulation of blood flow in the small arteries. The first one is autoregulation, a vascular myogenic response inducing a fast vasoconstriction in case of acute BP increase (see Figure 2.3). Autoregulation allows maintaining local flow and capillary pressure constant. Autoregulated vascular tone can further be controlled by a second intrinsic factor: local metabolic vasoactive agents produced within the vascular tissue allow autoregulated arteries to operate at a different level of flow [97].

The control of the neural and hormonal mechanisms that regulate BP is carried out by the so-called baroreflex (see dotted line in Figure 2.2), a rapid negative feedback mechanism operating within fractions of a second and maintaining BP at a nearly constant level. The baroreflex relies on so-called baroreceptors (stretch receptors sensitive to BP-induced distensions). The two main baroreceptors locations are found in the aortic arch and the carotid sinus.

2.3 Particularities of the pulmonary circulation

Some important differences exist between the systemic and pulmonary circulations. We have mentioned that PAP and pulmonary R_t are $\sim 1/7$ th of their systemic counterparts. We have also mentioned that pulmonary arterial compliance is distributed over the entire pulmonary arterial tree, as opposed to systemic arterial compliance which is mainly located in the aorta. Another important difference concerns the factors influencing R_t . Hereafter we will start by addressing this topic. We will then mention the various implications of a well-distributed pulmonary compliance.

2.3.1 Factors influencing pulmonary vascular resistance

With baroreceptors present in the pulmonary arteries, pulmonary R_t is controlled – in part – by neural and hormonal mechanisms similar to its systemic counterpart. However, R_t in the lungs is *not* affected by autoregulation or local vasoactive agents (left part of Figure 2.2). As a consequence, the pressure-flow relation is passive in the lungs: an increase in pressure leads to a quasi-proportional increase in flow, as detailed in Figure 2.3. Other factors, however, *do* affect pulmonary R_t , namely:

- a) *Lung volume*. R_t is known to be modulated by respiratory activity. The physiological aspects governing this phenomenon are explained in Figure 2.4.
- b) *Cardiac output*. An increased CO will distend the (highly compliant) pulmonary arteries and recruit previously closed/underperfused vessels, thus decreasing R_t (without significantly affecting the PAP) [46].
- c) *Gravity*. R_t is distributed unevenly when an upright position is adopted. Vessels at the apex (upper part) of the lungs (~ 16 cm above the heart) are barely perfused and collapse during diastole (low PAP, high R), whereas vessels at the bases of the lungs are hyperdistended and highly perfused (high PAP, low R) [97].
- d) *Hypoxia*. Hypoxic pulmonary vasoconstriction (HPV) is a mechanism that helps to maintain an efficient oxygenation of the blood. In case of hypoxia (lower oxygen supply), arteries leading to under-ventilated alveoli constrict in order to redirect the blood flow towards better-ventilated alveoli [97]. R_t increases as a result of this vasoconstriction.

2.3.2 Consequences of a well-distributed pulmonary vascular compliance

We have mentioned that ~ 80 % of vascular compliance is located in the aorta alone in the systemic circulation [149]. A remarkable characteristic of the pulmonary circulation is that only a small portion (15–20 %) of C_t is located in the major (main, left and right)

Chapter 2. Concepts on cardiovascular physiology

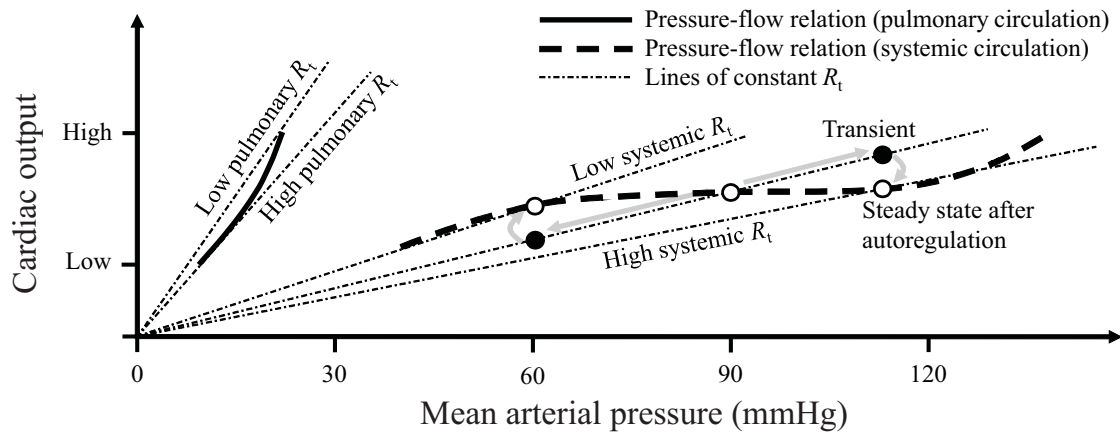


Figure 2.3 – Pressure-flow relationship in the systemic and pulmonary circulations (assuming zero venous pressure for simplicity). In the systemic circulation, a process known as autoregulation, illustrated here with gray arrows, allows maintaining local blood flow at a constant level through fast adaptation of the vascular tone in case of acute changes in BP. Autoregulation is absent of the pulmonary circulation, where the pressure-flow relationship is passive and almost linear. The curve steepens slightly with pressure due to flow-induced arterial distension (and related resistance decrease). Adapted from [97].

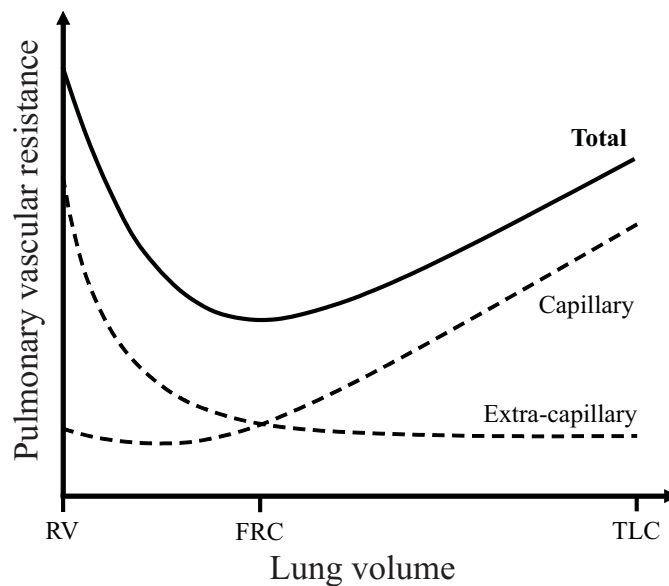


Figure 2.4 – Characteristic U-shaped relationship between pulmonary R_t and lung volume. At residual volume (RV), the increase in intrathoracic pressure compresses the arteries and veins (extra-capillary vessels), thereby increasing R_t . At total lung capacity (TLC), the increase in alveolar volume compresses the capillaries, thereby increasing R_t . The minimum of R_t is found at functional residual capacity (FRC), *i.e.* at end of passive expiration. Adapted from [46].

2.3. Particularities of the pulmonary circulation

pulmonary arteries. A considerable part ($\sim 50\%$) of pulmonary C_t is located in the arterioles [149]. Compliance and resistance are thus distributed in a similar fashion, and this anatomic distribution is unaltered in disease [164]. This special connection between R_t and C_t stands at the basis of several particular features of the pulmonary circulation:

- a) The so-called RC time τ_{RC} (the product of R_t and C_t) is constant in both health and disease [93, 94, 164]. In other words, an increase in arterial resistance is always accompanied by an inversely proportional decrease in arterial compliance, and vice versa, as illustrated in Figure 2.5. This means that the vessels responsible for resistance and compliance are the same in both health and disease [164]. This is not true for the systemic circulation, where τ_{RC} is highly variable due to the anatomic separation of C_t (central) and R_t (peripheral) [149, 164].
- b) The diastolic and systolic values of PAP are linearly related to the mean value of PAP (P_A) in both health and disease. In a retrospective study, Syeed *et al* [163] found the following relationships:

$$\text{Diastolic PAP} = 0.71 \cdot P_A - 0.66, \quad \text{Systolic PAP} = 1.50 \cdot P_A + 0.46.$$

The reason for this linearity is a consequence of τ_{RC} being constant. Indeed, combining (2.3) and (2.5) and neglecting venous pressure, we find that $P_A \approx \tau_{RC} \cdot \text{HR} \cdot \text{PP}$. With τ_{RC} constant and HR similar in health and disease, we find P_A to be proportional to PP [149]. As both quantities depend on the diastolic and systolic values of PAP, it can be derived that a linear relationship exists between these values and P_A [149]. This property does not hold true for the systemic circulation, where τ_{RC} is not constant.

- c) The ratio of right ventricular oscillatory power over total power is constant. The hydraulic power required by the heart for propelling blood to the arterial circulation consists in a mean power (the product of the mean pressure gradient and CO) and an oscillatory power, which can be considered as wasted power as it does not contribute to the transport of blood [149]. Because of the aforementioned linearity between diastolic and systolic PAP with P_A , the ratio of right ventricular oscillatory power over total power is constant in health and disease, and has found to be $\sim 23\%$ [150]. This contrasts with the systemic circulation, where the left ventricular ratio is $\sim 10\text{--}13\%$ in health and increases with BP [149].
- d) Finally, another consequence of a well-distributed pulmonary C_t is that arterial distensibility δ is uniform in the pulmonary circulation [90]. By definition, the distensibility of an arterial segment of volume V and compliance C is given by $\delta = C/V$, and is expressed in mmHg^{-1} [180]. (For instance, with a distensibility $\delta = 0.01 \text{ mmHg}^{-1}$, an increase in distending pressure of 15 mmHg will increase the volume of the artery by 15 %.) This property is unique to the pulmonary

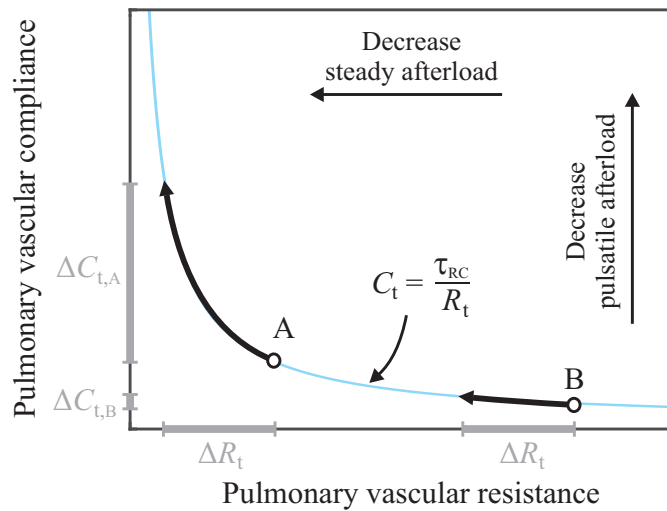


Figure 2.5 – Illustration of the consequence of a constant RC time τ_{RC} in the pulmonary circulation. Consider two patients (A and B) whose vascular resistance R_t is decreased through therapy by the same amount ΔR_t . Both will experience the same decrease in steady (resistive) afterload. However, only patient A will experience a significant decrease in pulsatile (capacitive) afterload. Adapted from [94].

circulation and has a remarkable consequence: the propagation velocity of the pressure waves in the arterial tree is uniform, as it directly depends on δ [180]. This will be further detailed in Section 2.5. Again, this property does not hold true for the systemic circulation, as systemic arteries become increasingly stiffer and muscular (*i.e.* δ decreases) as one moves away from the heart [121].

2.4 Cardiovascular pathologies

The present thesis tackles the subject of hemodynamic monitoring in general, but focuses in particular on two major hemodynamic parameters: cardiac output (CO) and pulmonary artery pressure (PAP). The purpose of this section is therefore to explain the clinical importance of CO and PAP, particularly in hemodynamically unstable patients, where both of these parameters are subjects to significant variations.

In Section 2.4.1, hemodynamic instability – and more specifically the underlying medical condition known as *circulatory shock* – is described in terms of its clinical and hemodynamic characteristics. Particular emphasis is put on the current clinical need for reliable non-invasive beat-to-beat CO monitoring solutions. Then, Section 2.4.2 introduces *pulmonary hypertension* (PH), its clinical subgroups and hemodynamic characteristics. Here, the emphasis will be put on the need for reliable non-invasive PAP monitoring solutions, both for events of acute PH that can arise in hemodynamically unstable patients and for

the monitoring of patients with chronic PH.

2.4.1 Circulatory shock

Clinical and hemodynamic characteristics

Circulatory shock (or simply shock) is a serious medical condition associated with high mortality rates and characterized by an inadequate oxygen delivery to body tissues (tissue hypoperfusion), usually resulting from inadequate CO [65]. Shock is common in critical care, and affects about one third of patients in intensive care units [169]. The clinical signs of shock are mainly cutaneous (*e.g.* mottled and clammy skin), renal (decreased urine output) and neurological (*e.g.* anxiety, confusion, disorientation). From a hemodynamic viewpoint, shock is characterized by a severely decreased BP (typically less than 70 mmHg in mean BP) and an increased heart rate (tachycardia). Depending on the type of shock (see below), CO can either be significantly decreased or increased. Finally, blood lactate levels are known to be abnormally high in shock, reflecting abnormal cellular function [169].

Diagnosis and clinical classification

The most common sign of shock is arterial hypotension, although a decreased BP is not sufficient to diagnose shock. Tachycardia, elevated blood lactate levels and the aforementioned clinical signs of tissue hypoperfusion are necessary to confirm the diagnosis [169]. Shock is clinically classified into four groups: distributive, hypovolemic, cardiogenic, and obstructive shock.

Distributive shock is characterized by a bacterial infection widely disseminated throughout the body, causing extensive damage and a marked vasodilation in the infected tissues [65]. As a result, CO is usually high in distributive shock (a unique feature for its diagnosis as CO typically decreases in all other types of shock). Echocardiographic signs in distributive shock are normal, *i.e.* normal cardiac chamber size and preserved contractility [169].

Hypovolemic shock, which occurs after a severe decrease in blood volume, is most often caused by hemorrhage [65]. Hypovolemic shock is characterized by a low CO (just as cardiogenic and obstructive shock) but a low central venous pressure (as opposed to cardiogenic and obstructive shock), as hypovolemia does not induce venous congestion. Echocardiographic signs usually shows small cardiac chambers, and normal or high contractility [169].

Cardiogenic shock can occur as a result of various cardiopathologies, *e.g.* acute myocardial infarction or advanced valvular diseases. It is characterized by a failure of the left

Chapter 2. Concepts on cardiovascular physiology

ventricle to pump blood efficiently, resulting in a low CO and progressively leading to venous congestion and an elevation in central venous pressure. Echocardiographic signs include enlarged ventricles and poor contractility [169].

Obstructive shock is characterized by an obstruction of blood flow in the large vessels or the heart itself, such as in case of pulmonary embolism (blockage of a pulmonary artery) or pericardial tamponade (accumulation of fluid in the pericardial cavity affecting heart function) [131, 169]. From a hemodynamic viewpoint, obstructive shock is somewhat similar to cardiogenic shock, *i.e.* decreased CO and elevated central venous pressure. Echocardiographic signs depend on the cause of the shock: enlarged right ventricle and small left ventricle in case of pulmonary embolism, and small ventricles in case of pericardial tamponade [169].

Therapy

In the event of shock, resuscitation should be started as soon as possible, even if the cause of the shock is still unknown [169]. The primary objective is to perform life-saving measures and to restore BP to an acceptable level. Oxygen should be administered immediately to improve oxygen delivery and prevent hypoxia-induced pulmonary hypertension. Once the underlying cause of the shock is identified, it must be corrected rapidly (*e.g.* control of bleeding in case of injury-induced hypovolemic shock). If the situation does not improve, an arterial catheter should be inserted for BP monitoring and blood sampling, and a central venous catheter for fluid resuscitation (replacement of lost bodily fluids) and injection of vasoactive agents. Fluid resuscitation mainly aims at improving CO and blood flow in the microvasculature through intravenous injections of fluids. A common difficulty in fluid resuscitation is the assessment of the patient's responsiveness to therapy. In mechanically-ventilated patients, signs of fluid responsiveness may be identified from beat-by-beat SV measurements. So-called fluid challenges are indicated to help assessing the patient's responsiveness, but must be rapidly stopped in absence of response to avoid fluid overload. The third component of resuscitation (along with oxygen administration and fluid therapy) is the intravenous injection of vasoactive agents. In particular, vasopressors (anti-hypotensive agents) such as norepinephrine are indicated to help increasing BP through vasoconstriction, while maintaining HR and CO. Conversely, inotropic agents such as dobutamine help increasing CO through increased myocardial contractility, with limited effects on BP.

The primary goal of resuscitation is to restore tissue perfusion by correcting arterial hypotension. Although a restored mean BP value of 65 to 70 mmHg is a good indicator, tissue perfusion should be assessed from the aforementioned signs of tissue hypoperfusion, namely skin appearance, urine output and mental state. CO is the main indicator for determining oxygen delivery, but no optimal CO value can be defined. In that sense, *trends* in CO rather than absolute values are of clinical importance to monitor the

patient's hemodynamic status, particularly during fluid challenges [169].

Prevalence

In a trial involving 1679 patients in intensive care units, septic shock (the most common form of distributive shock) was found in 62 % of cases. Non-septic distributive shock accounted for 4 % of all cases. Both hypovolemic and cardiogenic accounted for 16 % of all cases, and obstructive shock for 2 % [39, 169].

Current clinical need in terms of CO monitoring

There is a strong clinical need for practical, safe and continuous solutions for monitoring CO, in particular to assess reliable beat-to-beat trends in events of circulatory shock. However, as will be detailed in the next chapter, there is currently no safe, operator-independent and reliable way to monitor beat-to-beat CO values in hemodynamically unstable patients.

2.4.2 Pulmonary hypertension

Hypertension is a pathophysiological condition characterized by a persistent and abnormal elevation of BP. In the pulmonary circulation, *pulmonary hypertension* (PH) is formally defined as $P_A \geq 25$ mmHg at rest as assessed by right heart catheterization [56]. Untreated or inadequately treated PH is fatal as it increases the right cardiac afterload and thus ultimately leads to right heart failure (*cor pulmonale*) [97]. We have mentioned in the previous section the risk of acute PH in patients in circulatory shock in case of unmanaged hypoxia. This risk is even more increased in patients already suffering from chronic PH, which can arise from a wide variety of different pathophysiological causes. The exact prevalence of chronic PH remains unclear as the condition is considerably under-diagnosed due to the lack of specificity of the symptoms (*e.g.* shortness of breath, fatigue, weakness) [56]. Large discrepancies exist between prevalence estimates. In the UK, a prevalence of 10 cases/100,000 was reported; in contrast, a minimum indicative prevalence of 326 cases/100,000 was found in an Australian echocardiographic study [160].

Hemodynamic definitions

Multiple clinical conditions can lead to PH, left-sided heart diseases being the most common of them [56, 160]. In this situation, the failure of the left heart to pump blood leads to an elevation of left atrial pressure, which in turn causes an elevation of PAP upstream: therefore, PH is described as *post-capillary*. Conversely, most of the remaining forms of PH are induced by conditions or pathologies taking place before (*i.e.* upstream of) the

Chapter 2. Concepts on cardiovascular physiology

Table 2.1 – Hemodynamic definitions of pulmonary hypertension. PH: pulmonary hypertension; P_A : mean pulmonary artery pressure; P_W : (mean) pulmonary capillary wedge pressure. Adapted from [56].

Definition	Characteristics	Clinical groups
PH	$P_A \geq 25$ mmHg	All
Pre-capillary PH	$P_W \leq 15$ mmHg	1, 3, 4, 5
Post-capillary PH	$P_W > 15$ mmHg	2, 5

pulmonary capillary bed. In these situations, PH is described as *pre-capillary*. Clinically, pre- and post-capillary PH are distinguished from one another by measuring pulmonary capillary wedge pressure (P_W), an indirect estimate of left atrial pressure. P_W remains unaffected in pre-capillary PH and is markedly increased in post-capillary PH (central column of Table 2.1).

Clinical classification

Based on a consensus agreement of experts worldwide, PH is clinically classified into five groups, depending on clinical, pathological, hemodynamic and therapeutic considerations (Table 2.1): pulmonary arterial hypertension (Group 1), PH due to left heart disease (Group 2), PH due to lung diseases and/or hypoxia (Group 3), chronic thromboembolic PH and other pulmonary artery obstructions (Group 4), and PH with unclear and/or multifactorial mechanisms (Group 5) [56]. The diagnosis of PH and its classification into one of the five groups are carried out together. The diagnostic process starts with the suspicion of the presence of PH based on symptoms, signs or history [56]. An exam using transthoracic echocardiography is then performed in order to evaluate the likelihood of PH. In case of intermediate or high probability, further examinations are performed in order to confirm the diagnosis and assess the classification of PH. The following section presents each PH group in terms of its clinical and hemodynamic characteristics, diagnosis, therapy, and prevalence.

Group 1: Pulmonary arterial hypertension

Clinical and hemodynamic characteristics. Pulmonary arterial hypertension (PAH) is a form of pre-capillary PH that begins with *endothelial* dysfunction in the small pulmonary arteries. The endothelium (internal layer of blood vessels) regulates vascular tone and inhibits smooth muscle cell proliferation [92, 97]. Endothelial dysfunction thus leads to vasoconstriction and smooth muscle cell proliferation. A process known as vascular remodeling ensues, characterized by the muscularization, wall thickening and fibrosis of the small pulmonary arteries [92]. The later stages of PAH are characterized by the

appearance of local thrombi and so-called plexiform lesions, which further aggravate arterial occlusion [92].

Diagnosis. PAH is suspected when the main other forms of PH (Groups 2, 3, and 4) have been ruled out. The last group (Group 5) is associated with poorly understood mechanisms, as will be detailed later; its diagnosis is similar to that of Group 1 (PAH). The diagnosis of PAH or a rarer condition of Group 5 is confirmed by right heart catheterization if $P_A \geq 25$ mmHg and $P_W \leq 15$ mmHg (pre-capillary PH, see Table 2.1), and if $R_t > 0.18$ mmHg·s/mL [56]. Additional specific diagnostic tests (*e.g.* hematology, biochemistry, immunology) allows the final diagnosis to be refined (*e.g.* idiopathic PAH, heritable PAH, or a rarer condition of Group 5).

Therapy. The current treatment strategy for patients with PAH follows three main steps [56]: (1) general measures (*e.g.* encouraging patients to be active to improve cardiorespiratory function) and supportive therapy (*e.g.* anticoagulants or oxygen administration when appropriate); (2) specific drug therapy (vasodilator therapy with a treatment strategy depending on the patient's vasoreactivity and prognostic risk); (3) combination therapy (simultaneous use of two or more drugs) and consideration of lung transplantation in case of inadequate clinical response.

Prevalence. In Europe, PAH prevalence estimates stemming from epidemiological studies are in the range 15–60 cases per million population [56]. In an echocardiographic study, a prevalence of 15 cases/100,000 was reported [160].

Group 2: PH due to left heart disease

Clinical and hemodynamic characteristics. In Group 2, so-called PH due to left heart disease (PH-LHD) occurs as a secondary symptom to an underlying left heart condition (*e.g.* valvular diseases or advanced stages of heart failure). The failure of the left heart to pump blood efficiently leads to an elevation of left heart pressures. This pressure elevation is passively transmitted backwards and PAP increases in response, resulting in PH-LHD. In some cases, this passive elevation in PAP gives rise to vascular remodeling of the small pulmonary arteries, which further worsens the condition by increasing R_t .

Diagnosis. The diagnosis of PH-LHD is considered in a stepwise approach, by combining clinical presentation (*e.g.* symptoms of left heart failure, age, history), echocardiographic signs (*e.g.* structural left heart abnormality), and other modalities and imaging techniques [56]. The presence of post-capillary PH is formally confirmed by right heart catheterization with $P_A \geq 25$ mmHg and $P_W > 15$ mmHg (Table 2.1).

Therapy. As PH-LHD is secondary to an underlying condition, PH therapy in Group 2 focuses on managing said condition (*e.g.* repair of valvular heart disease when indicated). PAH therapy (vasodilator therapy) is not recommended as there is currently not enough

Chapter 2. Concepts on cardiovascular physiology

evidence demonstrating its benefits in the treatment of PH-LHD [56].

Prevalence. In an echocardiographic study, a prevalence of 250 cases/100,000 was reported, which makes of PH-LHD the most common form of PH (77 % of all cases) [160]. PH-LHD affects 60 % of patients with moderate or severe heart failure [58].

Group 3: PH due to lung diseases and/or hypoxia

Clinical and hemodynamic characteristics. As in Group 2, PH in Group 3 is secondary to an underlying condition, such as the very common chronic obstructive pulmonary disease. The mechanisms that lead to an abnormal and persistent elevation of PAP are specific to each condition. In chronic obstructive pulmonary disease for instance, the obstruction of small airways and the destruction of alveoli greatly decreases the diffusing capacity of the lungs (poor gaseous exchange), causing hypoxic pulmonary vasoconstriction [65]. As a result, a severe increase in R_t (and thus in PAP) occurs, as explained earlier (Section 2.3.1), progressively leading to PH.

Diagnosis. As for PH-LHD, the diagnosis of PH in Group 3 relies on a wide variety of modalities, such as chest radiography, pulmonary function tests and arterial blood gases. After confirmation of the diagnosis of a lung disease and when considered necessary (e.g. for surgical considerations), right heart catheterization is performed for the formal diagnosis of PH [56].

Therapy. As for PH-LHD, therapy in Group 3 focuses on managing the underlying condition, and not PH directly. Vasodilator therapy is thus not advised, all the more so as it may inhibit hypoxic pulmonary vasoconstriction and impair gaseous exchange. An example of therapy is the long-term administration of oxygen in case of COPD, which has shown to partially reduce PH [56].

Prevalence. In an echocardiographic study, a prevalence of 37 cases/100,000 (11 % of all cases) was reported, which makes of Group 3 the second most common form of PH after Group 2 [160].

Group 4: Chronic thromboembolic PH and other pulmonary artery obstructions

Clinical and hemodynamic characteristics. Chronic thromboembolic PH (CTEPH) is characterized by the partial or complete obliteration of one or several pulmonary arterial segments [128]. As a consequence, a part or the entirety of the flow is redirected towards the nonoccluded areas, thereby exposing them to higher wall shear stresses [72]. An arteriopathy similar to that encountered in PAH (vasoconstriction and vascular remodeling) progressively develops in these segments, while the arteries downstream of the occluded areas typically remain unaffected [72, 128].

Diagnosis. In the PH diagnostic process, CTEPH is considered after Group 2 and 3 have been ruled out. CTEPH is considered possible in case of perfusion defects in ventilation/perfusion scans, and confirmed by right heart catheterization and CT pulmonary angiography [56].

Therapy. Anticoagulation treatment is recommended in all patients with CTEPH. If the patient is found to be technically operable with an acceptable risk/benefit ratio, pulmonary thromboendarterectomy (surgical blood clot removal) is performed [56]. Otherwise, as an arteriopathy similar to that encountered in PAH develops in CTEPH, targeted vasodilator therapy is recommended [56, 72]. In case of severe and persistent PH, lung transplantation is considered [56].

Prevalence. CTEPH is notoriously under-diagnosed and its exact prevalence unclear [72]. An estimate of 3.2 cases per million population was reported in a PH Spanish registry [43]. A significantly larger prevalence of 9/100,000 was found in an Australian echocardiographic study [160].

Group 5: PH with unclear and/or multifactorial mechanisms

Clinical and hemodynamic characteristics. The exact mechanisms that lead to the development of PH are poorly understood in Group 5. PH is secondary to an underlying rare condition such as hematological, systemic or metabolic disorder [56].

Diagnosis. As detailed earlier for PAH, the diagnosis of PH in Group 5 is similar to that of Group 1, and thus not repeated here.

Therapy. As for the other types of PH secondary to an underlying condition, therapy in Group 5 focuses on managing the condition, and not PH directly. Vasodilator therapy is not advised in Group 5, due to the absence of randomized control trials demonstrating its benefits. It may even be harmful in case of disorders affecting the venous tree, such as the pulmonary veno-occlusive disease [56].

Prevalence. In an echocardiographic study, a prevalence of 15 cases/100,000 (4.6 % of all cases) was reported, which is similar to that of PAH [160].

Current clinical need in terms of PAP monitoring

There is a strong clinical need for risk-free and continuous solutions for monitoring the PAP, particularly in hemodynamically unstable patients. Similarly, the follow-up of patients with chronic PH currently lacks a proper monitoring tool to assess the patient's health status on a regular basis. Indeed, the follow-up of PH patients is often limited to clinic visits at intervals of several months. The risk (in case of right heart catheterization) and cost associated with more frequent measurements (*e.g.* weekly measurements) of

the patient's PAP strongly hinders the identification of short-term trends in pulmonary hemodynamics, and therefore the anticipation of worsening conditions or treatment inefficiency [111]. Increases in PAP have been shown to occur days to weeks before the onset of worsening signs and symptoms [1]. The benefits of frequent PAP measurements over intermittent clinic visits have been demonstrated in several previous studies, notably in terms of prediction of therapy outcomes [48], anticipation of worsening heart failure [3], feedback rapidity during vasodilator therapy [53], or decline in hospitalization rates [15]. Here again, a simple non-invasive means of monitoring the PAP in patients with chronic PH is currently lacking.

2.5 Pulse wave velocity

In this thesis, a novel method for measuring changes in PAP will be proposed and evaluated. We introduce hereafter the physiological principle on which this method is based.

At each heartbeat, pressure waves are produced by the heart at the aortic and pulmonary valves, and propagate along the wall of the arteries towards the periphery. The so-called pulse wave velocity (PWV) is the velocity at which these BP waves travel along the arterial wall. This velocity is higher in stiffer arteries. Thus, as stiffer arteries require a higher pulse pressure to expand, it follows that BP and PWV are intrinsically linked. In other words, arterial stiffness induces rises in both BP and PWV [180]:

$$\text{Arterial Stiffness} \nearrow \Rightarrow \begin{array}{l} \text{Blood Pressure} \nearrow \\ \text{Pulse Wave Velocity} \nearrow \end{array}$$

2.5.1 Relation to arterial stiffness and compliance

The relations linking arterial stiffness, compliance and the PWV are described via two equations. The first one is known as the Moens-Korteweg equation:

$$\text{PWV} = \sqrt{\frac{hE_{\text{inc}}}{\rho d}}, \quad (2.6)$$

where arterial stiffness is embodied by the incremental Young's modulus E_{inc} [180] and where h/d is the wall thickness to diameter ratio of the arteries, a quantity that remains almost invariable in elastic arteries [158]. Therefore, with ρ (density of blood) constant, the Moens-Korteweg equation directly links PWV to arterial stiffness in elastic arteries. The relation of PWV with compliance (C) and distensibility (δ) is described by

the Bramwell-Hill equation [180]:

$$\begin{aligned} \text{PWV} &= \sqrt{\frac{V}{\rho C}} \\ &= \sqrt{\frac{1}{\rho \delta}} \end{aligned} \tag{2.7}$$

where V is the arterial blood volume. It stems from (2.7) that the PWV depends directly on δ alone. As mentioned earlier in Section 2.3.2, a remarkable property of the pulmonary circulation is the uniformity of δ in the entire arterial tree, irrespective of vessel size. Therefore, via (2.7), PWV is also found to be uniform in the pulmonary arterial tree. This strongly contrasts with the systemic circulation, where the PWV increases in the periphery due to the smaller distensibility of resistance vessels [121].

2.5.2 Clinical significance

Before being a correlate of BP, PWV is a clinical surrogate of arterial stiffness, the best independent predictor of cardiovascular and all-cause mortality [158]. In the pulmonary circulation in particular, arterial compliance (which is inversely related to arterial stiffness and PWV, as seen hereabove) has shown to be a stronger predictor of outcome than vascular resistance or PAP itself in patients with PH [94, 102]. This aspect can easily be understood via Figure 2.5. A patient who is developing PH starts on the left-most part of the curve and progressively moves from left to right as the disease worsens. Therefore, in the early stages of PH, a large loss of compliance can occur before any noticeable increase in resistance or pressure takes place, making of pulmonary arterial compliance (or stiffness, or PWV) a strong predictor of survival [94, 95].

2.5.3 Typical values

In the aorta, PWV values typically range from 4 m/s in normotension, to 15 m/s in hypertension [121]. These values are noticeably lower in the pulmonary arteries, ranging from 2 m/s in normotension to 7 m/s in hypertension [96, 148]. Using (2.7), this translates to pulmonary distensibility values larger by a 4-fold factor than their systemic counterparts, as expected from the highly-compliant nature of the pulmonary arteries. Figure 2.6 illustrates the relationship between mean PAP and pulmonary PWV.

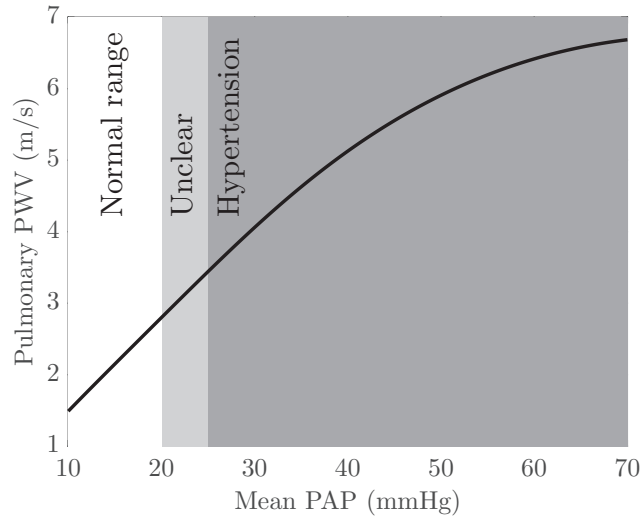


Figure 2.6 – Relationship between mean pulmonary artery pressure and pulmonary pulse wave velocity (PWV). From ~ 40 mmHg and above, the curve starts reaching a plateau level, as the arteries are approaching their elastic limit [96]. In other words, as pressure keeps increasing, the arterial wall cannot distend to the same extent: δ is approaching its lower limit, which translates to a higher limit in PWV via (2.7). Curve compiled with data from [96] and [148].

2.5.4 Measurement principle

The PWV in an arterial pathway going from a proximal point a to a distal point b can be calculated as:

$$PWV = D/PTT, \quad (2.8)$$

where D is the distance between a and b , and PTT is the so-called *pulse transit time*, *i.e.* the time required for a pressure wave traveling along the arterial wall to go from a to b . Depending on the arterial pathway considered, D can usually only be roughly estimated from surface measurements and anthropometric data. However, for blood pressure-related applications, estimating D is unnecessary as a calibration function $f(\cdot)$ is eventually required for converting the estimated PWV values to pressure units. Therefore, monitoring changes in BP via the PWV principle directly relies on monitoring changes in PTT and considering D to be constant:

$$BP = f(1/PTT). \quad (2.9)$$

Estimating the PTT requires choosing two distinct (and distant) arterial sites a and b , and detecting the time of arrival of the pressure wave – the so-called pulse arrival time

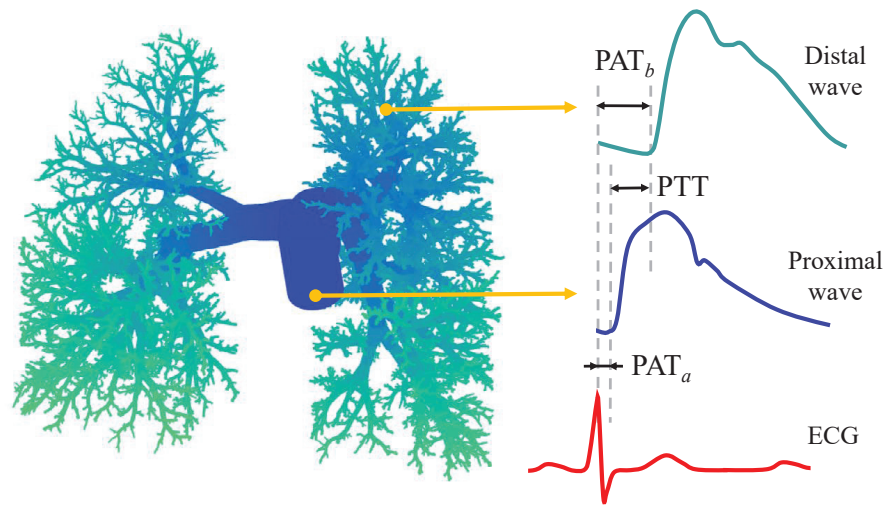


Figure 2.7 – Measurement of the pulmonary pulse transit time (PTT) as the difference between the pulse arrival times (PAT) at location a and b in the arterial tree.

(PAT) – at both locations. PTT is then simply obtained as the difference between both times:

$$\text{PTT} = \text{PAT}_b - \text{PAT}_a. \quad (2.10)$$

Both PAT values are usually computed relative to a given timing reference $t_0 = 0$. A typical choice for t_0 is the timing of the R-wave peak of the electrocardiogram (ECG), as the feature is robustly identifiable. Figure 2.7 illustrates a measurement of the PTT in the pulmonary arterial tree (provided one has access to the pressure waveforms in both locations depicted).

3 State of the art in cardiovascular monitoring techniques

In the previous chapter, we have emphasized the current clinical need for safe and continuous solutions for monitoring the cardiac output (CO) and the pulmonary artery pressure (PAP). The purpose of the present chapter is to provide an overview of the existing modalities and techniques for CO (Section 3.1) and PAP (Section 3.2) monitoring, and to highlight their strengths and limitations.

3.1 Cardiac output

3.1.1 Gold standards

The gold standard CO measurement method uses the Fick principle, which computes CO as the rate of oxygen consumption divided by the difference between arterial and venous oxygen concentrations [97]. However, its clinical applicability remains limited, as this method is time-consuming – with a time resolution of 5 to 10 minutes [97] – and only valid in a steady hemodynamic and respiratory state [121].

In clinical settings, the gold standard CO monitoring technique uses the pulmonary artery catheter (PAC) thermodilution method: a known mass of cold saline is injected into the right heart, and CO is computed from the area under the temperature curve measured at a point downstream [97]. PAC thermodilution offers a better time resolution (~ 30 s) than the Fick principle, but requires averaging 4 to 5 measurements for comparable accuracy [80].

3.1.2 Partial rebreathing methods

Partial rebreathing methods, as implemented in the NICO system (Respironics, Murrysville, USA), are derived from the Fick principle and use carbon dioxide as indicator instead of oxygen [79]. An extension loop is added to the circuit of a ventilator and al-

lows estimating the venous carbon dioxide content [54]. The system is thus non-invasive but restricted to intubated and ventilated patients [36].

Clinical studies evaluating its accuracy have reported good *trending ability* (high correlation coefficients) but significant bias in several patient populations. The approach remains untested in hemodynamically unstable patients [54].

3.1.3 Pulse contour methods

Pulse contour methods are a family of CO estimation methods based on the morphological analysis of arterial pressure waveforms [131]. As the relation between pressure and flow is not constant, pulse contour methods require periodic recalibration maneuvers, more frequently in case of varying CO [54, 131]. They rely on the joint estimation of stroke volume (SV) and heart rate to estimate CO, as CO is the product of both parameters.

The PiCCO system (Pulsion Medical Systems, Feldkirchen, Germany) measures the pressure waveform in a large (*e.g.* femoral or axillary) artery and uses transpulmonary thermodilution for calibration [131]. The working principle of transpulmonary thermodilution is similar to that of PAC thermodilution, but uses a central venous line for injection and the temperature curve is measured at the arterial catheter. Beat-to-beat SV estimation is obtained by computing the area under the curve of the flow waveform estimated from the pressure waveform via a so-called *Windkessel* model (later described in Section A.2) [36].

The LiDCO system (LiDCO Ltd, Cambridge, UK) is slightly less invasive as it relies on peripheral venous and arterial lines. Calibration is performed via lithium dilution, with the advantage of a high signal-to-noise ratio (SNR) as lithium is naturally absent in blood [54]. However, frequent recalibration maneuvers are limited in presence of muscle relaxation drugs [131]. For beat-to-beat SV estimation, the LiDCO system does not use a pulse contour method *per se*, as it relies on a power analysis of the pressure waveform and not on its morphology [131].

The FloTrac system (Edwards Lifesciences, Irvine, USA) measures the pressure waveform in the femoral or radial artery. As opposed to the PiCCO and LiDCO systems, FloTrac uses a self-calibration procedure. Beat-to-beat SV estimation is obtained from the pulse pressure (PP) as $SV = \chi \cdot PP$. PP is estimated as the standard deviation of the pressure waveform, while the χ factor is automatically re-estimated every minute using waveform morphological features and anthropometric data of the patient. Although appealing, this calibration maneuver is of limited accuracy [161].

Non-invasive systems such as the Nexfin system (BMEYE, Amsterdam, The Netherlands) measure the pressure waveform at the digital artery via the volume-clamp

method [36, 131]. The peripheral waveform is transformed into a central waveform using a generalized transfer function [180] and a Windkessel model is used to estimate a central flow waveform, and thus estimate SV [131]. The Windkessel parameters are obtained from empirical relationships with pressure derived from population averages [131].

The reliability of pulse contour systems in anesthesia and intensive care units is questioned because of their inability in tracking changes in peripheral resistance [36]. Invasive recalibration maneuvers are necessary whenever changes in vascular tone and/or CO may have occurred [14, 131].

3.1.4 Ultrasound methods

Ultrasound methods are based on the measurement of the mean blood velocity across the aorta via the Doppler ultrasound technique. The area under the velocity-time curve provides the so-called stroke distance, or velocity time integral (VTI) [97]. SV is obtained by multiplying the VTI with the cross-sectional area of the aorta.

The USCOM system (USCOM Ltd, Sydney, Australia) uses transthoracic Doppler ultrasound: the VTI is obtained non-invasively by directing the Doppler probe at the ascending aorta. The CardioQ-ODM system (Deltex Medical, Chichester, UK) uses transesophageal Doppler ultrasound: the VTI is obtained by inserting the probe through the patient's esophagus and directing it at the descending thoracic aorta [97, 106]. The transesophageal approach is invasive and thus limited to anaesthetized patients [36], but benefits from two main advantages over its transthoracic counterpart: it is more conducive to continuous monitoring [106], and has a better signal-to-noise ratio due to the proximity of the probe with the source of the signal [131]. However, both approaches depend strongly on the operator [36] and are very sensitive to probe positioning [106]. In both systems, the area of the aorta is estimated from the patient's anthropometric data [36]. Alternatively, the area can be assessed by measuring the diameter of the aorta using echocardiography, either non-invasively (transthoracic) or invasively (transesophageal) [106].

Another non-invasive ultrasound-based approach consists in estimating the end-diastolic and end-systolic volumes of the ventricles from echocardiograms of the ventricles using an assumed chamber geometry [97]. SV is obtained as the difference between both volumes. Alternatively, cardiac magnetic resonance imaging (MRI) scans can be used instead [166].

3.1.5 Impedance-based methods

Impedance cardiography (ICG) systems, such as the BioZ system (Cardiodynamics, San Diego, USA), measure thoracic electrical bioimpedance through electrodes located at

specific locations at the neck and the abdomen [54]. In this configuration, the injected electrical currents are assumed to pass mostly through the aorta, and therefore the pulsatile (cardiogenic) component of the measured impedance signal is assumed to be representative of aortic blood volume [36]. Its first time derivative – the so-called ICG signal – is thus expected to be representative of aortic flow. Therefore the peak amplitude of the ICG signal is expected to be linked to SV. The method has not gained widespread acceptance in clinical practice because of its contested accuracy and the lack of understanding of the phenomena being measured [71, 106, 177].

Another impedance-based approach has been proposed more recently and is implemented in the NICOM system (Cheetah Medical, Inc., Newton Center, USA). The method is known as bioimpedance and makes use of the phase shift of the thoracic bioimpedance signal [106]. Using the phase shift induced by aortic pulsatility (instead of its modulus as in ICG) is thought to reduce the influence of factors affecting the ICG signal, such as lung water; however, as for ICG, there is a lack of understanding of what the bioimpedance signal actually measures [36]. Its first time derivative is used to estimate cardiac parameters in a similar fashion to ICG. The performance of the bioimpedance approach for beat-to-beat SV estimation remains unclear [36], with poor accuracy reported in critically ill patients [44, 91].

3.1.6 Limitations of current CO monitoring techniques

In their review, Shephard *et al* [153] described the eight ideal characteristics for CO monitoring techniques: accuracy, reproducibility, fast response time, operator independency, ease of use, absence of morbidity, measurement continuousness, and cost effectiveness. To this day, no existing CO monitoring technique has been able to meet all of these requirements [131]. In particular, beat-to-beat and continuous monitoring techniques, which are of paramount importance for patients in circulatory shock, suffer from poor trending ability in case of hemodynamic instability.

3.2 Pulmonary artery pressure

3.2.1 Gold standard

The gold standard PAP measurement technique is the invasive PAC. An accurate measurement of the PAP implies some technical requirements to be followed with caution. In particular, verifying the dynamic response of the PAC is necessary due to the risk of under- or overdamped pressure waveforms [57]. Moreover, the system must be properly leveled and re-zeroed after each change in position. For every 1 cm shift above right atrial level (atmospheric pressure), 0.74 mmHg of hydrostatic pressure is subtracted from the pressure measured [89, 110].

3.2.2 Implantable hemodynamic monitors

Wireless implantable hemodynamic monitors (pressure sensors implanted in the pulmonary arteries) such as the CardioMEMS HF System (CardioMEMS Inc., Atlanta, USA) have been recently introduced for the management of heart failure patients [1]. They are able to provide beat-to-beat PAP readings with good accuracy [2].

3.2.3 Ultrasound methods

The main ultrasound-based method for PAP estimation is based on the Doppler measurement of the peak velocity v_{\max} of the tricuspid regurgitation (TR) jet, *i.e.* the velocity of the small blood backflow pushed from the right ventricle back through the tricuspid valve into the right atrium during ventricular ejection. Trivial or mild TR occurs in 50–80 % of normal subjects [16, 37, 40, 112]. Its prevalence (70–80 %) and severity is higher in cardiac patients [37, 40]. As right ventricular pressure and PAP are virtually equal during systole, systolic PAP (SPAP) can be estimated using the so-called modified Bernoulli equation [37]:

$$\text{SPAP} = 4v_{\max}^2 + \text{RAP}, \quad (3.1)$$

where RAP is right atrial pressure. When estimated non-invasively, RAP can only be obtained in a semi-quantitative manner from the change in diameter of the inferior vena cava assessed by echocardiography [56]. Alternatively, RAP can also be assumed to be constant, for instance 10 mmHg [112]. The latter option has the advantage of simplicity and provides comparable results [30, 37]. Comparison of TR-derived SPAP estimates with PAC-derived measurements show good agreement [10, 37, 108]. However, in the individual patient, the measurement of v_{\max} can be inaccurate, depending on the strength of the TR signal [56].

TR velocity is currently considered the main echocardiographic variable for estimating the likelihood of PH in symptomatic patients [56]. Other echocardiographic variables such as the time to peak right ventricular outflow (acceleration time) are known to correlate with the PAP [30]; their use in conjunction with v_{\max} for assessing the probability of PH is recommended [56].

Other ultrasound-based approaches have been proposed for measuring PAP-related variables. In [96], intravascular ultrasounds were used for the real-time imaging of the proximal pulmonary artery for estimating pulmonary arterial distensibility and compliance, both of which show an inverse exponential relation with the PAP. Similar findings were obtained non-invasively using MRI [148].

3.2.4 Phonocardiography-based methods

Various approaches based on the spectral analysis of the second heart sound have been proposed to estimate the PAP [31, 156, 184]. Xu *et al* [184] estimated the PAP indirectly using as feature the time interval between the aortic and pulmonary components of the second heart sound. There is however no direct physiological link between the PAP and this feature. Besides, the feature can be affected by diseases such as systemic arterial hypertension, or aortic/pulmonary valve stenosis. The trending ability of the proposed approach in the individual patient was not reported by the authors. Smith *et al* [156] used a larger feature space ($N = 10$). Large inter- and intra-dataset variances were obtained in the selection of the optimal feature subset, depending on the algorithm or selection method used. Their PAP estimation approach was even more indirect given the larger number of features used and the lack of direct physiological link between any of them and the PAP. The trending ability of the proposed approach in the individual patient was not reported neither.

3.2.5 Limitations of current PAP monitoring techniques

An optimal PAP monitoring modality should be non-invasive (free of any risks or complications associated with cardiac catheterization) and unsupervised (able to operate continuously without supervision of a medical doctor). Besides, it should be able to monitor short-term trends (trending ability), *e.g.* with a time resolution of 30 seconds or less. While the gold standard PAC and implantable monitors lack the first requirement, ultrasound-based methods lack the two last ones. Phonocardiography-based approaches have the advantage of complying with the two first requirements. However, their trending ability remains to be tested. Furthermore, their limited physiological basis, their invalidity under certain pathophysiological conditions, and the sensitivity of the measurement to background noise [184] strongly hinders their applicability for routine PAP monitoring in a clinical context.

4 Concepts on electrical impedance tomography

Electrical impedance tomography (EIT) is a non-invasive, non-ionizing and low-cost functional imaging technique allowing real-time visualization of impedance changes within the thorax. First tested for medical applications in 1978 [70] and originally introduced as applied potential tomography [11], EIT has been a growing center of attention since the mid-90s in fields such as thoracic imaging of lung and cardiac function, as well as brain and gastrointestinal tract imaging [6, 73]. The present thesis focuses on the use of EIT for thoracic imaging.

4.1 Thoracic imaging by EIT

4.1.1 Working principle

A typical EIT monitoring system consists in a belt of electrodes placed in a ring around a given medium of interest. Small electrical currents are injected into the medium and the resulting voltages are measured on its surface. A reconstruction algorithm then estimates, from these surface measurements, the most likely distribution of internal impedance changes. The result is a 2D tomographic image depicting the internal distribution of impedance change in the medium, and is commonly referred to as EIT frame, or simply EIT image. The technology is characterized by a low spatial resolution, but its strength resides in its high time resolution. Frame rates up to 50 images per second are common.

In thoracic imaging by EIT, the medium of interest is the thoracic cavity. The belt of electrodes is placed around the chest and images of the intra-thoracic distribution of bioimpedance changes are reconstructed.

4.1.2 Factors affecting thoracic bioimpedance

In thoracic EIT, most systems measure local *changes* in bioimpedance (with respect to a given reference spatial distribution)¹. In the thorax, changes in the internal distribution of bioimpedance are mainly induced by *respiratory* and *cardiovascular* activity. Figure 4.1a shows an example of an EIT image measured at the heart level in a healthy 28-year-old male subject during normal breathing, illustrating the effects of respiratory activity on the EIT signal. The measurements were obtained with a Goe MF II device (CareFusion, Höchberg, Germany) and the images reconstructed with the GREIT algorithm [5]. The effects induced by cardiovascular activity are hardly visible in that image as their amplitude is typically 10 times smaller than their respiratory counterparts. Figure 4.1b shows an EIT image measured in the same conditions but during breath-hold, illustrating the effects of cardiovascular activity on the EIT signal.

4.1.3 Separation of the respiratory- and cardiovascular-related components

Estimating parameters related to cardiovascular activity with EIT – one of the aims of the present thesis – requires the EIT signal to show minimal influence from breathing-related conductivity changes. Various methods have been proposed in the literature to isolate the cardiovascular component. Although not appropriate for continuous monitoring in contexts such as intensive care units, acquiring the EIT data during breath-hold remains the simplest and most effective approach [49]. Separation methods exploiting principal component analysis have been proposed [41, 130]. More commonly used, frequency filtering techniques (*e.g.* high-pass filtering) are a simple and effective alternative for strongly reducing the influence of the respiratory component. Another well-known approach is ECG-gated ensemble averaging, which consists in exploiting the physiological synchrony of cardiovascular-related EIT signals with the ECG signal. This method provides a more selective filtering than a simple high-pass filter by acting as a comb filter with increasingly wider lobes at higher cardiac harmonics [139]. The process can be performed in post-processing or in real-time by using the ECG signal as trigger during the data acquisition process.

4.2 EIT for bedside monitoring of the cardiorespiratory system

4.2.1 Current situation and challenges

The aforementioned qualities of EIT, in particular its non-invasiveness and its ability to provide continuous measurements, make of this technology an ideal candidate for

¹We explain later the rationale for reconstructing distributions of intra-thoracic impedance *changes* instead of absolute impedance values. Moreover, as impedance is mainly resistive at EIT frequencies [47, 73], EIT images are often depicted as distributions of *conductivity* changes (the inverse of resistance). We use this convention in the present thesis.

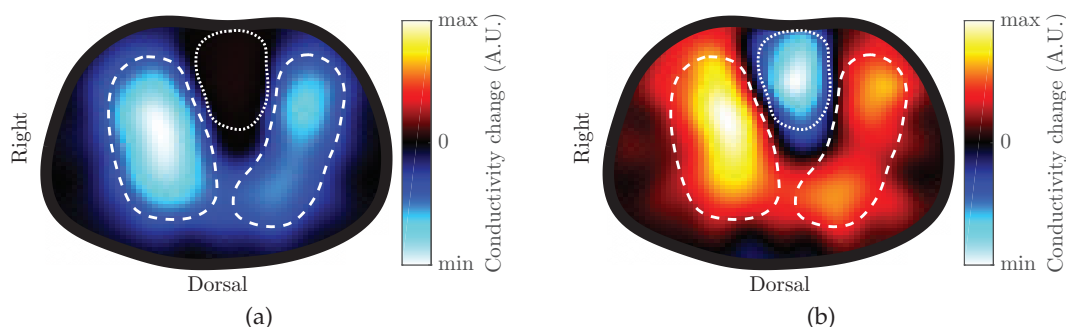


Figure 4.1 – Internal distribution of conductivity *changes* measured by EIT in a healthy subject: (a) at end inspiration with respect to end expiration, and (b) during breath-hold at end systole with respect to end diastole. Color scales are *not* the same between both images, as cardiovascular-related changes are of much smaller amplitude. Warm colors depict conductivity increases; cool colors depict conductivity decreases. The dashed lines highlight the pulmonary regions of interest; the dotted line highlights the cardiac region of interest. In (a), the conductivity decreases in the lung regions at inspiration due to the inflow of air, which deforms the cells of the alveolar walls and changes their dielectric properties [122]. In (b), the ejection of highly conductive blood from the ventricles to the lungs induces a decrease in conductivity in the heart region and an increase in the lungs.

patient monitoring at the bedside (*e.g.* in intensive care units), as illustrated in Figure 4.2. However, before EIT can make its way into routine clinical practice, several challenges, in particular a proper definition of standardized EIT protocols, findings, interpretations and diagnostic tools, need to be overcome [52].

4.2.2 Clinical outlook

At the current state of research, the most promising field of application of EIT is thought to be the monitoring and optimization of ventilation [6] as significant advances have been achieved in terms of EIT-based assessment of end-expiratory lung volume and ventilation distributions over the last decades [51]. Besides, cardiovascular applications have received increasing attention as well. In particular, the clinical potential of EIT has been investigated for the estimation of hemodynamic parameters such as cardiac output [129, 174], aortic blood pressure [157], pulmonary perfusion [21, 49, 120] or stroke volume variations [104].

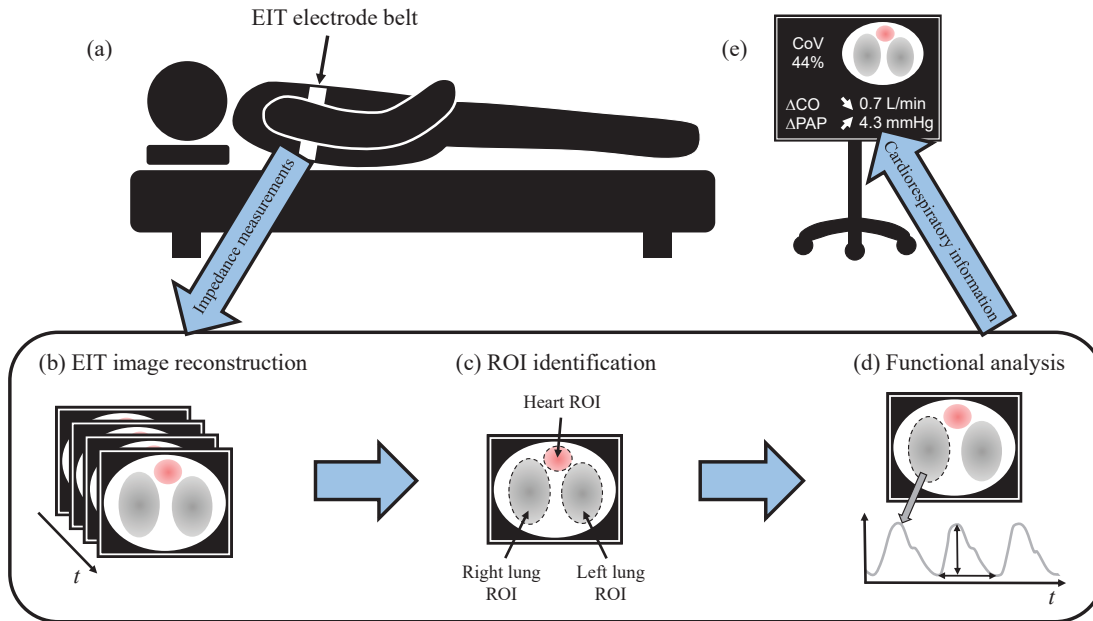


Figure 4.2 – Concept of bedside EIT monitoring. (a) A belt of equidistantly spaced electrodes is attached around the patient’s chest. (b) Impedance measurements are performed and supplied to an image reconstruction algorithm, resulting in sequence of EIT images. (c) Regions of interest (ROI) characteristic of particular organs or anatomical structures are identified and (d) ROI-wise or pixel-wise functional analysis of the impedance signals is performed. (e) The estimated cardiorespiratory parameters resulting from the analysis are provided to the clinician.

4.3 Technical aspects of EIT

4.3.1 Measurement of bioimpedance

Formally, bioimpedance is a measure of the opposition presented by biological tissue to an electrical current when a voltage is applied. Electrical currents flow through a biological tissue via the movement of ions among its cells [47]. The path taken by the current will depend on its frequency. Low-frequency currents will hardly penetrate the cells, as their membranes are mostly capacitive [13]. The currents thus primarily travel through the viscous extra-cellular fluid, which behaves as a resistor. At higher frequencies however, the currents will be able to charge the cell membranes and flow through them and the intra-cellular fluid [47]. This aspect is illustrated in Figure 4.3. A cell suspended in extra-cellular fluid can be modeled as a capacitor C in series with a resistor R_1 , both of which are in parallel with another resistor R_2 [13]. More generally, the entire human body can be electrically modeled as a combination of capacitive and resistive elements, with reasonable accuracy for low-voltage levels [47].

Considering the abovementioned aspects, the choice of frequency of the injected currents

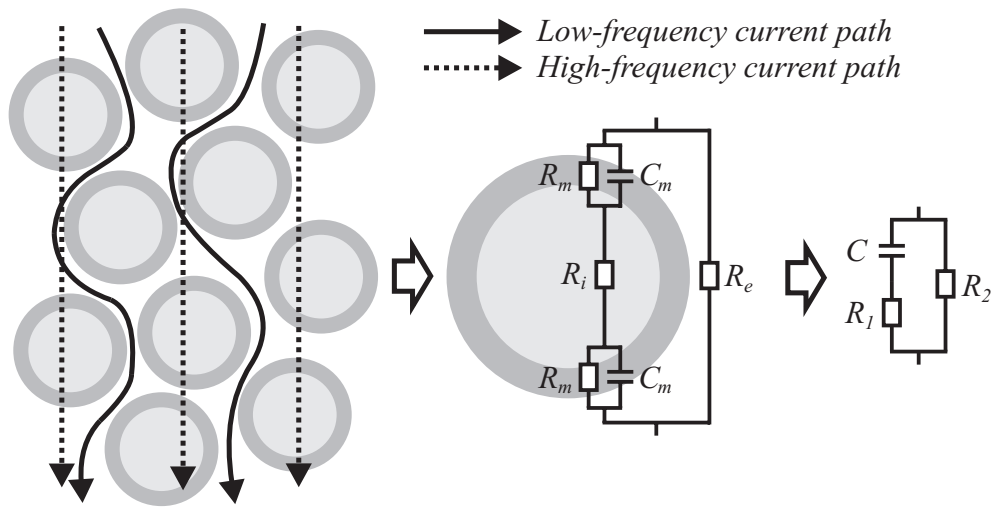


Figure 4.3 – Path of electrical currents through a suspension of cells. Low-frequency currents can hardly penetrate the cells due to the dominantly capacitive behavior of their membrane. High-frequency currents are able to pass through the membrane and the intra-cellular space. C_m : membrane capacitor; R_m : membrane resistor; R_i : intra-cellular fluid resistor; R_e : extra-cellular fluid resistor; C , R_1 , R_2 : capacitor and resistors of the equivalent circuit. Adapted from [13].

in EIT is a matter of compromise. The skin-electrode impedance is large at lower frequencies (up to $1\text{ M}\Omega$ at 1 Hz and $100\text{ k}\Omega$ at 100 Hz), but drops as frequency increases (down to $220\ \Omega$ at 100 kHz and $120\ \Omega$ at 1 MHz) [144]. Large skin-electrode impedances induce a substantial voltage drop on the injecting electrodes, and impedance imbalance on the measuring electrodes, thus degrading the common-mode rejection of instrumentation amplifiers [73]. This aspect favors higher frequencies. Furthermore, maximal allowed RMS amplitude of so-called *patient leakage currents* are very restricted at lower frequencies (0.1 mA at 100 Hz according to the current international electrical safety standards IEC 60601-1:2005) [77], which limits the signal-to-noise ratio. Beyond 1 kHz , the risk decreases rapidly and current amplitude can be increased, up to 10 mA at 100 kHz [77]. This aspect also favors higher frequencies. However, as frequency increases, the influence of capacitive effects (parasitic capacitances) increases, thereby limiting the possible frequency range [73]. Taking all these elements into consideration, a frequency of 100 kHz can thus be considered typical for EIT and – more generally – bioimpedance measurements, with most studies operating in the range $10\text{ kHz} - 1\text{ MHz}$ [47]. The choice of the amplitude of the injected currents is then dictated by safety considerations in function of the chosen frequency and the limitations of the device used.

4.3.2 Stimulation and measurement patterns

An EIT system typically consists of a belt of n_S electrodes equidistantly spaced on the periphery of the thorax. Small electrical currents are injected on pairs of electrodes and

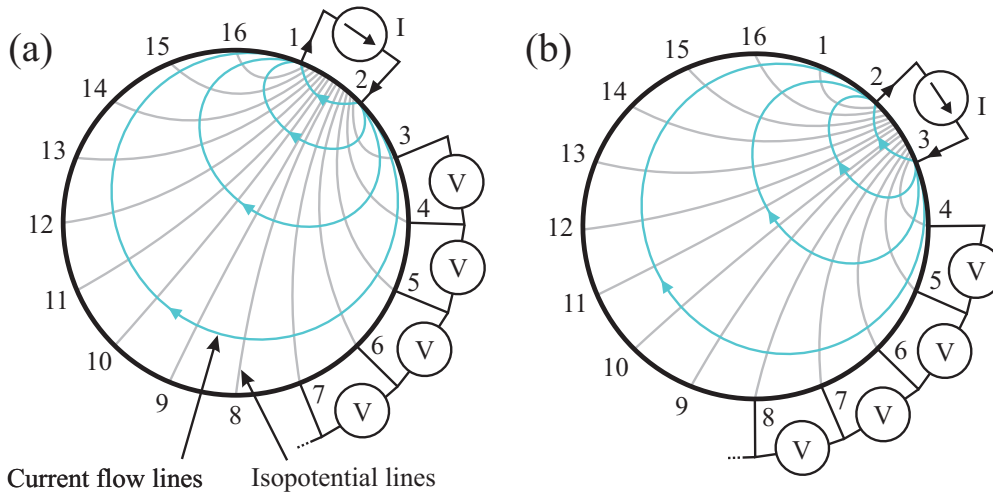


Figure 4.4 – Adjacent stimulation and measurement pattern: example for a 16-electrode configuration. (a) The current is injected on the first pair of adjacent electrodes ($\{1,2\}$) and the resulting voltages are measured on the remaining pairs ($\{3,4\}, \{4,5\}, \dots, \{15,16\}$). (b) The same process is repeated until each adjacent pair has been used as injecting pair once. Adapted from [105].

the resulting voltages are measured on the remaining pairs according to a so-called *stimulation and measurement pattern*. For instance, in the widely-used *adjacent* pattern illustrated in Figure 4.4, the current is first injected through the pair of electrodes $\{1,2\}$, while the resulting voltages are measured on the $(n_S - 3)$ remaining adjacent pairs (Figure 4.4a). The current is then injected on the next pair of adjacent electrodes, namely $\{2,3\}$, and the resulting voltages are measured on the remaining pairs again (Figure 4.4b). Once each pair of adjacent electrodes has served for current injection, a total of $n_M = n_S(n_S - 3)$ voltage measurements have been performed. However, because of reciprocity, only $n_M/2$ of these voltage measurements are independent [105]. The choice of stimulation and measurement pattern depends on the system and the application. With the adjacent pattern, current density is larger near the injecting electrodes and decreases rapidly as a function of distance [105]. Sensitivity is thus larger near the boundaries, but weak near the center of the thorax, where most cardiorespiratory phenomena of interest occur. Other patterns, where the pairs of injecting/measuring electrodes are separated by one or more electrodes, allow a more uniform current density and a better sensitivity in the central regions, at the cost of a decreased sensitivity near the boundaries [81].

4.3.3 Image reconstruction

The generation of an EIT frame begins with the acquisition of n_M voltages $\mathbf{v}_m \in \mathbb{R}^{n_M}$ using a given stimulation and measurement pattern. The voltages are then supplied to an image reconstruction algorithm and the distribution of intra-thoracic conductivity

changes is reconstructed. We present hereafter the underlying physics concepts and working principles of EIT image reconstruction, in particular of one-step linearized reconstruction as commonly used in *difference* EIT for clinical applications.

Let us consider the thorax as a medium of complex admittance $\gamma(\mathbf{x})$ (the inverse of impedance) into which electrical currents are injected at a fixed angular frequency ω . (The dependence on the spatial variable \mathbf{x} is implicit in the following for simplicity of notation.) As mentioned earlier, in the range of frequencies used by EIT, the reactive part of γ is negligible [47, 73], and therefore the medium can simply be characterized by its real-valued conductivity σ . During current injection, an electric field \mathbf{E} is set up in the medium and induces a conduction current density \mathbf{J} [8]. Both quantities are related by a continuum version of Ohm's law [73]:

$$\mathbf{J} = \sigma \mathbf{E}. \quad (4.1)$$

In absence of internal sources, the total current density in the medium is \mathbf{J} , and it is divergence-free [20]:

$$\nabla \cdot \mathbf{J} = 0. \quad (4.2)$$

Equation (4.2) is the *continuity equation* and basically states that the amount of charge entering the medium is equal to the amount of charge leaving it: as the medium is conductive, there is no accumulation of charge in it [8]. Furthermore, ω being sufficiently low in EIT for magnetic effects to be negligible, a quasi-electrostatic assumption (constant magnetic field) allows us to express \mathbf{E} purely in terms of a scalar electric potential ϕ [8, 73]:

$$\mathbf{E} = -\nabla \phi. \quad (4.3)$$

Combining (4.1), (4.2) and (4.3), we find the continuum version of Kirchhoff's law (Laplace equation) [73]:

$$\nabla \cdot \sigma \nabla \phi = 0. \quad (4.4)$$

From (4.4), finding a unique solution for ϕ given σ is then possible, given appropriate boundary conditions [73]. This is known as the *forward problem*. This system can only be solved analytically in cases of very simple medium geometries and conductivities [7]. However, for more general medium geometries and conductivity distributions, numerical methods are needed and therefore a discretization of the medium is required. This is typically performed using the finite element method, by approximating the medium geometry with a mesh of n_E tetrahedral elements [7]. Using the first-order finite element

method, the conductivity of the medium is discretized into a vector of element-wise constant conductivity values $\sigma \in \mathbb{R}^{n_E}$. The potential ϕ can then be approximated by functions which are linear on each element and continuous across the faces (by analogy with Kirchhoff's law) [73]. The potential ϕ being thus piecewise-defined is not differentiable, which prevents solving (4.4). However, using the weak form of the equation allows circumventing the issue and leads to a solvable linear system of equations [73].

The process of obtaining the surface voltages \mathbf{v} resulting at the electrodes given a supposedly known internal distribution of conductivity σ can be described via the so-called forward operator $\mathcal{F}: \mathbb{R}^{n_E} \mapsto \mathbb{R}^{n_M}$:

$$\mathbf{v} = \mathcal{F}(\sigma). \quad (4.5)$$

Obviously, in EIT the problem is reversed (*inverse problem*): the internal distribution of conductivity σ is unknown and the EIT reconstruction process aims at assessing it from a set of n_M voltages $\mathbf{v}_m \in \mathbb{R}^{n_M}$ measured at the surface electrodes. The simplest solution is to find the conductivity distribution that minimizes the difference between $\mathcal{F}(\sigma)$ and \mathbf{v}_m in a least square sense ($\|\cdot\|$ is the standard 2-norm) [73]:

$$\hat{\sigma} = \arg \min_{\sigma} \|\mathcal{F}(\sigma) - \mathbf{v}_m\|^2. \quad (4.6)$$

However, solving (4.6) is doomed to fail as the problem is *ill-posed* [73]: there are more unknowns than measurements ($n_E > n_M$) and the solution is not unique. Moreover, the problem is *ill-conditioned*: as current density is larger near the surface, EIT is more sensitive to unwanted information (e.g. skin-electrode impedance imbalance) than to the phenomena of interest (intra-thoracic conductivity changes). Addressing these issues is done by *regularizing* the problem, i.e. by introducing some assumptions and restrictions in order to ensure numerical stability and smoothness of the solution [73]. To do so, the usual approach is to use Tikhonov regularization:

$$\hat{\sigma} = \arg \min_{\sigma} \|\mathcal{F}(\sigma) - \mathbf{v}_m\|^2 + \lambda^2 \|\Gamma(\sigma - \sigma_r)\|^2. \quad (4.7)$$

The positive scalar λ is called the regularization parameter, and controls the trade-off between accuracy of the solution (low λ) and numerical stability (high λ). The term $\|\Gamma(\sigma - \sigma_r)\|^2$ allows penalizing solutions that differ too much from an *a priori* reference conductivity distribution σ_r . The regularization matrix $\Gamma \in \mathbb{R}^{n_E \times n_E}$ may be chosen to be the identity matrix to penalizes large conductivity deviations from σ_r , or a difference operator to ensure smoothness of the solution [73]. The choice of σ_r can for instance be based on a priori knowledge of the internal distribution of anatomical structures and of their average electric properties.

As mentioned earlier, it is convenient in medical EIT to make use of *difference* data, namely conductivity and voltage *changes* around reference working points σ_r and \mathbf{v}_r , that is $\Delta\sigma = \sigma - \sigma_r$ and $\Delta\mathbf{v} = \mathbf{v} - \mathbf{v}_r$. The use of *difference* data provides several advantages, such as a reduced variance between acquisition channels (*e.g.* due to component variability and aging) and skin-electrode impedances [8], and the possibility to *linearize* the EIT problem around the aforementioned working points. Besides, obtaining absolute conductivity values is not only of great complexity but typically not necessary for EIT-based biomedical applications, which are more interested in *functional* information (conductivity variations around a working point are thus sufficient for that purpose). In practice, the voltage working point \mathbf{v}_r is typically estimated by averaging the voltages of a few frames of an EIT recording when the physiology is presumed stable and, by definition, is hypothesized to correspond to the conductivity working point σ_r , *i.e.* $\mathbf{v}_r = \mathcal{F}(\sigma_r)$ via equation (4.5). It follows:

$$\begin{aligned}\Delta\mathbf{v} &= \mathcal{F}(\Delta\sigma), \\ &\approx \mathbf{S}\Delta\sigma,\end{aligned}\tag{4.8}$$

where $\mathbf{S} \in \mathbb{R}^{n_M \times n_E}$ is the so-called sensitivity matrix and is obtained through the linearization of the forward operator \mathcal{F} around the working point σ_r [8]. In practice, \mathbf{S} is calculated from the finite element mesh as the sensitivity of each i -th voltage measurement to a change in conductivity in the j -th mesh element:

$$[\mathbf{S}]_{ij} = \left. \frac{\partial[\Delta\mathbf{v}]_i}{\partial[\Delta\sigma]_j} \right|_{\sigma_r}.\tag{4.9}$$

Equation (4.7) can now be rewritten as:

$$\widehat{\Delta\sigma} = \arg \min_{\Delta\sigma} \|\mathbf{S}\Delta\sigma - \Delta\mathbf{v}_m\|_{\mathbf{P}}^2 + \lambda^2 \|\Delta\sigma\|_{\mathbf{Q}}^2.\tag{4.10}$$

The matrix $\mathbf{P} \in \mathbb{R}^{n_M \times n_M}$ is a weighting matrix controlling the influence each measurement has in the computation of the errors, by giving less weight to noisier or erroneous measurements. It is often determined automatically (*e.g.* by measuring reciprocity errors) and/or from *a priori* considerations (*e.g.* knowledge of faulty electrodes) [66]. The matrix $\mathbf{Q} \in \mathbb{R}^{n_E \times n_E}$ is a regularization matrix that favors smooth solutions, as the limited number of measurements in EIT prevents resolving high spatial frequency details [8]. \mathbf{Q} can for instance be implemented as a discrete Laplacian filter [168]. Other choices exist, such as the NOSER prior [32], which scales \mathbf{Q} with the sensitivity of each element using \mathbf{S} to cope with the larger sensitivity of EIT at the boundaries [5]. By solving (4.10), a

linearized one-step solution is obtained as [73]:

$$\begin{aligned}\widehat{\Delta\sigma} &= (\mathbf{S}^T \mathbf{P} \mathbf{S} + \lambda^2 \mathbf{Q})^{-1} \mathbf{S}^T \mathbf{P} \Delta \mathbf{v}_m \\ &= \mathbf{R} \Delta \mathbf{v}_m\end{aligned}\tag{4.11}$$

where $\mathbf{R} \in \mathbb{R}^{n_E \times n_M}$ is the so-called reconstruction matrix for one-step linearized EIT. One-step linearized reconstruction algorithms, as opposed to most non-linear and/or iterative algorithms, allow real-time imaging of the thorax, with image sampling rates typically ranging between 10 and 50 frames per second, depending on the system and the application [6].

4.4 Commercially available EIT systems

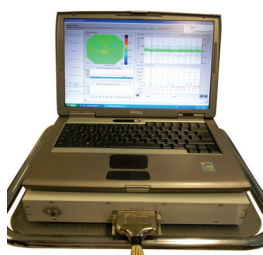
Many research-oriented EIT systems dedicated to lung monitoring have been developed over the last decades (see [55] for an exhaustive list). At present only few systems are commercially available (see Table 4.1).

4.4. Commercially available EIT systems

Table 4.1 – Commercial EIT systems.



System: ENLIGHT[®] 1800
Distributed by: Timpel, São Paulo, Brazil
Electrodes: individual, passive
Number of electrodes: 32
Current frequency: 125 kHz
Imaging rate: 50 images/s



System: Goe MF II
Distributed by: CareFusion, Höchberg, Germany
Electrodes: individual, passive
Number of electrodes: 16
Current frequency: 5–500 kHz
Imaging rate: 13, 25, 33, or 48 images/s



System: PulmoVista[®] 500
Distributed by: Dräger Medical, Lübeck, Germany
Electrodes: stretchable elastic belt, passive
Number of electrodes: 16
Current frequency: 80–130 kHz
Imaging rate: 10, 20, 30, 40, or 50 images/s



System: Sheffield MK 3.5
Distributed by: Maltron International, Rayleigh, UK
Electrodes: individual, passive
Number of electrodes: 8
Current frequency: 2–1600 kHz
Imaging rate: 25 images/s



System: Swisstom BB²
Distributed by: Swisstom AG, Landquart, Switzerland
Electrodes: textile belt, active
Number of electrodes: 32
Current frequency: 125–175 kHz
Imaging rate: flexible, up to 50 images/s

Cardiac output by electrical impedance tomography **Part II**

5 Influence of heart motion on the EIT-based measurement of CO

Adapted from the post-print version of [133]:

Influence of heart motion on cardiac output estimation by means of electrical impedance tomography: a case study

Martin Proença^{1,2}, Fabian Braun^{1,2}, Michael Rapin^{1,3}, Josep Solà¹, Andy Adler⁴, Bartłomiej Grychtol⁵, Stephan H. Böhm⁶, Mathieu Lemay¹, and Jean-Philippe Thiran^{2,7}

¹Systems Division, Centre Suisse d'Electronique et de Microtechnique (CSEM), Neuchâtel, Switzerland

²Signal Processing Laboratory (LTS5), Ecole Polytechnique Fédérale de Lausanne (EPFL), Lausanne, Switzerland

³Department of Health Sciences and Technology (D-HEST), Swiss Federal Institute of Technology (ETHZ), Zürich, Switzerland

⁴Systems and Computer Engineering, Carleton University, Ottawa, Canada

⁵Fraunhofer Project Group for Automation in Medicine and Biotechnology, Mannheim, Germany

⁶Swisstom AG, Landquart, Switzerland

⁷Department of Radiology, University Hospital Center (CHUV) and University of Lausanne (UNIL), Lausanne, Switzerland

Published in **Physiological Measurement**

Physiol. Meas., vol. 36, no. 6, pp. 1075–1091, 2015

5.1 Introduction

5.1.1 Objectives

In Chapter 3, we have introduced the limitations of current CO monitoring solutions. The use of the gold standard PAC thermodilution method in clinical settings has, for the last two decades, become controversial due to the lack of evidence of improved patient outcomes following its use [67, 107]. Besides, its time resolution is insufficient to provide continuous monitoring during hemodynamic instability [36, 131]. Finally, current non-invasive beat-to-beat monitors are limited by their sensitivity to physiological phenomena unrelated to CO, thus requiring frequent recalibration maneuvers, whenever changes in the patient’s hemodynamic status may have occurred [91, 131, 177].

In the present study, we investigate the potential and accuracy of EIT for the non-invasive and continuous measurement of CO.

5.1.2 Measurement principle and study goal

We have seen in Section 3.1 that several modalities for CO measurement are based on the joint estimation of stroke volume (SV) and heart rate, as CO is the product of both parameters. Thus, the main technical challenge resides in the non-invasive estimation of SV, as heart rate is easy to assess non-invasively. In the present study, we investigate the feasibility of using EIT for SV estimation. This approach is based on the hypothesis illustrated in Figure 5.1, *i.e.* that the EIT-derived conductivity change in the ventricular region $\Delta\sigma$ – hereafter referred to as “EIT heart signal” – is representative of changes in ventricular blood volume, and therefore its peak-to-peak amplitude $\Delta\sigma_{\max}$ over the cardiac cycle, representative of SV. The goal of the present study is to investigate the validity of this hypothesis.

Previous work. The determination of SV by means of EIT was first reported by Vonk-Noordegraaf *et al* [174]. Through multivariate regression, an indirect correlation between SV and $\Delta\sigma_{\max}$ was found. Zlochiver *et al* [185] proposed a parametric approach where the axes of an ellipsis representing the left ventricle were iteratively optimized from the analysis of the impedances measured. High correlation with the reference was found despite some limitations: the use of impedance cardiography as reference, and the dependency of their approach on anatomical and conductivity a priori assumptions. A similar approach was used by Rashid *et al* [140] who expressed the boundary of the left ventricle as truncated Fourier series coefficients, and used a first-order kinematic model as state evolution model. A recent publication [129] found significant correlation coefficients between SV and a cardiac impedance change derived from principal component analysis. However, due to unresolved issues in their results (unexpected scaling effects), the authors highlighted the need for further investigations before considering

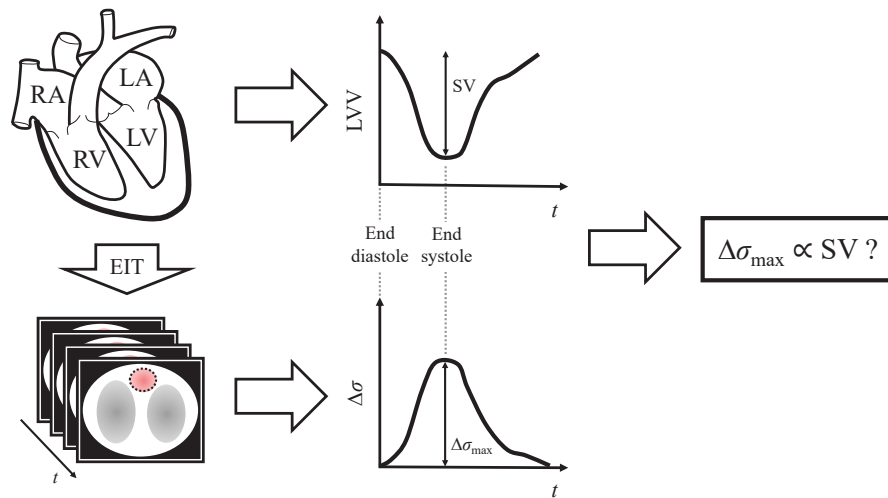


Figure 5.1 – Stroke volume (SV) monitoring by EIT: measurement principle and hypothesis. The EIT heart signal $\Delta\sigma$ is hypothesized to be representative of changes in left ventricular volume (LVV), or ventricular volume in general. As a consequence, its peak-to-peak amplitude $\Delta\sigma_{\max}$ is assumed to be representative of SV, *i.e.* the peak-to-peak change in LVV.

the transfer of their technique into clinical practice.

These studies differ in their approach for computing an SV-related quantity. In particular, the non-parametric approaches in [129] and [174] did not find a direct relation between $\Delta\sigma_{\max}$ and SV, suggesting that the hypothesis in Figure 5.1 might be incorrect, or at least incomplete. The exact sources contributing to the genesis of $\Delta\sigma$ appear to be still unclear and subject to interpretation. Yet, the correct interpretation of impedance-derived parameters requires a fundamental understanding of the physiological origin of the signals being measured.

Origins of pulsatile EIT signals in the heart region. The exact origin of pulsatile conductivity changes in EIT remains subject to interpretation [52]. Many potential cardio-synchronous sources of conductivity change (such as atrial and ventricular blood volume changes, arterial distensibility and pulsatility, or blood flow) act in concert within the thorax. In the heart region, the hypothesis in Figure 5.1 assumes $\Delta\sigma$ to be solely induced by changes in ventricular blood volume. However, recent investigations in pigs [23] suggest that *heart motion* (cardiobalistic effects) may play a significant role in the genesis of $\Delta\sigma$. Indeed, as myocardial deformation occurs over the cardiac cycle, interactions between the myocardium and low conductivity tissues (mostly adipose and lung tissues) at the periphery of the heart generate cardio-synchronous conductivity changes that directly contribute to the genesis of $\Delta\sigma$, but are not caused directly by variations in blood volume. Isolating these motion-induced changes from those caused by variations in blood volume is virtually impossible, as strong mechanical (*e.g.* myocardial deforma-

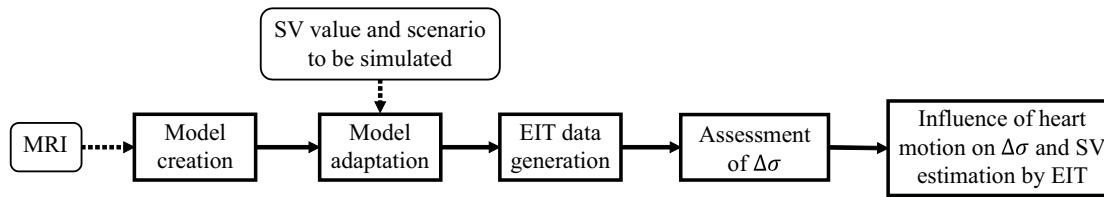


Figure 5.2 – Overview of the simulation and analysis process for the present study. See text (beginning of Section 5.2) for details.

tion and ventricular volume change) and physiological (*e.g.* cardiac inotropy and SV) interdependencies link both of these two factors [86]. Simulations on a dynamic model to quantify the contribution of each factor to the genesis of $\Delta\sigma$ are therefore suggested.

The goal of this study is thus twofold: (1) to provide, through simulations on a dynamic model, a better understanding of the origins of the EIT heart signal $\Delta\sigma$, in particular by quantifying and characterizing the influence of heart motion in its genesis; and (2) to evaluate via the model the validity of using $\Delta\sigma$ as an estimator of left ventricular volume (LVV), and thus of using $\Delta\sigma_{\max}$ for SV estimation.

Section 5.2 describes the creation of the model and the EIT simulations performed. The simulation results are presented in Section 5.3 and discussed in detail in Section 5.4.

5.2 Methods

Figure 5.2 shows an overview of the simulation and analysis process used in the present study. From segmented magnetic resonance imaging (MRI) scans, a dynamic bioimpedance model is created. The model can be adapted via two parameters: the SV value to be simulated, and the “scenario”, which controls the amount of heart motion in the cardiac region. The adapted model is then used to perform EIT simulations for each SV value and scenario considered, and the EIT heart signal $\Delta\sigma$ is automatically assessed from the EIT images. The influence of heart motion on $\Delta\sigma$ and on $\Delta\sigma$ -based SV estimation is then investigated.

5.2.1 Influence of heart motion: three scenarios

The scenario is one of the two parameters of the model (along with the simulated SV value), and controls the amount of heart motion. Throughout the whole study, three scenarios are considered. Two of them (scenarios A and B) are physiologically unrealistic. In A, only blood volume changes are occurring in the heart, but no heart motion is present, *i.e.* there is no mechanical interaction of the outer myocardial surface with its surrounding tissues. Scenario B is the opposite of A: only heart motion is

present, and no blood volume changes occur in the heart. Finally, scenario C is the physiologically realistic scenario. In C, both blood volume changes and heart motion are present.

Scenarios A and B will allow us to isolate and thus quantify the individual effects that blood volume changes and heart motion have on $\Delta\sigma$. Scenario C will allow us to evaluate the performance of EIT for SV estimation in physiologically realistic conditions, *i.e.* when the EIT heart signal is a mixture of blood volume- and motion-related changes. The way these three scenarios are implemented will be detailed in the next section.

5.2.2 Dynamic bioimpedance model creation

MRI data acquisition and segmentation

The healthy subject enrolled in this experiment was an 83-kg, 183-cm, 50-year-old male with an under-bust girth of 100 cm. MRI scans were acquired with a 3T Philips Achieva instrument. ECG-gated scans were performed during breath-hold in an oblique plane along the long axis of the heart. A full cardiac cycle was imaged with a time resolution of 43 ms, resulting in a total of 20 2D image slices. The spatial resolution in the mediolateral and anteroposterior directions was 0.94 mm/pixel, and slice thickness 8 mm.

The cardiac cavities (atria and ventricles), the outer boundary of the myocardium, and the aorta were segmented manually in each of the 20 MRI frames representing the cardiac cycle. The lungs, fat, skeletal muscle, spine, and thorax contour were segmented manually in the first frame only. The aortic wall thickness was assumed to be 12 % of the segmented aortic radii [121] and the pericardium uniformly 2 mm thick [176]. The resulting segmentation can be seen in Figure 5.3a (for one frame of the cardiac cycle).

In addition, the segmented area and length of the left ventricle in each frame were used to compute the reference left ventricular volume LVV_{MRI} via the single-plane area-length method [166] (see Figure 5.3b).

Simulation of scenarios A, B, and C

Simulating the three scenarios described earlier in Section 5.2.1 can be done by modifying adequately the segmentation of the *inner* boundary of the myocardium (*i.e.* the boundary of the cardiac chambers), as well as its *outer* boundary. This process is illustrated in Figure 5.4. In short:

- a) In scenario A (where the EIT heart signal $\Delta\sigma$ is caused by changes in blood volume only), the segmentation of the myocardial *outer* boundary is “frozen” to its end-diastolic state for all 20 frames of the cardiac cycle. This suppresses conductivity

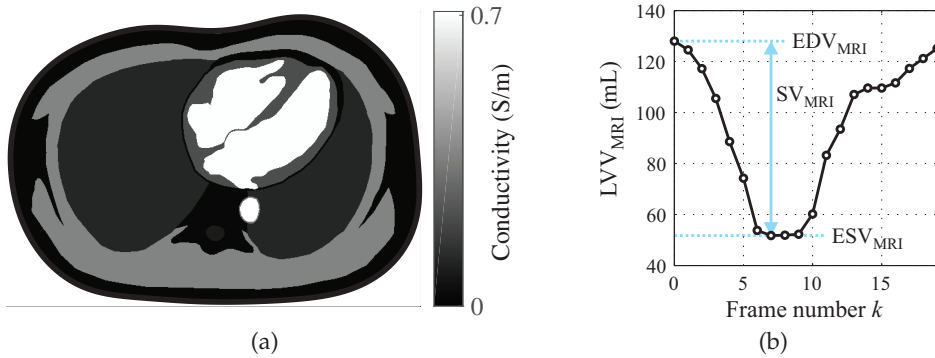


Figure 5.3 – (a) Example of an MRI-derived segmented frame of the dynamic model. For illustration purposes, each organ or tissue is colored using a gray level proportional to its electrical conductivity value. (b) Reference MRI-derived left ventricular volume LVV_{MRI} . The reference end-diastolic, end-systolic and stroke volumes are $EDV_{MRI} = 128$ mL, $ESV_{MRI} = 51.7$ mL and $SV_{MRI} = 76.3$ mL.

changes related to heart motion.

- b) In scenario B (where $\Delta\sigma$ is caused by heart motion only), the myocardial *inner* boundary is “frozen” to its end-systolic state for all 20 frames of the cardiac cycle. This suppresses conductivity changes related to blood volume variations.
- c) In scenario C, no modification is made to the segmentation, as scenario C depicts the realistic scenario.

Our segmentation can therefore be adapted depending on which scenario (A, B, or C) is to be simulated. However, just as our 20 MRI frames, the segmentation covers one cardiac cycle and therefore one corresponding SV value only (SV_{MRI}). Investigating the possibility of tracking changes in SV with EIT requires the possibility of changing this SV value. This can be done through appropriate modification of the segmentation, as described in the next section.

Simulation of SV changes

Simulating a different SV value can be achieved by *morphing* the segmentation of the heart at end diastole and end systole to different end-diastolic and end-systolic volumes, respectively. This process is detailed hereunder. It is worth mentioning that this only needs to be done for 2 frames of the cardiac cycle, namely frame 0 (end-diastolic frame) and frame 7 (end-systolic frame), since only the peak-to-peak amplitude of $\Delta\sigma$, namely $\Delta\sigma_{max}$, is needed for SV estimation, as illustrated earlier in Figure 5.1. The morphing process operates as follows.

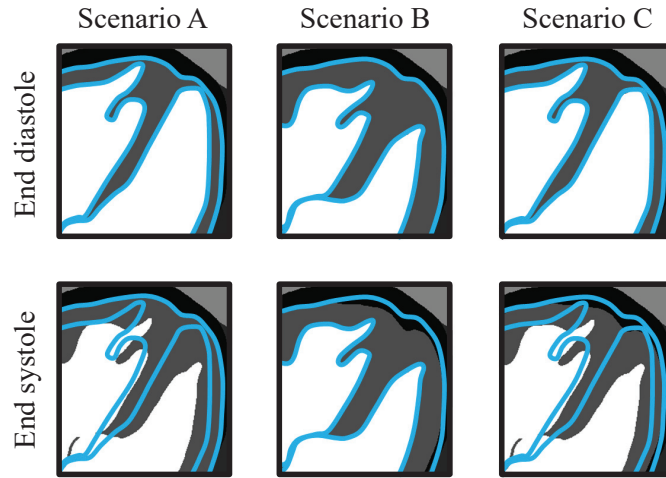


Figure 5.4 – Zoom on the segmentation of the ventricular region for each scenario at end diastole and end systole. The inner and outer boundaries of the myocardium at end diastole are shown in light blue in all images. In scenario A, the *outer* boundary of the myocardium is “frozen” to its end-diastolic state. In scenario B, the *inner* boundary of the myocardium is “frozen” to its end-systolic state. In scenario C (realistic scenario), no modification is made to the segmentation.

- a) For each 2D point located on the inner or outer boundary of the segmented myocardium at frame 0 (end-diastolic frame), its corresponding point is manually identified at frame 7 (end-systolic frame).
- b) Aggregating all these 2D boundary points into matrices at frame 0 and 7 leads to \mathbf{X}_0 and \mathbf{X}_7 , respectively.
- c) We then obtain a displacement matrix $\mathbf{Y} = \mathbf{X}_7 - \mathbf{X}_0$.
- d) Introducing the pair of parameters $\{\kappa, \lambda\}$ (both being equal to 1 for the moment), we can write $\mathbf{X}_0 = \mathbf{X}_7 - \kappa\mathbf{Y}$ and $\mathbf{X}_7 = \mathbf{X}_0 + \lambda\mathbf{Y}$.
- e) Simulating different SV values can then be done by morphing the segmentation \mathbf{X}_0 to a different end-diastolic volume value using $\mathbf{X}_0 = \mathbf{X}_7 - \kappa\mathbf{Y}$ with $\kappa \neq 1$, and/or by morphing the segmentation \mathbf{X}_7 to a different end-systolic volume value using $\mathbf{X}_7 = \mathbf{X}_0 + \lambda\mathbf{Y}$ with $\lambda \neq 1$.

Applying the procedure described above allows easily simulating SV values different from SV_{MRI} . For scenario A, the procedure is applied only for the *inner* boundary of the myocardium. For scenario B, it is applied only for its *outer* boundary.

A given segmentation is thus characterized by two parameters: the SV value and the scenario simulated. The next section describes how – for a given segmentation – the corresponding bioimpedance model is created.

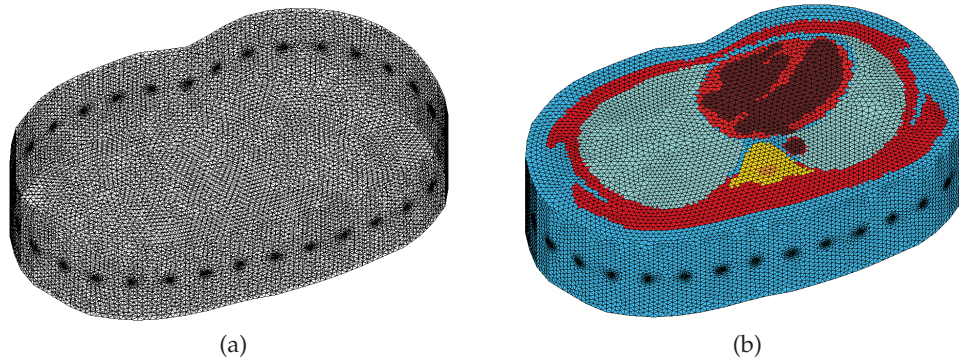


Figure 5.5 – Mesh of the 2.5D dynamic bioimpedance model before (a) and after (b) assigning a conductivity value to each of its finite element.

Table 5.1 – Conductivity value of tissues at 100 kHz [68].

Tissue	Conductivity (S/m)	Tissue	Conductivity (S/m)
Blood	$7.03 \cdot 10^{-1}$	Lungs	See Figure 5.6a
Blood (aorta)	See Figure 5.6b	Spinal cord	$8.08 \cdot 10^{-2}$
Skeletal muscle	$3.62 \cdot 10^{-1}$	Fat	$2.44 \cdot 10^{-2}$
Aortic wall	$3.19 \cdot 10^{-1}$	Vertebrae	$2.08 \cdot 10^{-2}$
Myocardium	$2.15 \cdot 10^{-1}$		

Model creation

The model creation process and all ensuing EIT simulations are carried out using Matlab (MathWorks, Natick, USA) and the framework of the EIDORS toolbox [4]. A 2.5D (2D extruded) fine mesh fitting the subject's segmented thorax contour is generated using the dedicated function [62] of the EIDORS toolbox (Figure 5.5a). A total of $\sim 4.6 \cdot 10^5$ tetrahedral elements with an average edge length of 5.1 mm are obtained. At each k -th frame, each finite element of the mesh is assigned an electrical conductivity value of the organ or tissue its center belongs to (by considering an extrusion of the segmentation to 3D) in the time laps of the current frame (Figure 5.5b). The biological values of electrical conductivity used in this model are listed in Table 5.1.

Pulmonary and aortic conductivity changes. The model implements conductivity changes purely related to cardiovascular activity, as the MRI scans were acquired during breath-hold using ECG gating. The conductivity changes in the lungs are thus purely induced by the pulsatility of the pulmonary arteries, and their conductivity varies according to the curve depicted in Figure 5.6a. In the aorta, the conductivity depends both on the distension-induced change in blood volume, and the flow-induced change in blood conductivity [170]. While the former is directly determined in the model by the MRI-obtained area change of the aorta over the cardiac cycle, the later is controlled by

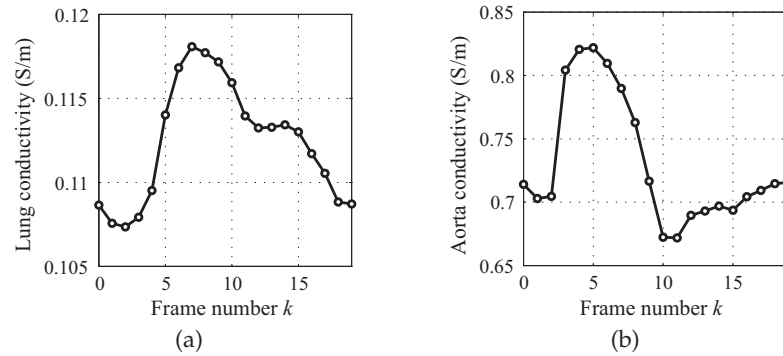


Figure 5.6 – (a) Pulmonary conductivity change over the cardiac cycle, based on the waveform measured by [173], set to a baseline (end-diastolic) conductivity value of $1.07 \cdot 10^{-1}$ S/m [68] and scaled in order to produce a conductivity change of 10 % [27]. (b) Aortic conductivity change over the cardiac cycle, computed via Visser’s model [170] using an MRI-based blood flow curve and aortic radii measured in a healthy subject. The conductivity curve is set to a baseline value of $7.03 \cdot 10^{-1}$ S/m [68] and scaled in order to produce a conductivity change of 15 % [138].

the conductivity curve in Figure 5.6b.

5.2.3 EIT simulations

EIT data generation: the forward problem

EIT relies on the application of small alternating electrical currents and peripheral voltage measurements \mathbf{v} to estimate the intra-thoracic conductivity distribution σ . In the present study, EIT voltages \mathbf{v} are obtained using EIDORS with a 32-electrode stimulation and measurement pattern where each injecting or measuring pair of electrodes is separated by four non-injecting or non-measuring electrodes, respectively [55]. The default EIDORS first-order forward solver is used to generate the voltages \mathbf{v} .

EIT image reconstruction: the inverse problem

As is convenient for biomedical applications of EIT, we make use of *difference* EIT reconstruction (previously introduced in Chapter 4) in the present study. Image reconstruction is performed using the GREIT algorithm with the recommended parameters [5]. Difference data are obtained by using the first frame (representing end diastole) as reference data set, resulting in sequences of 40×60 pixel images after image reconstruction.

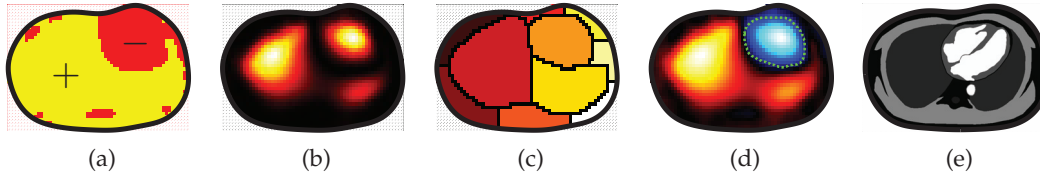


Figure 5.7 – Automatic segmentation of the ventricular ROI. (a) A *sign* image is computed as the sign of the average conductivity value at each pixel over the cardiac cycle. As the reference EIT frame corresponds to end diastole, a negative sign indicates that – on average – conductivity decreases over the course of the cardiac cycle. As the ventricles are filled with blood at end diastole and empty during systole, a negative sign is expected in the ventricular ROI. (b) A power image is then computed as the pixel-wise variance of the conductivity change across time and (c) is segmented using the watershed algorithm [113] as proposed by Ferrario *et al* [45]. (d) The watershed region containing the negative-sign pixel with maximal cardiac power is defined as the ventricular ROI (green dotted line). (e) For visual comparison, a segmented frame (the same as in Figure 5.3a) is shown.

5.2.4 Automatic extraction of $\Delta\sigma$ in EIT image sequences

Automatically obtaining $\Delta\sigma$ from an EIT image sequence first requires the automatic extraction of the ventricular region of interest (ROI). The ROI is computed in scenario C (realistic scenario). This process is illustrated and detailed in Figure 5.7. At each k -th frame, the total conductivity change in the ventricular region $\Delta\sigma[k]$ is computed by summing the conductivity change of all pixels within the ROI.

5.2.5 Simulated SV values

As explained earlier, the model is controlled by two parameters: the SV value and the scenario (A, B, or C) simulated. In the present study, 11 physiologically realistic stroke volumes¹ are simulated, and listed in Table 5.2. They are hereafter referred to as SV_i ($i \in \{1, \dots, 11\}$), with SV_1 corresponding to SV_{MRI} , the original SV value obtained from the MRI scans. SV_2 to SV_{11} simulate SV values induced by changes in cardiac preload, afterload, or inotropy. Hereafter, the $\Delta\sigma$ curve obtained with SV_i and scenario X ($X \in \{A, B, C\}$) will be referred to using the notation $\Delta\sigma_i^{(X)}$. The peak-to-peak amplitude of $\Delta\sigma_i^{(X)}$ will be referred to as $\Delta\sigma_{i,max}^{(X)}$.

¹The physiological interdependent effects of preload, afterload and cardiac inotropy on SV (described earlier in Section 2.2.5) are taken into account [86].

5.2.6 Analysis protocol

Analysis 1: Contribution of heart motion to the genesis of $\Delta\sigma$

This first analysis aims at quantifying the influence (*i.e.* the *contribution* in terms of amplitude) of heart motion to the genesis of $\Delta\sigma$. To do so, the peak-to-peak amplitudes $\Delta\sigma_{1,\max}^{(A)}$ and $\Delta\sigma_{1,\max}^{(B)}$ of the EIT heart signal in scenarios A and B are compared. The contribution (percentage of the total amplitude change) of heart motion to the EIT heart signal is estimated as $\Delta\sigma_{1,\max}^{(B)} / (\Delta\sigma_{1,\max}^{(A)} + \Delta\sigma_{1,\max}^{(B)})$.

Analysis 2: Impact of heart motion on the morphology of $\Delta\sigma$

This analysis aims at evaluating the closeness of fit between the EIT heart signal $\Delta\sigma$ and left ventricular volume (LVV) at various levels of heart motion, as using $\Delta\sigma_{\max}$ for SV estimation implicitly requires $\Delta\sigma$ to be representative of LVV. To do so, for each scenario X, $\Delta\sigma_1^{(X)}$ is fitted onto LVV_{MRI} (least-square linear fit); the root mean square error (RMSE) and Pearson's correlation coefficient between both curves are then computed.

Analysis 3: Impact of heart motion on EIT-based SV estimation

This analysis aims at evaluating the accuracy of EIT-based SV estimation at various levels of heart motion. To do so, Pearson's correlation coefficient between the simulated SV_i values and their corresponding $\Delta\sigma_{i,\max}^{(X)}$ in all three scenarios is evaluated. Furthermore, using a 1-point calibration (the MRI-derived SV_1 value and its corresponding $\Delta\sigma_{1,\max}^{(X)}$ value), all $\Delta\sigma_{i,\max}^{(X)}$ values are converted to milliliters, resulting in an EIT-based estimate of SV for each scenario as follows:

$$\text{SV}_{\text{EIT}_i}^{(X)} = \Delta\sigma_{i,\max}^{(X)} \cdot \frac{\text{SV}_1}{\Delta\sigma_{1,\max}^{(X)}}, \quad (5.1)$$

where $\text{SV}_1 / \Delta\sigma_{1,\max}^{(X)}$ is the 1-point scaling (calibration) factor. The error (mean \pm SD), both absolute (in milliliters) and relative (as a percentage), is calculated between $\text{SV}_{\text{EIT}_i}^{(X)}$ and SV_i for each scenario.

5.3 Results

For illustrative purposes, examples of reconstructed EIT images for various SV_i values and for the three scenarios are shown in Figure 5.8.

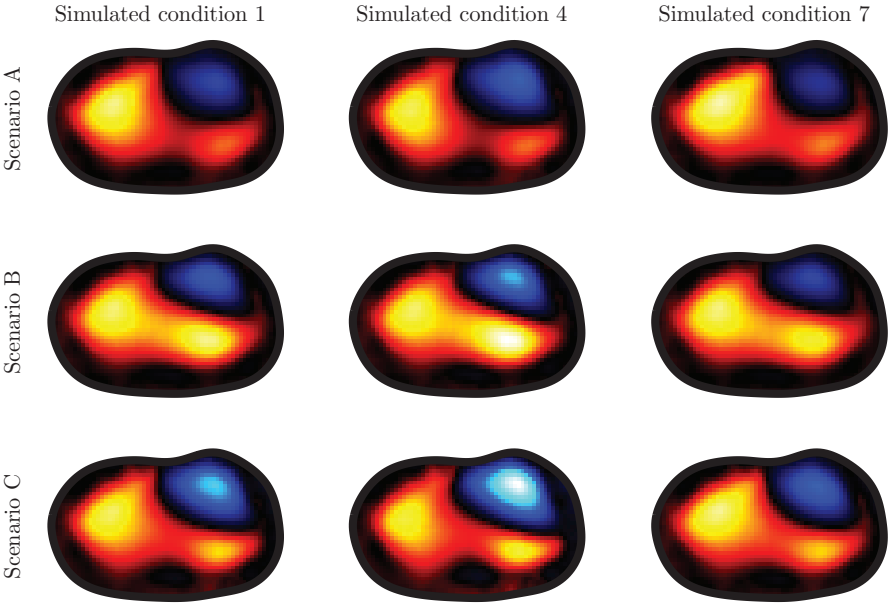


Figure 5.8 – End-systolic reconstructed EIT frame for the three scenarios in various conditions (see Table 5.2): the baseline condition (1) and the two conditions (4 and 7) showing the most extreme SV_i values. The blue and red colors respectively depict decreases and increases in conductivity with respect to the reference (end-diastolic) frame. The color scale is the same for all images.

Table 5.2 – Simulated SV values (adapted from [86]). EDV and ESV represent the end-diastolic and end-systolic volumes, respectively. The “Baseline” condition represents the original volumes obtained from the MRI data (Figure 5.3b).

i	Description	EDV $_i$ (mL)	ESV $_i$ (mL)	SV $_i$ (mL)
1	Baseline	128.0	51.7	76.3
2	Preload (small increase)	144.0	54.3	89.7
3	Preload (moderate increase)	160.0	56.9	103.1
4	Preload (large increase)	176.0	59.5	116.5
5	Preload (small decrease)	114.6	46.5	68.1
6	Preload (moderate decrease)	101.3	41.3	60.0
7	Preload (large decrease)	88.0	36.2	51.8
8	Afterload (increase)	138.7	67.2	71.5
9	Afterload (decrease)	122.7	41.4	81.3
10	Inotropy (increase)	117.3	36.2	81.1
11	Inotropy (decrease)	144.0	72.4	71.6

5.3.1 Contribution of heart motion to the genesis of $\Delta\sigma$ (Analysis 1)

The EIT heart signal $\Delta\sigma_1^{(X)}$ is depicted for each scenario in Figure 5.9a. The peak systolic amplitude $\Delta\sigma_{1,\max}^{(X)}$ is found to be 0.84, 1.08, and 1.99 A.U. for scenarios A, B, and C, respectively. The contribution of heart motion to the EIT heart signal is therefore $\Delta\sigma_{1,\max}^{(B)} / \left(\Delta\sigma_{1,\max}^{(A)} + \Delta\sigma_{1,\max}^{(B)} \right) = 1.08 / (0.84 + 1.08) \simeq 56.3\%$.

5.3.2 Impact of heart motion on the morphology of $\Delta\sigma$ (Analysis 2)

The linear least-square fit of $\Delta\sigma_1^{(X)}$ onto LVV_{MRI} is shown in Figure 5.9b (only for the realistic scenario C for the sake of clarity). The RMSE between both curves is found to be 27.7 mL, 25.4 mL, and 21.6 mL for scenarios A, B, and C respectively. In the same order, Pearson’s correlation coefficients of 0.973, 0.978, and 0.984 between both curves are obtained.

5.3.3 Impact of heart motion on EIT-based SV estimation (Analysis 3)

The correlation between $\Delta\sigma_{i,\max}^{(X)}$ and SV_i is shown in Figure 5.10a (for the realistic scenario C only). Figure 5.10b depicts the error on SV estimation for all three scenarios after converting $\Delta\sigma_{i,\max}^{(X)}$ into $SV_{\text{EIT}_i}^{(X)}$ using (5.1). The error (mean \pm SD) between $SV_{\text{EIT}_i}^{(X)}$ and SV_i is -0.66 ± 3.88 mL ($-0.62 \pm 4.43\%$), 1.67 ± 2.48 mL ($2.19 \pm 3.38\%$) and 0.57 ± 2.19 mL ($1.02 \pm 2.62\%$) for scenarios A, B, and C, respectively. In the same order, Pearson’s correlation coefficients of 0.984, 0.991, and 0.996 between both quantities are obtained.

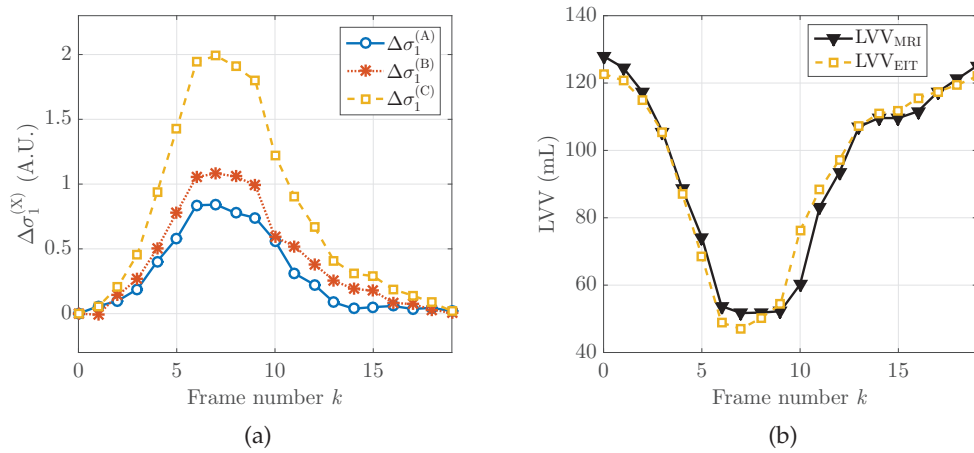


Figure 5.9 – (a) Conductivity change in the ventricular region $\Delta\sigma_1^{(X)}$ for all three scenarios. (b) Comparison (only shown for scenario C for the sake of clarity) between LVV_{MRI} and LVV_{EIT} , the least-square linear fit of $\Delta\sigma_1^{(C)}$ onto LVV_{MRI} .

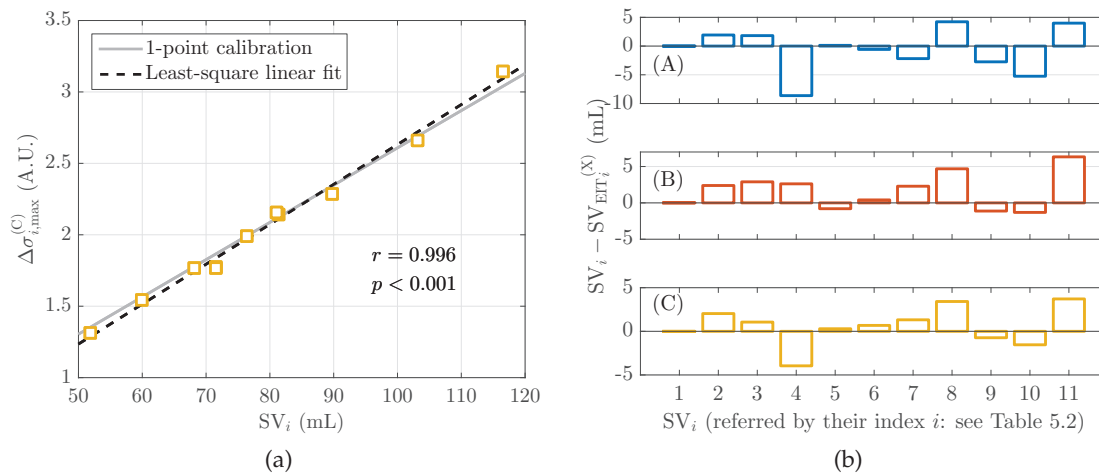


Figure 5.10 – (a) Simulated SV value vs. the resulting peak-to-peak amplitude of the EIT heart signal for the realistic scenario C. (b) Error between the simulated and estimated SV values for scenarios A, B, and C.

5.4 Discussion

A dynamic bioimpedance model was created for quantifying and characterizing the influence of heart motion on the genesis of the EIT heart signal $\Delta\sigma$. The influence of heart motion on the accuracy of EIT-based SV estimation was also evaluated.

5.4.1 Contribution of heart motion to the genesis of $\Delta\sigma$

From *Analysis 1*, the EIT heart signal $\Delta\sigma$ was found to be dominated by heart motion-induced changes, with a contribution of approximately 56 %. This joint presence of blood volume-related and heart motion-induced changes to the genesis of $\Delta\sigma$ can be explained as follows. During ventricular ejection, as illustrated in Figure 5.11, the myocardium contracts in the EIT ventricular ROI (light blue dashed line in the figure) and is progressively substituted – spatially speaking – by adipose and/or lung tissue [60], causing heart motion-related impedance changes. In the meanwhile, blood is substituted by myocardial tissue, causing blood volume-related changes. These two effects act in concert and decrease the global conductivity in the ventricular ROI. The opposite occurs in the atrial region, where the low-conductivity adipose and lung tissues are progressively substituted by the myocardium (heart motion-related changes), and the latter by blood (blood volume-related changes), thus increasing the global conductivity in the atrial region. The ventricular and atrial regions are separated by a zone of negligible conductivity change (between the two green dotted lines of the right panel in the figure). At end diastole, this zone is occupied by ventricular blood and is progressively substituted by atrial blood as the atrioventricular plane moves towards the apex during ventricular ejection [29]. Therefore, no significant conductivity change occurs in this region.

5.4.2 Impact of heart motion on the morphology of $\Delta\sigma$

Analysis 2 aimed at evaluating the influence of heart motion on the closeness of fit between LVV_{MRI} and $\Delta\sigma$. It was found that both blood volume-related changes $\Delta\sigma^{(A)}$ and heart motion-induced changes $\Delta\sigma^{(B)}$ strongly correlate with LVV_{MRI} ($r > 0.97$). This is also reflected by the very similar RMSE found in all scenarios after fitting $\Delta\sigma$ onto LVV_{MRI} , and the strong morphological resemblance between all curves in Figure 5.9a. We explain this strong correlation between heart motion-induced conductivity changes and LVV_{MRI} as follows. The myocardium and blood are nearly incompressible [18, 83]. Therefore, in the ventricular region, the deformation of the myocardial outer boundary *must* follow that of its inner boundary (*i.e.* the deformation of the ventricles), as no volume loss can occur. Consequently, conductivity changes occurring outside of the heart *reflect* changes occurring inside, *i.e.* changes in ventricular blood volume.

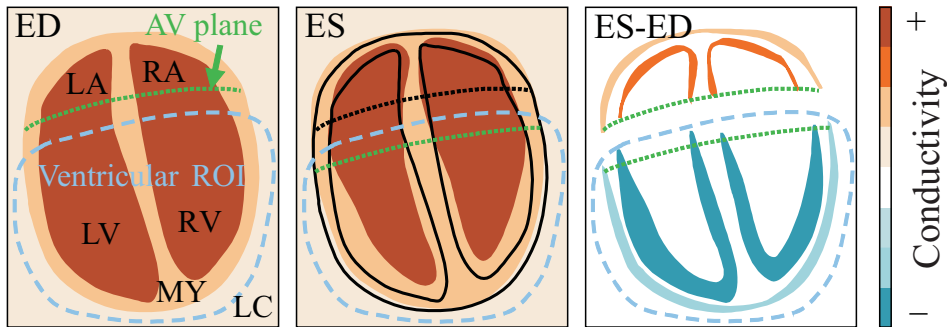


Figure 5.11 – Schematic illustration of the conductivity change in the heart region between end diastole (ED) and end systole (ES). The rightmost image depicts the difference of both aforementioned images, *i.e.* what *difference* EIT actually aims at reconstructing. The black lines in ES depict the outlines of ED. See Section 5.4.1 for details. LA: left atrium; RA: right atrium; LV: left ventricle; RV: right ventricle; AV plane: atrioventricular plane; MY: myocardium; LC: low-conductivity tissue (adipose or lung tissue).

5.4.3 Impact of heart motion on EIT-based SV estimation

Analysis 3 aimed at testing the feasibility of tracking changes in SV with EIT from the peak-to-peak amplitude of the EIT heart signal $\Delta\sigma_{\max}$. To do so, a wide range of physiologically realistic SV values were simulated. Strong correlation coefficients ($r > 0.98$) were found for all scenarios between $\Delta\sigma_{\max}$ and SV. After conversion of $\Delta\sigma_{\max}$ to milliliters using a 1-point calibration, the resulting errors on SV estimation were small enough to be clinically useful [36]. These results suggest that EIT can accurately monitor SV variations despite the dominantly heart motion-related origin of the EIT heart signal.

In summary, our observations suggest that the EIT heart signal is *not* dominantly *induced* by ventricular blood volume changes. However, it is *representative* of ventricular blood volume changes, due to the strong correlation between heart motion- and blood volume-induced impedance changes.

5.4.4 Implications of our observations

Impact of respiratory activity

We have explained in Section 5.4.1 that heart motion-induced impedance changes are due to the conductivity contrast between the myocardium and its surrounding tissues, mainly lung tissue. In our model based on ECG-gated MRI scans during *breath-hold*, variations in lung conductivity were limited to small changes induced by arterial pulsatility. However, in realistic scenarios, lung tissue conductivity varies much more due to respiratory activity; therefore, the contrast with myocardial tissue varies much more as well. In other terms, the amplitude of the motion-related component of the EIT

heart signal is *modulated* by lung conductivity changes, and thus by respiratory activity. This could affect the accuracy of the EIT-based measurement of SV. Similarly, other respiration-induced phenomena, such as the in- and out-of-plane motion of the heart or the deformation of the internal distribution of impedance volumes, may challenge the measurement. A possible workaround could consist in performing *respiration-gated* EIT measurements, for instance by only measuring $\Delta\sigma_{\max}$ at end of expiration. Such a solution could overcome the aforementioned respiration-induced limitations, at the cost of limiting the responsiveness of the EIT-based measurement of SV.

Impact of particular pathological conditions

On the other hand, our observations call into question the feasibility of EIT-based SV estimation in particular pathological conditions, such as large pericardial effusion (accumulation of fluid around the heart) [103]. In such cases, heart motion is not limited to the normal deformation of the myocardium, but also to its disease-induced *displacements* in the pericardial cavity. The resulting mechanical interactions of the heart with its surrounding tissues – unrelated to SV – are likely to significantly affect the EIT heart signal.

It is also worth mentioning that other pathologies, such as valvular insufficiencies, are likely to compromise the EIT-based measurement of SV. In such cases, SV is likely to be overestimated, as part of the ejected volume is pushed back into the atria (mitral/tricuspid regurgitation) or the ventricles (aortic/pulmonary regurgitation) at the end of ventricular ejection.

5.4.5 Limitations and future work

The main limitations of the model and study are listed hereafter.

- a) Given the aims of this study, only cardiovascular-related conductivity changes were modeled. Therefore, the aforementioned effects of respiratory activity on the accuracy of EIT-based SV estimation can only be described, but not formally quantified. To include respiration in a model – and all its aforementioned effects (such as in- and out-of-plane heart motion) – would require complex 4D modeling. We rather suggest to investigate this aspect in real clinical data.
- b) Another aspect not included in our model was the flow-induced change in blood conductivity in the cardiac chambers, due to the complexity of the modeling process. A future extension of the present model should aim at taking these effects into account.
- c) The model is 2.5D. Electrical currents are known to propagate in three dimensions.

Chapter 5. Influence of heart motion on the EIT-based measurement of CO

Conductivity changes occurring above and below the electrode plane are thus not necessarily considered adequately.

- d) No noise was included in the simulations. Its influence on the accuracy of SV estimation by EIT remains to be evaluated.
- e) The simulation of the different SV_i values (Table 5.2) using the morphing procedure described in Section 5.2.2 is limited by the linearity assumption of the latter. Extrapolating the original end-diastolic and end-systolic volumes to larger – respectively smaller – values is therefore only valid to a certain extent.
- f) The model is based on the morphology of one single subject. The generalizability of our observations should be verified in larger datasets.
- g) The influences of atrial, pulmonary and aortic conductivity changes on the EIT heart signal $\Delta\sigma$ have not been formally quantified. They can however be assumed to be small, given the spatial distance between the ventricular ROI and the other structures, as well as the strong correlation found between $\Delta\sigma$ and ventricular blood volume.

In our opinion, this last point should be thoroughly investigated in the future, as the plane imaged by EIT may not always be as optimal as the one used in the present study, where both the imaged ventricular “area” and the atrioventricular distance were large. In realistic clinical setups, managing to place the EIT electrode belt in that exact field of view without the assistance of another imaging modality seems hardly achievable. Future work should therefore focus on investigating the influence of sub-optimal belt placements and/or belt displacements, to quantify atrial, pulmonary and aortic pulsatile influence on $\Delta\sigma$, and verify the SV trending ability of EIT in those conditions.

In a second phase, measurements on humans should be performed to confirm our observations and validate the potential of EIT for non-invasive SV and CO monitoring. Particular attention should be given to the aforementioned influence of respiration on the EIT heart signal. We suggest the use of respiration-gating in the analysis process.

5.4.6 Summary and conclusion

Simulations were performed on a dynamic bioimpedance model to investigate the origins of the EIT heart signal $\Delta\sigma$. It was found that the main contributor to this change is heart motion, by approximately 56 %. It was further found that the motion-induced component of the EIT heart signal was strongly correlated ($r = 0.978$) with left ventricular volume. This observation was explained by the quasi-incompressibility of blood and myocardial tissue. Under those circumstances, EIT was found to be able to estimate SV (and thus CO) over a wide range of physiologically realistic values with

great accuracy. However, these observations were made using a model simulating intrathoracic bioimpedance changes during breath-hold and in a healthy heart. Respiratory activity may affect the accuracy of the measurement, through its influence on the motion-induced component of the EIT heart signal. This influence should be quantified in clinical data. Furthermore, the feasibility of the measurement is called into question in patients suffering from particular conditions such as large pericardial effusion.

6 Influence of belt position and displacement on the EIT-based measurement of CO

Adapted from the post-print versions of [22, 24, 25]:

Aortic blood pressure measured via EIT: investigation of different measurement settings

Fabian Braun^{1,2}, Martin Proença^{1,2}, Michael Rapin^{1,3}, Mathieu Lemay¹, Andy Adler⁴, Bartłomiej Grychtol⁵, Josep Solà¹, and Jean-Philippe Thiran^{2,6}

¹Systems Division, Centre Suisse d'Electronique et de Microtechnique (CSEM), Neuchâtel, Switzerland

²Signal Processing Laboratory (LTS5), Ecole Polytechnique Fédérale de Lausanne (EPFL), Lausanne, Switzerland

³Department of Health Sciences and Technology (D-HEST), Swiss Federal Institute of Technology (ETHZ), Zürich, Switzerland

⁴Systems and Computer Engineering, Carleton University, Ottawa, Canada

⁵Fraunhofer Project Group for Automation in Medicine and Biotechnology, Mannheim, Germany

⁶Department of Radiology, University Hospital Center (CHUV) and University of Lausanne (UNIL), Lausanne, Switzerland

Published in **Physiological Measurement**

Physiol. Meas., vol. 36, no. 6, pp. 1147–1159, 2015

4D heart model helps unveiling contributors to cardiac EIT signal

Fabian Braun^{1,2}, Martin Proença^{1,2}, Michael Rapin¹, Xenia Alba³, Karim Lekadir³, Mathieu Lemay¹, Josep Solà¹, Alejandro F. Frangi⁴, and Jean-Philippe Thiran^{2,5}

¹Systems Division, Centre Suisse d'Electronique et de Microtechnique (CSEM), Neuchâtel, Switzerland

²Signal Processing Laboratory (LTS5), Ecole Polytechnique Fédérale de Lausanne (EPFL), Lausanne, Switzerland

³Center for Computational Imaging and Simulation Technologies in Biomedicine, Universitat Pompeu Fabra, Barcelona, Spain

⁴Center for Computational Imaging and Simulation Technologies in Biomedicine, University of Sheffield, Sheffield, UK

⁵Department of Radiology, University Hospital Center (CHUV) and University of Lausanne (UNIL), Lausanne, Switzerland

Published in the proceedings of the 2015 International Conference on Biomedical Applications of Electrical Impedance Tomography (EIT 2015), Neuchâtel, Switzerland

EIT-derived stroke volume is impaired by belt displacement

Fabian Braun^{1,2}, Martin Proença^{1,2}, Josep Solà¹, Mathieu Lemay¹, and Jean-Philippe Thiran^{2,3}

¹Systems Division, Centre Suisse d'Electronique et de Microtechnique (CSEM), Neuchâtel, Switzerland

²Signal Processing Laboratory (LTS5), Ecole Polytechnique Fédérale de Lausanne (EPFL), Lausanne, Switzerland

³Department of Radiology, University Hospital Center (CHUV) and University of Lausanne (UNIL), Lausanne, Switzerland

Published in the proceedings of the 2016 International Conference on Biomedical Applications of Electrical Impedance Tomography (EIT 2016), Stockholm, Sweden

6.1 Introduction

In the previous chapter, the study was focused on the influence of heart motion on the EIT heart signal $\Delta\sigma$. However, some key aspects regarding the origins of $\Delta\sigma$ have not been investigated. For instance, the influence of atrial blood volume changes on $\Delta\sigma$ remains unknown. Indeed, the model presented in the previous chapter was based on MRI scans acquired along the long axis of the heart, where the spatial separation between the ventricles and the atria is maximized and is assumed to allow minimizing the influence of the atria on $\Delta\sigma$ [171]. In practice, managing to position an EIT electrode belt exactly along this axis can hardly be done without the use of another modality – such as CT scans – to verify the position of the belt. It is therefore necessary to investigate and quantify the influence of atrial conductivity changes on $\Delta\sigma$ when the belt is not placed in a plane maximizing atrioventricular separation. The same applies regarding the influence of conductivity changes induced by the pulsatility of the proximal pulmonary arteries or the aorta. These two sources were already included in our model, but their influence on $\Delta\sigma$ was negligible in the EIT plane considered.

This raises an important point, namely the extension of the model to the third dimension. Indeed, the use of 2D or 2.5D models requires creating a fully new model when a different belt position is investigated, as the plane imaged by EIT is different. A 3D model solves this issue by easily allowing to investigate various belt positions. In addition, it allows adequately considering the conductivity changes occurring above and below the electrode plane. Last but not least, a 3D model would also allow the investigation of another important aspect of SV by EIT, namely the repeatability of the measurement, particularly in case of displacement or repositioning of the electrode belt in-between measurements. Indeed, in a clinical context, the belt may occasionally be displaced (shifted by a few centimeters) during patient handling, or not be repositioned at the exact same place after having been momentarily removed. The influence of such belt displacements on the accuracy of SV by EIT has not been investigated.

The goals of this preliminary study are thus the following:

- a) To create a 3D dynamic (*i.e.* 4D) bioimpedance model of the human thorax easily allowing to investigate different belt positions;
- b) To quantify the contribution of the ventricles, the atria, the lungs and the aorta on the EIT heart signal $\Delta\sigma$;
- c) To confirm our previous findings, *i.e.* the feasibility of tracking changes in SV by EIT during breath-hold, on this complete 4D model;
- d) To investigate the influence of belt displacement or repositioning on the repeatability of the measurement.

6.2 Methods

The purpose of this section is to provide a summarized description of the 4D bioimpedance model. A detailed description of the various structures and functionalities of the model can be found in [22, 24, 25]. Similarly, the various simulations and analyses performed – extensively described in the three aforementioned studies – will be provided in a summarized form here.

6.2.1 Thoracic bioimpedance model

The anatomy of the model was based on MRI recordings performed on a healthy male volunteer (62 kg, 178 cm, 28 years old) during expiratory breath-hold. The outer surfaces of the thorax and the lungs were segmented from static whole-thorax 3D scans, whereas the geometrical deformations of the cardiac chambers and the aorta were segmented from 4D ECG-gated scans. While the conductivity changes induced by the pulsatility of the heart and the aorta were directly dictated by their geometrical deformations over the cardiac cycle, the conductivity changes induced by the pulsatility of the pulmonary arterial tree was modeled using a time- and location-dependent curve of conductivity change based on a simplified model of the pulmonary circulation. Finally, in order to investigate the influence of belt displacements, six EIT belts – each comprised of 32 electrodes – were applied onto the thorax mesh (see Figure 6.1). (1) The TM (*transversal middle*) belt was placed at the average level of the heart, which is in between the 9-th and 10-th thoracic vertebra. The belts (2) TH (*transversal high*) and (3) TL (*transversal low*) were placed 3.5 cm higher and lower than TM, respectively. This corresponds to the level of the 8-th (for TH) or in between the 10-th and 11-th (for TL) thoracic vertebrae. The belts (4) TLM and (5) THM were placed midway between TL and TM, and TH and TM, respectively. Finally, (6) the OB (*oblique*) belt was obtained by tilting the TM belt by 25° from transverse to coronal as suggested for cardiac EIT by Vonk-Noordegraaf *et al* [171], who hypothesized this angle to be optimal for imaging the heart along its longitudinal axis, and thus for optimizing the separation between the atria and the ventricles. To ensure accurate calculations, the mesh was refined in the vicinity of the electrodes as described in [63].

6.2.2 Bioimpedance simulations and EIT reconstruction

All simulations were performed with Matlab (MathWorks, Natick, USA) using the framework of the EIDORS toolbox [4]. All impedance measurements were simulated using a quasi-adjacent stimulation pattern with four inactive electrodes in between the two ones actively measuring voltage/injecting current [55]. The simulated impedance measurements were reconstructed to EIT images with the GREIT algorithm [5] and inverse models generated at the height of each belt from a coarser version of the static

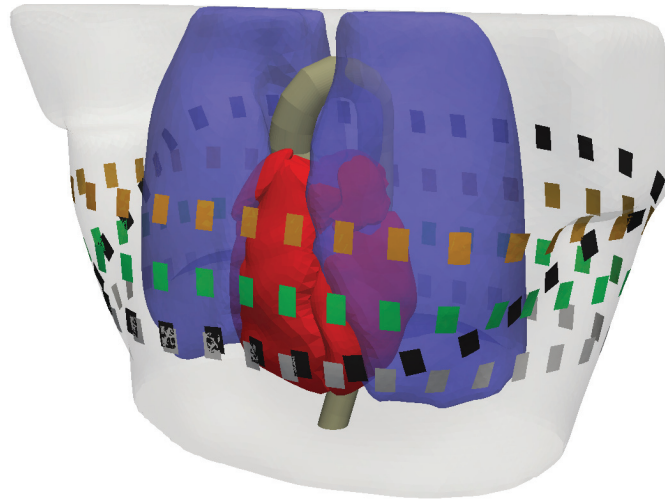


Figure 6.1 – 4D thoracic bioimpedance model. The model includes MRI-based dynamic models of the heart and the aorta, and a simplified dynamic model of the pulmonary vasculature. The small rectangles on the periphery of the thorax depict the EIT electrodes. TH: orange belt; TM: green belt; TL: gray belt; OB: black belt. TLM and THM not shown for easier visualization.

thorax model.

6.2.3 Analysis protocol

Analysis 1: Sources contributing to $\Delta\sigma$

The purpose of this analysis was to allow quantifying the contribution of each pulsatile source (ventricles, atria, lungs, aorta) to the EIT heart signal $\Delta\sigma$, in particular for two electrode belt placements commonly used in cardiac EIT, namely TM and OB (see Figure 6.1). For each belt, one heart cycle was simulated with all structures (atria, ventricles, lungs and aorta) contributing to the intra-thoracic impedance change. In each case, an image representing the RMS amplitude of the time signal at each pixel – hereafter referred to as RMS image – was calculated, as shown in Figure 6.2 (left). From this RMS image, the ventricular ROI (solid red line in the Figure) was automatically segmented in a similar fashion as the one described earlier in Section 5.2.4. Then, to investigate the individual influence of each source of impedance change (atria, ventricles, lungs, aorta), each structure was simulated independently, with the other structures frozen to their end-diastolic state. Again, in each case, an RMS image was calculated (such as Figure 6.2, right). From these RMS images, the contribution of each individual structure to the EIT heart signal was determined by summing up all pixels of the corresponding RMS image in the ventricular ROI. Evaluating the contribution of each individual structure in this manner involves that the superposition hypothesis is true, *i.e.* that simulating each individual structure (ventricles, atria, lungs, aorta) separately and computing the RMS

Chapter 6. Influence of belt position and displacement on the EIT-based measurement of CO

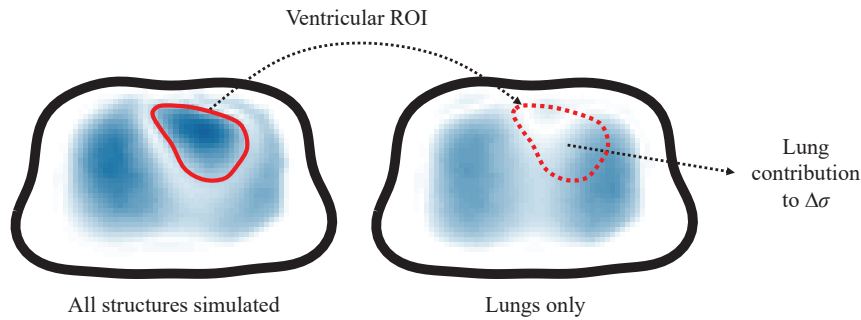


Figure 6.2 – Example of RMS images when simulating all structures (left) or the lungs only (right). The contribution of the lungs to the EIT heart signal $\Delta\sigma$ is determined by summing up all pixels of the lung RMS image falling into the ventricular ROI.

amplitude of the sum of their respective EIT image sequences, is similar to simulating all structures together and computing the RMS amplitude of the resulting sequence directly. This was verified to be true, with a relative absolute error of $3.2 \pm 1.7 \%$ (for TM) and $2.3 \pm 1.4 \%$ (for OB) between the RMS images of both cases in the ventricular ROI.

Analysis 2: Influence of belt displacement on EIT-based SV estimation

By deforming the heart model in a fashion similar to the one described in Section 5.2.2 in the previous chapter, 11 different SV values were simulated. The correlation between the peak-to-peak amplitude $\Delta\sigma_{\max}$ of the EIT heart signal and the simulated stroke volumes was then evaluated for all belt placements, in order to confirm/infirm the validity of $\Delta\sigma_{\max}$ as a correlate of SV.

In a second phase, the influence of belt displacement was investigated as follows. (1) $\Delta\sigma_{\max}$ as obtained using the TM belt placement was fitted (least-square linear fit) onto the reference simulated SV values, leading to a “baseline” $\Delta\sigma_{\max}$ -to-SV calibration. (2) Up-, down-, left-, and rightwards realistic electrode shifts were then applied to the TM belt, and $\Delta\sigma_{\max}$ was recalculated with these shifted belt configurations. (3) Finally, all calculated $\Delta\sigma_{\max}$ were converted to SV value using the previously obtained $\Delta\sigma_{\max}$ -to-SV calibration, and the error with respect to the reference simulated SV values was calculated in each case.

6.3 Results

This section presents the results of this study in a summarized form. A detailed description of the results can be found in [24] and [25].

6.3.1 Sources contributing to $\Delta\sigma$

In both belt placements, the main contributor to the EIT heart signal $\Delta\sigma$ was found to be the ventricles, by approximately 70 %, followed by the lungs (~ 15 %) and the atria (~ 10 %) [24]. The ventricular contribution was slightly stronger using the OB belt placement than with the TM placement.

6.3.2 Influence of belt displacement on EIT-based SV estimation

For all belt positions investigated, strong correlation coefficients ($r > 0.99$) were found between the peak-to-peak amplitude change $\Delta\sigma_{\max}$ and the simulated SV values, thereby corroborating the results obtained in Chapter 5 on the 2.5D model. However, significant errors (up to 30 mL) were found between the EIT-derived SV estimates and the simulated SV values after inducement of realistic belt displacements [25].

6.4 Discussion

The goals of this preliminary study were multiple. In a first step, a 4D bioimpedance model of the human thorax was created in order to investigate the influence of various belt positions. In this regard, the first finding of this study has shown that the EIT heart signal $\Delta\sigma$ is dominated by conductivity changes induced by ventricular activity, and that this contribution increases slightly when the belt is placed in an oblique plane. This can easily be explained by the larger ventricular “surface” imaged by an oblique EIT plane. However, contrary to observations in [171], a reduced contribution of the atria using the oblique belt placement instead of the transverse placement could not be observed. This needs to be explored further by comparing different reconstruction strategies and measurement settings.

This preliminary study has also allowed to corroborate the findings made earlier in Chapter 5, namely that tracking amplitude changes ($\Delta\sigma_{\max}$) in the EIT heart signal during breath-hold indeed allows tracking changes in SV. However, this ability to track SV changes seems to be significantly affected by belt displacements. These findings call into question the intra-subject repeatability of SV values obtained with the current setup. Future work should focus on finding an improved setup less sensitive to electrode displacements. A possible but limiting workaround could be to recalibrate the EIT signal using another modality after each displacement.

Pulmonary artery pressure by electrical impedance tomography **Part III**

7 Model-based feasibility study on the EIT-based measurement of PAP

Adapted from the post-print version of [136]:

Noninvasive pulmonary artery pressure monitoring by EIT: a model-based feasibility study

Martin Proença^{1,2}, Fabian Braun^{1,2}, Josep Solà¹, Jean-Philippe Thiran^{2,3}, and Mathieu Lemay¹

¹Systems Division, Centre Suisse d'Electronique et de Microtechnique (CSEM), Neuchâtel, Switzerland

²Signal Processing Laboratory (LTS5), Ecole Polytechnique Fédérale de Lausanne (EPFL), Lausanne, Switzerland

³Department of Radiology, University Hospital Center (CHUV) and University of Lausanne (UNIL), Lausanne, Switzerland

Accepted for publication in **Medical & Biological Engineering & Computing** Med. Biol. Eng. Comput., in press, 2016. DOI: 10.1007/s11517-016-1570-1

7.1 Introduction

7.1.1 Objectives

In Chapter 3, we have introduced the current limitations of PAP monitoring solutions in hemodynamically unstable patients and patients with chronic pulmonary hypertension (PH). The pulmonary artery catheter provides continuous readings but is associated with non-negligible morbidity and mortality rates, whereas transthoracic Doppler echocardiography is not conducive with continuous monitoring. The need for a safer solution for the clinical management of PH is thus strong. An optimal PAP monitoring modality should be non-invasive (free of any risks or complications, and thus compatible with frequent measurements) and unsupervised (able to operate without supervision of a medical doctor) [1].

In the present study, we propose and investigate the potential of a novel non-invasive, continuous and unsupervised PAP monitoring method based on the use of EIT.

7.1.2 Measurement principle

In Section 2.5, we have introduced the physiological relation linking blood pressure and the pulse wave velocity (PWV), the speed of propagation of pressure waves in the arterial tree. Monitoring changes in PAP using this relation implies measuring the PWV in the pulmonary arteries, and therefore to have access to the pulsatile signal of the pulmonary arteries. Hence the proposed use of EIT, as further detailed hereafter.

Let us consider the ejection of blood by the right ventricle starting with the opening of the pulmonary valve at time $t = 0$. The resulting pressure pulse propagates at a certain velocity (the PWV) to the various branches of the pulmonary arterial tree. At any downstream arterial site \mathbf{x} , the passage of the pressure pulse distends the arterial wall (Figure 7.1a) with a pressure $p(\mathbf{x}, t)$ (Figure 7.1b). The local distension of the arterial wall induced by $p(\mathbf{x}, t)$ induces a local variation in electrical conductivity $\sigma(\mathbf{x}, t)$ (Figure 7.1c). Consequently, assuming that $\sigma(\mathbf{x}, t)$ is entirely induced by $p(\mathbf{x}, t)$, they are inherently synchronous. Therefore $p(\mathbf{x}, t)$ and $\sigma(\mathbf{x}, t)$ are expected to have identical pulse transit times (PTT), *i.e.* the time required by the pressure pulse to reach location \mathbf{x} in the arterial tree (see dashed line in Figure 7.1b and 7.1c). The PTT being, by definition, inversely proportional to the PWV, we hypothesize that tracking changes in pulmonary PWV, and therefore in PAP, can be done by tracking changes in the PTT of $\sigma(\mathbf{x}, t)$ assessed by EIT:

$$\text{PAP} \nearrow \iff \text{PWV} \nearrow \iff \text{EIT-derived PTT} \searrow .$$

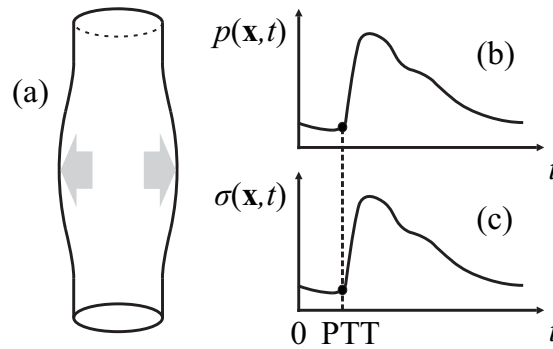


Figure 7.1 – Measurement principle of the pulmonary pulse transit time (PTT) by EIT. (a) At each cardiac cycle, the wall of each artery is distended by the passage of a pressure pulse. (b) The pressure exerted by blood at a given location \mathbf{x} along the arterial wall is described by $p(\mathbf{x}, t)$. (c) The local distension of the arterial wall induced by $p(\mathbf{x}, t)$ creates a small increase in electrical conductivity $\sigma(\mathbf{x}, t)$. Both waveforms ($p(\mathbf{x}, t)$ and $\sigma(\mathbf{x}, t)$) being inherently synchronous, their timing information – namely their PTT – is identical.

7.1.3 Previous work and study goal

The use of EIT for monitoring patients with PH has previously been proposed by the group of Smit *et al* [155]. They observed a decreased maximal pulmonary systolic impedance change (ΔZ_{sys}) in patients suffering from advanced stages of idiopathic pulmonary arterial hypertension. ΔZ_{sys} was hypothesized to represent pulmonary perfusion and its decrease to originate mostly from the reduction of the vascular bed. However, the physiological link between the *amplitude* information of the pulmonary impedance change and the PAP remains to this day unclear, as ΔZ_{sys} may not unequivocally be representative of perfusion [21, 52, 69]. Conversely, the *timing* information of the pulmonary impedance change has a direct physiological link to the PAP through the PWV, hence the PWV-based approach proposed in the present study.

We have previously demonstrated the feasibility of this EIT- and PWV-based approach experimentally for blood pressure monitoring in the systemic circulation [157, 159]. In the present study, we investigate its feasibility for the pulmonary circulation using simulations on a 4D bioimpedance model of the human thorax.

7.2 Methods

We test our approach using a model as this offers several advantages over clinical data: (1) we can easily simulate various PAP-affecting pathological conditions, in particular different types of PH, and thus avoid protocol- or pathology-specific results that could arise from clinical data; (2) we can freely induce PAP variations, be they small or

large; (3) we do not depend on reference hemodynamic variables measured in clinical settings, which can be difficult to obtain (*e.g.* pulmonary PWV) or affected by transient hemodynamics (*e.g.* PAP) [142].

Section 7.2.1 presents in detail the 4D bioimpedance model. Section 7.2.2 describes how the model can simulate various types of pulmonary hypertensive pathologies. Finally, the EIT simulations performed with the model and the signal processing approach for estimating a pulmonary PTT are detailed in Section 7.2.3.

7.2.1 Thoracic bioimpedance model

Main components and functionalities

We use a modified version of the 4D bioimpedance model presented in Chapter 6. This model, shown in Figure 7.2, consists in a mesh of a human thorax where each mesh element is at a fixed location \mathbf{x} and has a conductivity value $\sigma(\mathbf{x}, t)$ that varies over time, in function of the organ or anatomical structure occupying the location of the element at time t . The model includes conductivity changes induced by the main sources of cardiovascular activity in the thorax during breath-hold, namely the heart, the aorta and the pulmonary arterial tree. The geometrical deformations of the cardiac chambers and the aorta are directly based on 4D magnetic resonance imaging (MRI) scans of a healthy male volunteer (62 kg, 178 cm, 28 years old). The same could obviously not be done for the pulmonary arterial tree, due to the size of its microvasculature and the limited resolution of MRI scans, which is why a simplified model of the pulmonary vasculature was implemented in Chapter 6. In the present study, we replace this pulmonary model by a complete 4D bioimpedance model of a realistic pulmonary arterial tree.

To build this pulmonary model, we start by building an anatomically realistic static 3D model of the whole pulmonary arterial tree. Then, in order to dynamize it (*i.e.* to make it 4D by simulating the pressure-induced distension of its arteries over time), we use a circulatory model of the pulmonary circulation. Finally, we transform this 4D model into a 4D *bioimpedance* model by describing how the pressure-induced distension of the pulmonary arteries affects the conductivity $\sigma(\mathbf{x}, t)$ at each location \mathbf{x} in the lungs.

Anatomical model of the pulmonary arterial tree

This section describes the creation of the 3D anatomical model of the pulmonary arterial tree used in this work. The goal was to obtain a tree that is geometrically and morphometrically accurate. In other words, the tree should fill the lung cavities with realistic branching patterns, and the number and dimensions of all arterial segments in the tree should match those of actual human lungs. To that end, we will be using the study by Huang *et al* [74], which provides, for each order of arteries, their estimated

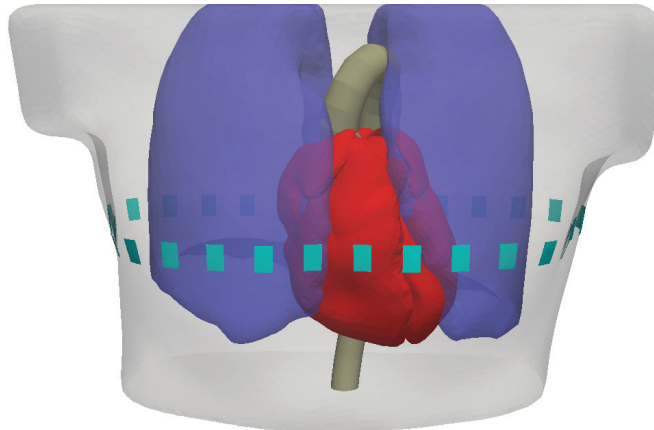


Figure 7.2 – 4D thoracic bioimpedance model. Each mesh element is at a fixed location and its conductivity $\sigma(\mathbf{x}, t)$ varies over the time course of the cardiac cycle, in function of the organ or anatomical structure occupying the location of the element at time t . The small rectangles on the periphery of the thorax depict the EIT electrodes.

number, average radius and length. They obtained these reference morphometrical data by measuring a pulmonary cast of a left pulmonary arterial tree. It is to be noted that the arterial radius measurements reported by Huang *et al* [74] were obtained in arteries at quasi-atmospheric pressure (*i.e.* zero pressure in medical applications, as blood pressure is standardly expressed in mmHg *above* atmospheric pressure). This is convenient in our case as our circulatory model (see the next section) needs to deal with zero-pressure radiuses.

As a first step in the tree creation process, an anatomically accurate model of the large pulmonary arteries by Reymond [141] – based on contrast-enhanced magnetic resonance angiography scans – was rigidly registered onto our corresponding MRI-based arteries. These arteries were imaged *in vivo* and were thus subjected to a distending PAP > 0 . Thus we scaled down their radiuses in order to fit the reference zero-pressure arterial radiuses reported by Huang *et al* [74].

As a second step, the remaining (medium and small) arteries were generated using the volume-filling branching algorithm by Burrowes *et al* [28] described in detail in the Appendix (Section A.1): the lung volumes were automatically filled with a branching tree using the end segments of the large arteries as seed points for the tree growing procedure.

In the whole tree, the ratio between the radius of each artery and those of its two daughters was controlled using equation (A.3), which depends on the branching (ζ) and asymmetry (γ) ratios. The branching ratio was set to the average value $\zeta = 3.2$ for pulmonary arterial trees in humans [74]. The asymmetry ratio γ was then adjusted in order for the generated tree to accurately match the morphometrics reported by

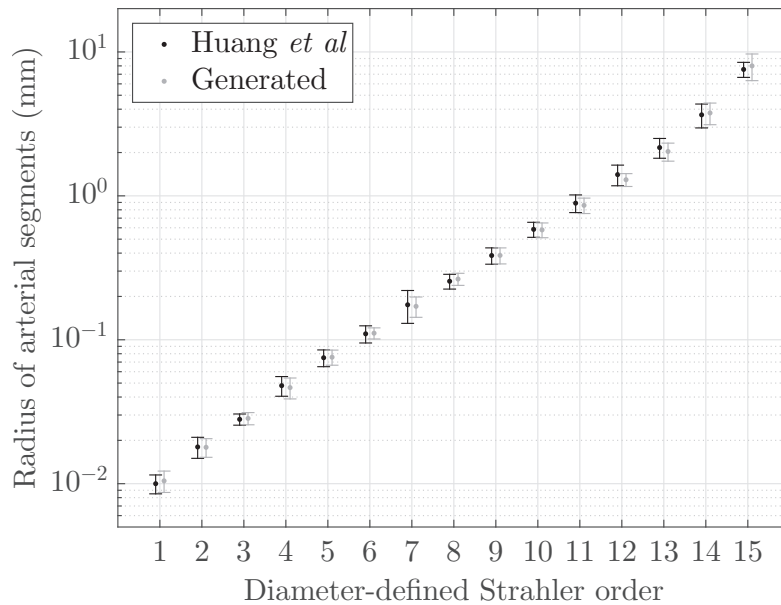


Figure 7.3 – Radius of all generated arterial segments in the left pulmonary tree as a function of their order: comparison with reference morphometrical values of an actual left pulmonary arterial tree (Huang *et al* [74]). The values are given as mean \pm SD.

Huang *et al* [74], as illustrated in Figures 7.3, 7.4 and 7.5, which respectively show the radius, length and number of arterial segments in the generated left arterial tree against reference morphometrical values. In the figures, the arterial segments are sorted according to their *order*, as is usual for tree-like structures: we use the so-called diameter-defined Strahler ordering system as it is the system used by Huang *et al* [74]. The final generated 3D pulmonary arterial tree is shown in Figure 7.6.

Circulatory model of the pulmonary arterial tree

The purpose of the circulatory model is to determine the pressure-induced distension undergone by each arterial segment in the pulmonary arterial tree during the cardiac cycle. We describe in detail the inner workings and principles of so-called *1D distributed parameter models* in the Appendix (Section A.2). In short, these models consider the arterial tree as a vast network of interconnected arterial segments through which pressure and flow waves propagate. By analogy with electrical circuits, transmission line theory can be applied and provides analytical solutions for pressure and flow. However, this analogy is only truly valid in the smaller arterial segments, which do not taper (narrow along their length) significantly. In the larger (tapering) segments of the arterial tree, non-linear effects prevent the use of transmission line theory and numerical solutions are required to assess pressure and flow. Therefore two models are necessary for obtaining the distribution of pressure and flow in the pulmonary arterial tree: a non-linear and numerically-solved model for the large arteries, and a linear and analytically-solved

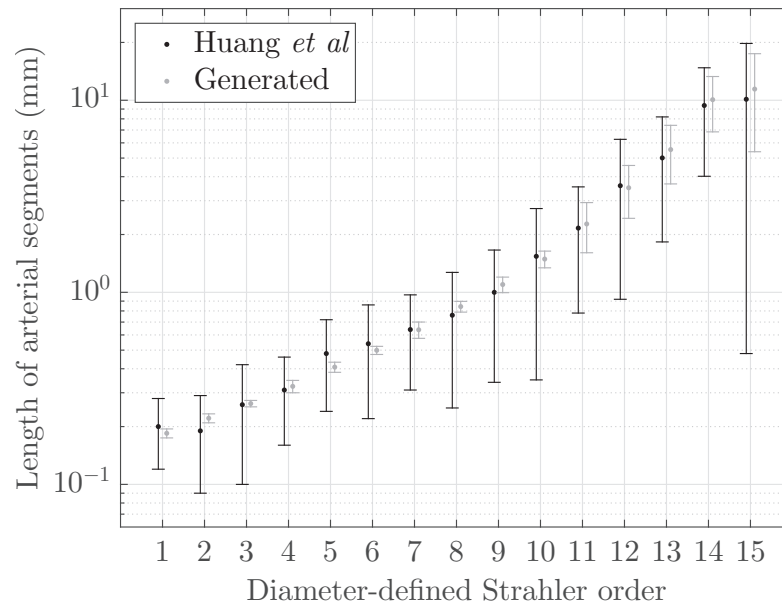


Figure 7.4 – Length of all generated arterial segments in the left pulmonary tree as a function of their order: comparison with reference morphometrical values of an actual left pulmonary arterial tree (Huang *et al* [74]). The values are given as mean \pm SD.

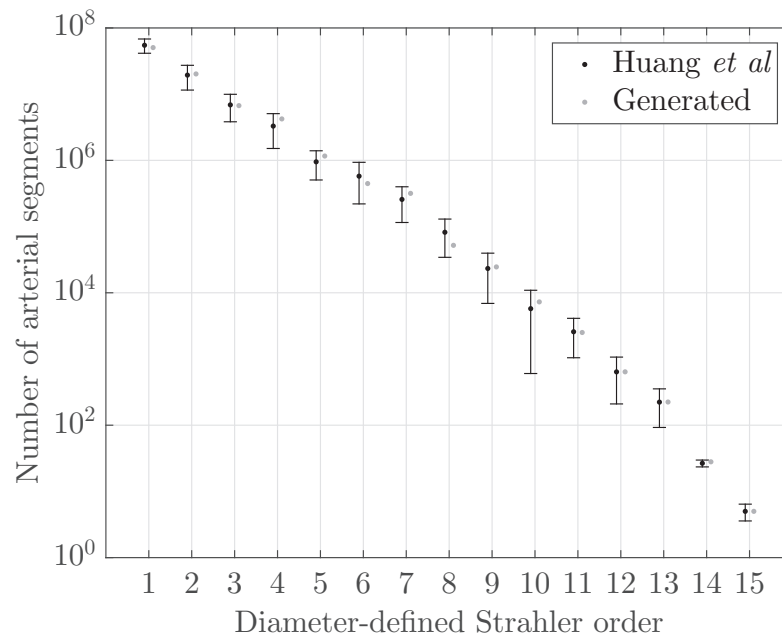


Figure 7.5 – Number of generated arterial segments in the left pulmonary tree as a function of their order: comparison with reference morphometrical values of an actual left pulmonary arterial tree (Huang *et al* [74]). The values of the reference are given as mean \pm SD.

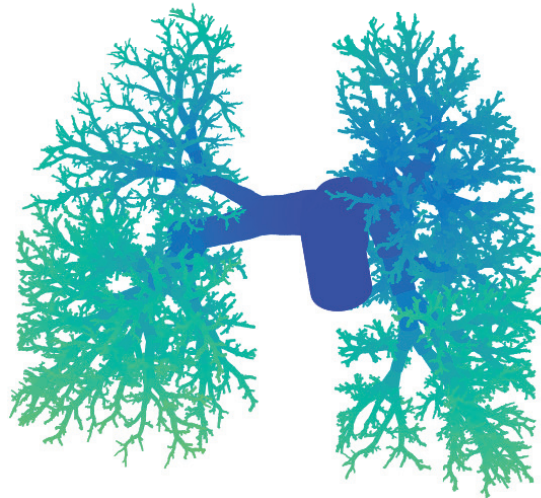


Figure 7.6 – Anatomical model of the pulmonary arterial tree. To help the visualization, not all smaller arteries are shown and a color code is used to illustrate the distance from the pulmonary valve (dark blue = close; light green = far).

model for the small arteries. In order to solve both of these models, proper boundary conditions must be defined. In particular, each model requires:

- a) An *inflow* boundary condition: most often, a flow waveform is used. Alternatively, a pressure waveform or model of the right ventricle (varying elastance model) can be used [141], but only one of those or the system will be overdetermined;
- b) An *outflow* boundary condition: most often, an output impedance is used, by analogy with transmission line theory [123]. The impedance mimics the load “seen” beyond the arterial tree (or portion of the tree) under consideration.

Figure 7.7 illustrates the structure of the global circulatory model of the pulmonary circulation. In the present study, the so-called *transition sites* are the arterial sites in the tree where the transition between the large and the small arteries occurs, *i.e.* the sites where the transition between the non-linear and the linear model will take place. In the present study, the 1D distributed parameter model by Reymond [141], adapted by Billiet [17] for the pulmonary circulation, will be used as non-linear model for the large arteries, whereas the standard linear solutions based on transmission line theory will be implemented for the smaller arteries. As mentioned above, both models are described in detail in the Appendix (Section A.2).

Determination of the transition sites. The *transition sites* are those segments in the arterial tree where the transition between the so-called “large” and “small” arteries occurs. From a hemodynamic viewpoint, large arteries are dominated by inertial effects,

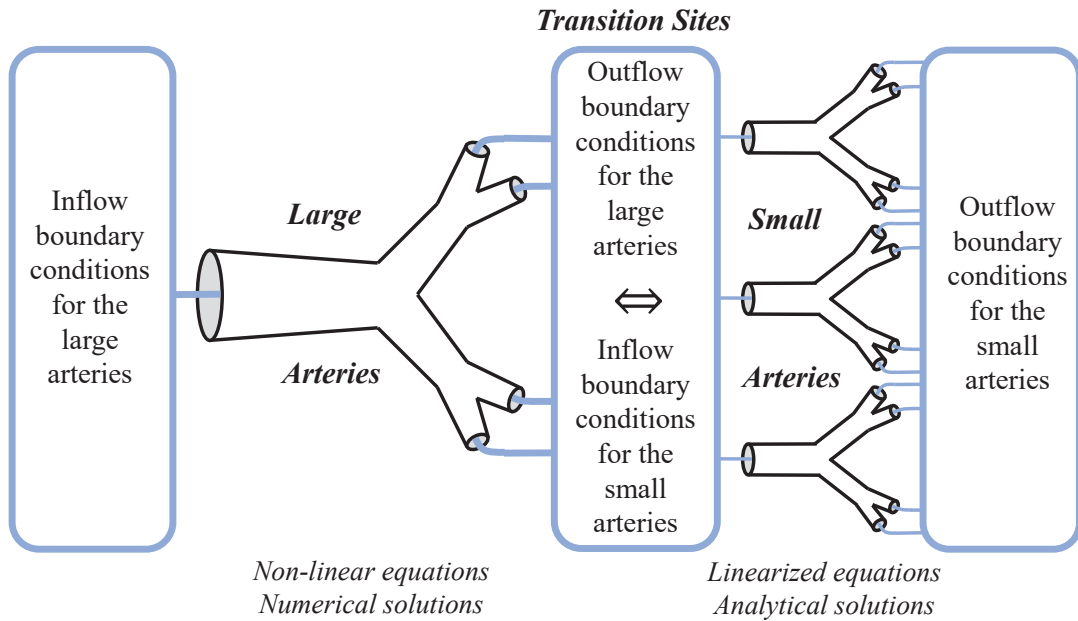


Figure 7.7 – Structure of the global circulatory model of the pulmonary circulation. A non-linear and numerically-solved model is used for the large arteries, and a linear and analytically-solved model is used for the small arteries. The transition between the so-called “large” and “small” arteries occurs at the *transition sites*. Each model requires proper boundary conditions to be solved. At the level of the *transition sites*, the outflow boundary conditions for the large artery model need to be consistent with the inflow boundary conditions for the small artery model, for continuity purposes.

whereas small arteries are dominated by viscous effects [180]. Therefore, as a dimensionless ratio of inertial over viscous forces, the so-called Womersley number α is a well-suited criterion for classifying arteries either as large or small [180]. Milnor [115] measured Womersley numbers at multiple arterial sites and found that large elastic arteries typically show Womersley numbers $\alpha \geq 4$. Therefore, we can define our *transition sites* as the last arterial segments in the tree (starting from the heart) for which $\alpha \geq 4$. Furthermore, as the linear circulatory model will be used beyond these sites, we can verify that the linearization condition is met for the small arteries, *i.e.* that the non-linear convective acceleration term in the x -momentum Navier-Stokes equation (equation (A.6) in Section A.2) becomes negligible [154]. This is the case if $U/PWV \ll 1$, where U is the characteristic velocity (average axial velocity) of blood [35, 167]. Even in the worst-case scenario (highest flow, lowest PWV), we found U/PWV to be systematically < 0.04 in the small arteries, which satisfies the linearization condition.

Boundary conditions. We define hereafter the inflow and outflow boundary conditions for both the large and small artery circulatory models. At the level of the *transition sites*, the outflow boundary conditions for the large artery model need to be consistent with the inflow boundary conditions for the small artery model, for continuity purposes.

Chapter 7. Model-based feasibility study on the EIT-based measurement of PAP

As inflow boundary condition for Reymond's large artery model, we use the waveform proposed by [124], which can easily be scaled to any desired cardiac output (CO) and heart rate:

$$q(0, t) = \frac{\text{CO} \cdot t}{\tau_p^2} \exp\left(-\frac{t^2}{2\tau_p^2}\right), \quad (7.1)$$

with $t \in [0, T]$, where T is the cardiac period, and τ_p is the time to peak flow (also known as acceleration time). This time is inversely related to the PAP and can be empirically derived from it as [85]:

$$\tau_p = \frac{1}{6.8} [2.1 - \log_{10}(P_A)], \quad (7.2)$$

where P_A is the mean PAP.

As outflow boundary condition, Reymond's model uses 3-element Windkessel models (Section A.2.1) at all *transition sites* [141]. These models are frequently used to mimic the afterload of the heart [179]. In Reymond's model, they are used to mimic the equivalent impedance of the tree branches "seen" from each *transition site* downstream. These equivalent impedances are known in our study from the 3D anatomical model of the pulmonary arterial tree. With both its inflow and outflow conditions thus defined, Reymond's model can now be solved.

Solving Reymond's model provides us directly with the inflow boundary conditions for the small arteries, as it determines the flow waveforms entering each *transition site*, *i.e.* entering the small arteries. On the other hand, the outflow boundary conditions for the small arteries in linearized circulatory models are typically set by controlling the value of the pressure downstream of the arterial tree [123] (let us call it P_W). Formally speaking, P_W represents the pressure of the capillaries or the venous microvasculature, which is difficult to measure in clinical practice. It is however essentially the same as pulmonary capillary wedge pressure if we neglect the small transvenous pressure gradient [109], and is assumed to be continuous in the model; we discuss the validity of this assumption in Section 7.4.

Setting P_W to a given desired value in structured tree models is typically done through the use of N_t terminal impedances Z_{t_i} ($i \in \{1, \dots, N_t\}$) at the leaves of the tree [123] (see Figure 7.8). The value of each terminal impedance Z_{t_i} must be properly set in order to ensure its upstream pressure to equal P_W . This requires finding the flow q_i running through each i -th leaf of the tree, as $Z_{t_i} = P_W / q_i$, $\forall i \in \{1, \dots, N_t\}$. These flow values can easily be obtained by momentarily setting $Z_{t_i} = 0$ for all terminal impedances and imposing the desired transarterial pressure gradient ($P_A - P_W$) at the input of the tree. With both its inflow and outflow conditions now defined, the linear model for the small arteries can be solved as well.

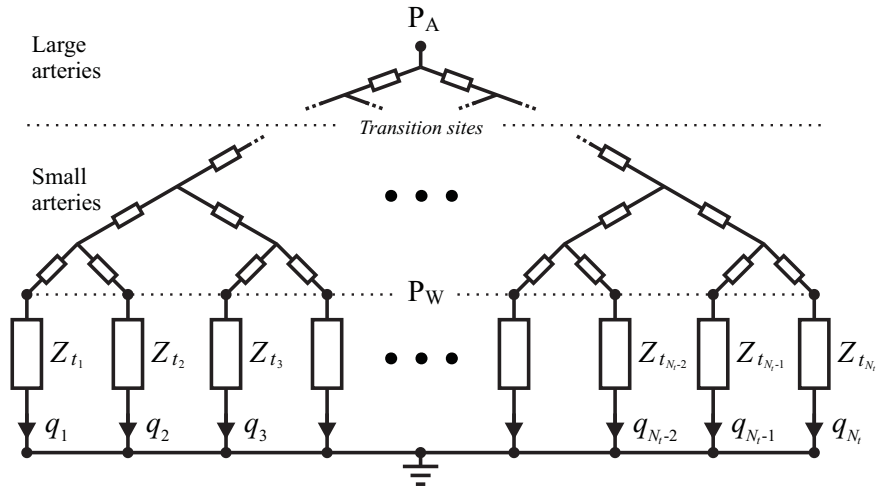


Figure 7.8 – Schematic representation of the pulmonary arterial tree, by analogy with electrical circuits. The tree is made of large and small arteries. In the large arteries, non-linear effects are non-negligible and the distribution of pressure and flow in the arterial network requires a numerical solution. From the so-called *transition sites* and beyond, the distribution of pressure and flow in the arterial network can be solved analytically after linearization of the problem. Each terminal arterial segment in the tree (pre-capillary artery) is connected to a terminal impedance Z_{t_i} that allows controlling the value of the pressure P_W at the output of the tree.

In this section, we have presented an anatomically realistic static 3D model of the whole pulmonary arterial tree (Figure 7.6). We have then made it 4D by assessing the pressure-induced distension of all pulmonary arteries over time via a circulatory model. As a last step, we need to transform this 4D model into a 4D *bioimpedance* model by describing how the pressure-induced distension of each artery at location \mathbf{x} in the lungs induces changes in pulmonary conductivity $\sigma(\mathbf{x}, t)$.

Assessment of pulmonary conductivity

During breath hold, the effective conductivity of lung parenchyma $\sigma(\mathbf{x}, t)$ is predominantly affected by arterial pulsatility. The distension of the arterial bed makes the conductivity of lung parenchyma slightly rise above its end-diastolic value $\sigma(\mathbf{x}, 0)$ during systole (*i.e.* for $t > 0$), due to the high conductivity of blood ($\sigma_{blood} \approx 0.7$ S/m at EIT frequencies) [68]. This end-diastolic value of lung parenchyma $\sigma(\mathbf{x}, 0)$ is difficult to estimate as it depends on the conductivity of lung alveolar tissue σ_{alv} , which depends on the fractional volume of air in the lungs. Several mathematical models have been developed to express σ_{alv} as a function of the degree of deflation of the lungs. Roth *et al* [145] compared several of these models and introduced their own, based on 3D alveolar microstructures. For lung tissue imaged at functional lung capacity as is the case in our model, their observations suggest an average value $\sigma_{alv} = 0.1$ S/m [145].

This conductivity value does not include extra-capillary blood vessels, *i.e.* the arteries and veins. In order to obtain the effective conductivity of the whole lung parenchyma $\sigma(\mathbf{x}, t)$ (including extra-capillary blood vessels), Nopp *et al* [122] suggested to consider lung tissue as a mixture of a dielectric medium (alveolar tissue with conductivity σ_{alv}) and conductive inclusions (extra-capillary blood vessels with conductivity σ_{blood}). The Maxwell Garnett mixing rule states that [87]:

$$\sigma(\mathbf{x}, t) = \sigma_m + \frac{\frac{1}{3}f_i(\sigma_i - \sigma_m) \sum_{k=1}^3 \frac{\sigma_m}{\sigma_m + N_k(\sigma_i - \sigma_m)}}{1 - \frac{1}{3}f_i(\sigma_i - \sigma_m) \sum_{k=1}^3 \frac{N_k}{\sigma_m + N_k(\sigma_i - \sigma_m)}}, \quad (7.3)$$

where $\sigma_m = \sigma_{alv}$ and $\sigma_i = \sigma_{blood}$ are the conductivities of the dielectric medium and the inclusions respectively, $f_i = f_i(\mathbf{x}, t)$ is the volume fraction of the inclusions, N_k are the depolarization factors and $k \in \{1, 2, 3\}$ corresponds to the three Cartesian coordinates. For cylindrical inclusions such as arterial segments, $N_{1,2} \approx 0.5$ and $N_3 \approx 0$ [87]. By means of our anatomical model of the pulmonary arterial tree, the volume fraction of blood vessels $f_i(\mathbf{x}, t)$ can be assessed in each pulmonary voxel \mathbf{x} over time, as illustrated in Figure 7.9, with pulmonary venous blood volume approximately equal to the non-pulsatile (end-diastolic) component of arterial blood volume [65]. For instance, in a small pulmonary voxel at location \mathbf{x} whose volume is occupied at 10 % by arteries at end diastole ($t = 0$), the volume fraction of blood will be $f_i(\mathbf{x}, 0) = 0.2$ (10 % of arterial blood and 10 % of venous blood). The remaining 80 % will be occupied by lung alveolar tissue with conductivity σ_{alv} . Using (7.3), this gives us $\sigma(\mathbf{x}, 0) = 0.17$ S/m in that particular pulmonary voxel.

As the cardiac cycle unfolds ($t > 0$) and systole occurs, the arteries distend with the increase in pressure. We can precisely determine the extent of this arterial distension thanks to the circulatory model. With this distension, the increase in arterial blood volume and therefore $f_i(\mathbf{x}, t)$ is known at each instant of the cardiac cycle. As a consequence, via (7.3), the value of $\sigma(\mathbf{x}, t)$ is also known for every location \mathbf{x} in the lungs and for the whole cardiac cycle, which completes the creation of our 4D *bioimpedance* model.

7.2.2 Simulation of pathologies

The hemodynamic behavior of our 4D thoracic bioimpedance model is controlled by a set of hemodynamic parameters (P_A , P_W , CI , R_t , and C_t). In the following we describe each these parameters, their physiological interdependencies, and their typical values in normotensive (nonpathological) conditions. We will then detail how the values of these parameters can be adjusted to simulate several pulmonary hypertensive pathologies.

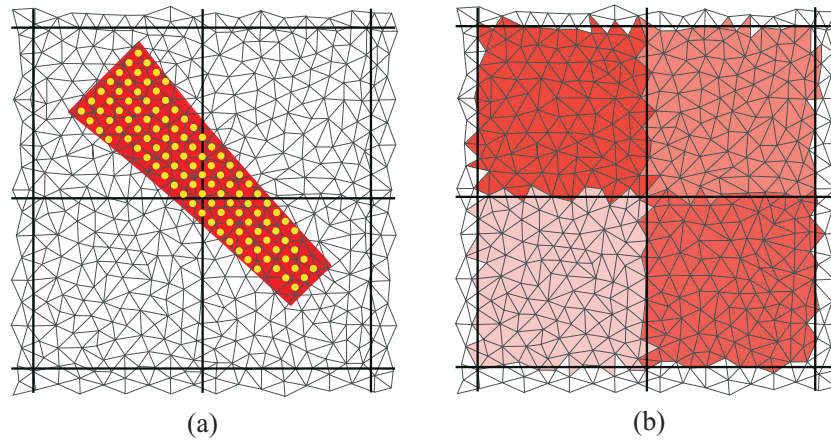


Figure 7.9 – Assessment of the volume fraction of extra-capillary blood vessels in each pulmonary voxel. Lung tissue can be considered as a mixture of a dielectric medium (alveolar tissue) and conductive inclusions (extra-capillary blood vessels) [122]. The pulmonary voxels should not be chosen too large in order not to exceed EIT resolution. They should not be too small neither in order for most inclusions (arteries and veins) to be of reasonably small size with respect to the voxels for the Maxwell Garnett mixing rule (equation 7.3) to be applicable [87]. We consider 1 mL cubic voxels to be a good compromise. The computation of the volume fraction $f_i(\mathbf{x}, t)$ of conductive inclusions for each voxel at location \mathbf{x} and at time t is performed as follows. Consider the 2D example shown in (a). An arterial segment passes through four cubic voxels. In order to assess the percentage of the segment's volume in each voxel, the segment is filled with a grid of uniformly spaced points, with a grid resolution equal to one fourth of the segment's average radius. A voxel containing 30 % of all grid points will be assigned 30 % of the segment's volume. Note that this point-to-cube assignment procedure is largely sped up (in terms of computational time) by the choice of cubic voxels (instead of tetrahedral voxels, for instance). After this procedure is performed for all arterial segments of the pulmonary tree, the volume fraction $f_i(\mathbf{x}, t)$ for each voxel is known and is assigned to all tetrahedral elements of the mesh whose barycenters falls within said voxel, as shown in (b).

Hemodynamic parameters description, interdependencies and normal values

We have earlier described in Section 2.3.2 a remarkable hemodynamic characteristic of the pulmonary circulation, namely that the pulmonary RC time τ_{RC} , *i.e.* the product of the pulmonary vascular resistance R_t and compliance C_t , is a constant (at a given downstream left atrial pressure) [164]. In a retrospective study on large clinical datasets, Tedford *et al* [164] derived the following relationship with pulmonary capillary wedge pressure (P_W), a surrogate measure of left atrial pressure:

$$\tau_{RC} = -0.0063 \cdot P_W + 0.46. \quad (7.4)$$

As a consequence, except for particular conditions affecting left atrial pressure and thus

Chapter 7. Model-based feasibility study on the EIT-based measurement of PAP

P_W , the pulmonary RC time τ_{RC} remains constant in health and hypertension [93, 94, 149]. Although τ_{RC} is related to HR [94, 149], any reduction in R_t and related increase in C_t during hypertension treatment has been shown not to be due to a change in HR, and therefore the latter is constant in the model (HR = 80 bpm) [94].

In their literature review on pulmonary hemodynamics in normal subjects, Kovacs *et al* [88] reported normal values for R_t of 0.056 ± 0.023 mmHg·s/mL. In our model, R_t can directly be obtained from the anatomical model of the pulmonary arteries as the equivalent resistance of the entire tree [180]. We obtain $R_t = 0.048$ mmHg·s/mL, which is well in line with the aforementioned value reported by Kovacs *et al* [88]. They also reported normal mean PAP ($P_A = 14.0$ mmHg) and pulmonary capillary wedge pressure ($P_W = 8.0$ mmHg) values, which yields $\tau_{RC} = 0.41$ s via (7.4). We can then obtain the pulmonary vascular compliance C_t using the definition of the pulmonary RC time:

$$C_t = \tau_{RC}/R_t, \quad (7.5)$$

which gives us $C_t = 8.478$ mL/mmHg. Lastly, we can find the cardiac index (CI), *i.e.* the cardiac output (CO) normalized by the body surface area (BSA):

$$CI = \frac{CO}{BSA} = \frac{P_A - P_W}{R_t \cdot BSA}. \quad (7.6)$$

With $BSA = 1.78$ m² calculated using the Du Bois formula [42], we find $CI = 4.19$ L/min/m², which is well in line with the value of 4.10 L/min/m² reported by Kovacs *et al* [88].

These normal (nonpathological) values for the hemodynamic parameters governing the model are summarized in the first row of Table 7.1.

Simulation of pulmonary hypertensive conditions

By modifying the values of the hemodynamic parameters controlling the model, several hypertensive conditions can be realistically simulated and allow us to test our PAP monitoring method in various forms of PH.

We have previously described the clinical classification of PH into five groups (Section 2.4.2): pulmonary arterial hypertension (PAH), PH due to left heart disease (PH-LHD), PH due to lung diseases and/or hypoxia, chronic thromboembolic PH (CTEPH), and PH with unclear and/or multifactorial mechanisms [56]. We aim at simulating one pathological case of each group, except for the last one, since its pathogenesis is unclear. For each pathological case considered, 5 levels of PAP above the nonpathological value (14 mmHg) will be considered, by increments of 10 mmHg (*i.e.* $P_A = \{24, 34, 44, 54, 64\}$ mmHg). The case $P_A = 24$ mmHg simulates a borderline

Table 7.1 – Normal and pathology-specific values of the hemodynamic parameters of the model.

Pathology	P_A (mmHg)	P_W (mmHg)	CI (L/min/m ²)	R_t (mmHg·s/mL)	C_t (mL/mmHg)
None	14.0	8.0	4.19	0.048	8.478
PAH	24.0	8.0	2.82	0.191	2.141
	34.0	8.0	2.63	0.334	1.225
	44.0	8.0	2.55	0.477	0.858
	54.0	8.0	2.50	0.620	0.660
	64.0	8.0	2.48	0.764	0.536
PH-LHD	24.0	15.3	2.66	0.111	3.284
	34.0	22.6	2.23	0.173	1.835
	44.0	29.9	2.02	0.236	1.154
	54.0	37.2	1.91	0.298	0.758
	64.0	44.5	1.83	0.360	0.499
HAPE	24.0	12.0 ^a	3.70	0.110 ^b	3.107
	34.0	17.0 ^a	3.70	0.155 ^b	1.813
	44.0	22.0 ^a	3.70	0.201 ^b	1.280
	54.0	27.0 ^a	3.70	0.246 ^b	0.989
	64.0	32.0 ^a	3.70	0.292 ^b	0.806
CTEPH	24.0	8.0	2.51	0.215	1.905
	34.0	8.0	2.30	0.382	1.073
	44.0	8.0	2.22	0.549	0.747
	54.0	8.0	2.17	0.715	0.573
	64.0	8.0	2.14	0.882	0.464

PAH: pulmonary arterial hypertension; PH-LHD: pulmonary hypertension due to left heart disease; HAPE: high altitude pulmonary edema; CTEPH: chronic thromboembolic pulmonary hypertension; P_A : mean pulmonary artery pressure; P_W : mean pulmonary capillary wedge pressure; CI: cardiac index; R_t : pulmonary vascular resistance; C_t : pulmonary vascular compliance.

^a These values actually represent capillary pressure P_C , not pulmonary capillary wedge pressure P_W . As detailed in the text, P_W in HAPE is actually normal (10.0 mmHg) [101], whereas P_C is abnormally elevated. Increasing P_W in the model can either simulate an increase in P_W (as is the case in PH-LHD) or an increase in transvenous pressure gradient (as is the case in HAPE).

^b As the values provided for P_W actually represent P_C (see previous note), these R_t values actually represent pulmonary arterial resistance only, not the true values of the entire pulmonary vascular resistance. Those can be obtained using (7.6) with $P_W = 10.0$ mmHg for all levels of HAPE [101].

Chapter 7. Model-based feasibility study on the EIT-based measurement of PAP

pre-hypertensive stage, as PH is only formally diagnosed for $P_A \geq 25$ mmHg [56]. The remaining cases (34 to 64 mmHg) represent mild to severe levels of PAP.

Pulmonary arterial hypertension (PAH). PAH is characterized by the vasoconstriction, muscularization and fibrosis of the small pulmonary arteries (< 0.5 mm of diameter) [56]. The loss of distensibility that results from this vascular remodeling process progressively induces an overall decrease in arterial compliance in the whole tree [96, 148]. In our model, PAH is simulated by reducing the diameter of the small arteries. This allows us to increase R_t to any targeted value for simulating the various levels of PAH. The remaining parameters are then adjusted accordingly, as detailed hereafter.

Let us first consider the average hemodynamic parameter values in PAH reported by Humbert *et al* [75] from a French national registry: $P_A = 55.0$ mmHg, $P_W = 8.0$ mmHg (unaffected in PAH) and $CI = 2.5$ L/min/m². We find the corresponding R_t value (0.635 mmHg·s/mL) with (7.6). With the baseline P_A (14.0 mmHg) and R_t (0.048 mmHg·s/mL) values found earlier for the normal (nonpathological) case, we now have two $\{P_A, R_t\}$ pairs, which allows us to predict R_t as a function of P_A , as both quantities are linearly related in the pulmonary circulation [149]. We obtain:

$$R_t = 0.0143 \cdot P_A - 0.1519. \quad (7.7)$$

Finally, for each level of PAP, we obtain C_t via (7.5), and CI via (7.6).

The complete list of thus-obtained hemodynamic parameter values to simulate each level of PAH is provided in Table 7.1.

PH due to left heart disease (PH-LHD). In the second group of pulmonary PH, the failure of the left heart to pump blood efficiently – as in cases of valvular diseases or advanced stages of heart failure – leads to an elevation of left heart pressures [64]. This rise in P_W causes an elevation of P_A upstream [56]. R_t can remain normal, or significantly increase in cases of capillary and arterial remodeling [64]. In a retrospective study in heart failure patients, Afshar *et al* [9] reported the following average hemodynamic parameters: $P_A = 38.0$ mmHg, $P_W = 25.5$ mmHg and $CI = 2.13$ L/min/m². From these values and the baseline P_A and P_W values found for the above-described nonpathological case, we can predict P_W for all levels of PAP, as experimental data show a quasi-linear relationship between P_A and P_W in PH-LHD [9]:

$$P_W = 0.73 \cdot P_A - 2.21. \quad (7.8)$$

Proceeding as for PAH, we then find R_t , C_t and CI for all levels of PAP. The complete list of thus-obtained hemodynamic parameter values to simulate each level of PH-LHD is provided in Table 7.1.

PH due to lung diseases and/or hypoxia. One example of the third PH group is the high altitude pulmonary edema (HAPE), a potentially lethal condition affecting previously healthy individuals rapidly going to high altitude [178]. The exact cause of HAPE remains unknown [101]. The favored hypothesis regarding its genesis is a severe and inhomogeneous vasoconstriction of the vasculature associated with a stress failure and an increase in transmural pressure P_C of the capillaries [178]. Rupture of the capillary wall causes fluid to flow from the capillary lumen to the interstitial and alveolar spaces. In order to simulate HAPE in our model, we start by randomly designating small regions of the lungs as edemic while the others remain unaffected, thus mimicking the typically patchy distribution of high altitude-induced edemas [178]. Vasoconstriction is induced in the non-edemic regions only [178], thus increasing R_t and decreasing C_t via (7.5). In the edemic regions, the presence of fluid in the alveolar space causes the electrical conductivity of the parenchyma to increase. We consider an increase in lung water concentration by 75 % [152]. In the aforementioned model proposed by Roth *et al* [145] for estimating the conductivity of lung parenchyma, this corresponds to using an alveolar tissue conductivity $\sigma_{alv} = 0.15$ S/m.

In a study on control and HAPE-susceptible subjects at high altitude, Maggiorini *et al* [101] concluded that HAPE is initially caused by an increase in P_C . It stems from their study that $P_A \approx 2 \cdot P_C$. The remaining hemodynamic variables of the model, namely P_W and CI, remain normal in case of HAPE [178]. Maggiorini *et al* [101] reported values of $P_W = 10.0$ mmHg and $CI = 3.7$ L/min/m² for both control and HAPE-susceptible subjects at high altitude [101]. In our model, the abnormal increase in P_C can be simulated simply by setting $P_W = P_C$. Indeed, increasing P_W in the model can either simulate an increase in left atrial pressure (as is the case in PH-LHD) or an increase in transvenous pressure gradient (as is the case in HAPE).

The complete list of thus-obtained hemodynamic parameter values to simulate each level of HAPE is provided in Table 7.1.

Chronic thromboembolic pulmonary hypertension (CTEPH). In the fourth group of PH, the disease is characterized by the partial or complete obliteration of one or several pulmonary arterial segments [128]. As a consequence, a part or the entirety of the flow is redirected towards the nonoccluded areas, thereby exposing them to higher wall shear stresses [72]. An arteriopathy similar to that encountered in PAH (vasoconstriction and vascular remodeling) progressively develops in these segments, while the arteries downstream of the occluded areas typically remain unaffected [72, 128].

In the model we simulate this disease by occluding one of the daughter vessels of the left interlobar artery and by inducing vasoconstriction in those parts of the microvasculature that are not downstream of the occluded segment [72]. Pepke-Zaba *et al* [128] reported average hemodynamic parameters in CTEPH from an international registry: $P_A = 47.0$ mmHg and $CI = 2.2$ L/min/m². Left atrial pressure remains unaffected in CTEPH;

Nagaya *et al* [118] reported a value of 8.0 mmHg for P_W . Following the same procedure as the one used for PAH, we then find R_t , C_t and CI for all levels of PAP.

The complete list of thus-obtained hemodynamic parameter values to simulate each level of CTEPH is provided in Table 7.1.

7.2.3 EIT simulations and PTT estimation

With the ability to simulate various PAP-affecting pathologies in our 4D bioimpedance model, we can now proceed to simulating EIT measurements using the model. All EIT simulations were performed with Matlab (MathWorks, Natick, USA) using the framework of the EIDORS toolbox [4].

EIT simulations

Obtaining surface voltage measurements (the forward problem). The cardiac cycle, of duration $T = 0.75$ s, was discretized into 25 time instants of 30 ms each, thus corresponding to an EIT image sampling rate of 33 frames/sec. At each k -th time instant of the cardiac cycle, the first-order forward solver of EIDORS was used to simulate the propagation of small alternating electrical currents in the bioimpedance model (via the electrode belt shown in Figure 7.2) and measure the resulting voltages \mathbf{v}_k . A voltage matrix \mathbf{V} was then obtained by concatenating horizontally all 25 column vectors \mathbf{v}_k .

Real EIT measurements are well-known to include noise. In order to model noisy voltages, a realistic SNR was considered. In [151], the authors analyzed recordings from a Goe MF II EIT device (CareFusion, Germany) and found SNRs ranging from 42 to 156 dB. We chose a worst-case scenario SNR of 42 dB (*i.e.* SNR = 15,850). Following their approach, noisy voltages \mathbf{V}_n were thus obtained by adding a white Gaussian noise of variance \mathcal{P}_i/SNR to each i -th line of \mathbf{V} , where \mathcal{P}_i is the average power of the i -th line [151].

So-called *difference* voltages \mathbf{U}_n were then obtained by subtracting the first column (first frame) of \mathbf{V}_n , *i.e.* the end-diastolic voltages, from all columns (all frames) of \mathbf{V}_n , as is usual in medical EIT applications [73]. \mathbf{U}_n thus describes voltage variations around a reference state (end diastole) and allows the linearization of the EIT reconstruction problem for small voltage variations around this working point.

Reconstructing the internal conductivity distribution (the inverse problem). Image reconstruction was carried out on a coarser version of the thoracic mesh using the widely-used one-step Gauss-Newton algorithm with the Laplace prior [100]. *Difference* noisy EIT images \mathbf{Y}_n representing the intra-thoracic conductivity changes over time with

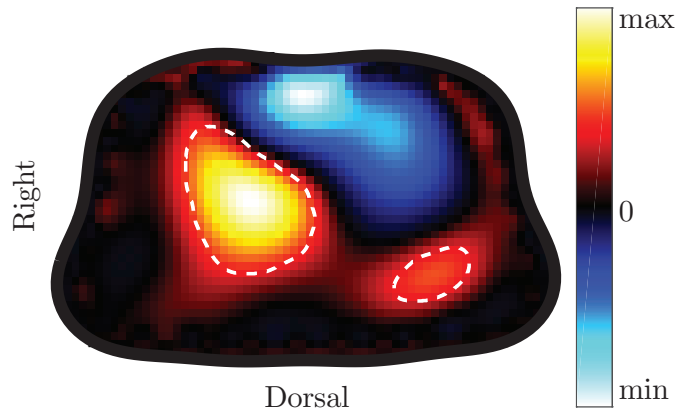


Figure 7.10 – Example of reconstructed EIT frame (slice at the level of the EIT electrodes shown in Figure 7.2) depicting the end-systolic distribution of conductivity change (with respect to end diastole). Cool colors (heart region) depict conductivity decreases with respect to end diastole, while warm colors (lung regions) depict conductivity increases. The pulmonary region of interest is highlighted by dashed lines. EIT tomographs provide *functional* information; they are known for not being anatomically accurate references. A lack of symmetry between the left and right lungs – as is the case here – is not unusual.

respect to the end-diastolic reference state were thus obtained as:

$$\mathbf{Y}_n = \mathbf{R}\mathbf{U}_n, \quad (7.9)$$

where \mathbf{R} is the so-called reconstruction matrix. Figure 7.10 shows an example of an EIT frame at end systole.

Pulmonary PTT estimation approach

In the following, the automatic procedure for estimating a pulmonary PTT value from a 25-frame EIT image sequence \mathbf{Y}_n is described.

First, a pulmonary region of interest (ROI), defined as those pixels depicting a lung-like behavior and a significant pulsatility, was automatically segmented from the EIT images. To do so, the cardiac frequency Fourier coefficient z_T of the EIT time signal $s(t)$ at each pixel was computed as:

$$z_T = \frac{1}{T} \int_0^T s(t) e^{-i\frac{2\pi t}{T}} dt. \quad (7.10)$$

At any given pixel location, the modulus $|z_T|$ depicts the amplitude of the first cardiac harmonic, whereas the argument $\arg(z_T)$ depicts its phase shift with respect to the opening time of the pulmonary valve ($t = 0$). As the conductivity increases in the lungs

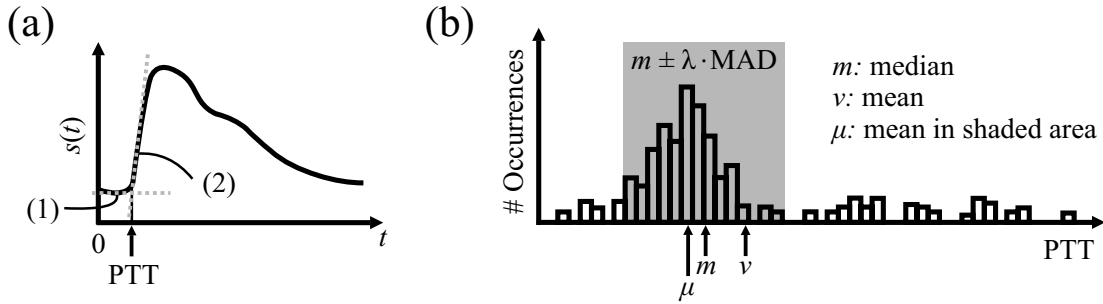


Figure 7.11 – Estimation of the pulmonary pulse transit time (PTT). (a) In each pixel of the pulmonary region of interest (ROI), the PTT is estimated using the intersecting tangent method [33]. The first tangent goes through the minimum of $s(t)$ in (1), while the second tangent passes through the maximum of its first time derivative in (2). The PTT is found at the intersection of both tangents. (b) Histogram of PTT estimates for all pixels of the ROI, with v and m the mean and the median of all PTT values, respectively. The global PTT estimate is μ , the average of those PTT values falling within the $m \pm \lambda \cdot \text{MAD}$ interval, with $\lambda = 2.5$ and MAD the median absolute deviation [99].

and decreases in the heart shortly after cardiac ejection, the first harmonic of $s(t)$ is expected to resemble a sine wave ($\pi/2$ phase shift) in the lungs, whereas it is expected to resemble an antiphase sine wave ($-\pi/2$ phase shift) in the heart. Both types of pixels were therefore separated by using a threshold value of 0 on $\arg(z_T)$. Pixels with significant pulsatility were then identified by comparing $|z_T|$ to an automatic amplitude threshold β obtained using Otsu's method [125]. In the end, the pulmonary ROI was obtained as those pixels for which $|z_T| > \beta$ and $\arg(z_T) > 0$ (Figure 7.10).

For each pixel belonging to the pulmonary ROI, a PTT was estimated from its EIT time signal $s(t)$ using the intersecting tangent method [33], as illustrated in Figure 7.11a. With M pixels contained within the ROI, M estimates of the pulmonary PTT were obtained. Erroneous PTT estimates were expected to arise in case of excessive noise or significant influence from sources not related to pulmonary pulsatility in $s(t)$, particularly in ROI pixels located near the cardiac region. In order to mitigate for these possible erroneous PTT estimates, outliers were automatically rejected using the median absolute deviation method [99] as illustrated in Figure 7.11b. Finally, a representative pulmonary PTT value was obtained by averaging all non-rejected PTT estimates.

This whole process was carried out for all 21 vascular states summarized in Table 7.1. For each of them, the pulmonary PTT value estimated from the EIT images was then compared with the underlying PAP.

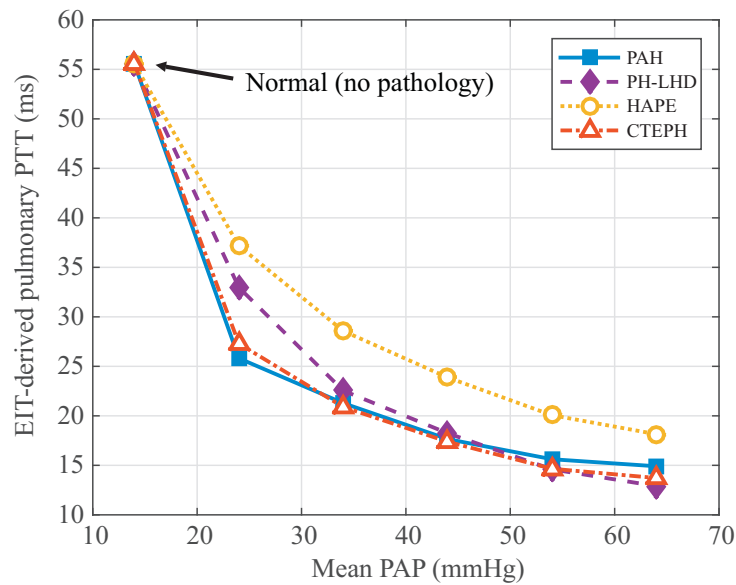


Figure 7.12 – EIT-derived pulmonary PTT for different levels of PAP and for different pathologies.

7.3 Results

Figure 7.12 shows the main findings of our study: for each type of hypertensive condition considered (PAH, PH-LHD, HAPE, CTEPH), the relation between the mean PAP and the PTT derived by EIT is shown. In the estimation of the PTT, an average of 6.9 ± 2.6 % of pixels of the pulmonary ROI were rejected as outliers by the median absolute deviation method.

The next figures aim at illustrating the inner workings of our model and approach. Figure 7.13 illustrates the morphological differences that can be observed between the pressure waveforms traveling in the pulmonary arterial tree and the resulting EIT signals. The solid lines depict an example of the pressure waveforms found at various arterial sites, from the main pulmonary artery to a pre-capillary artery, whereas the dotted line depicts the average EIT signal in the pulmonary ROI obtained in the same pathological condition.

Figure 7.14 (top panel) depicts an example of the pressure waveforms as found in a distal artery for increasing levels of PAP. For each of them, their PTT value is highlighted with a marker. Similarly, the bottom panel depicts the corresponding average EIT signal in the pulmonary ROI, with their respective PTT values also highlighted. Comparing the PTT values calculated from the pressure waveforms with those calculated from the EIT signals, correlation coefficients $r > 0.99$ ($p < 0.001$) were found for all pathologies (PAH, PH-LHD, HAPE, and CTEPH).

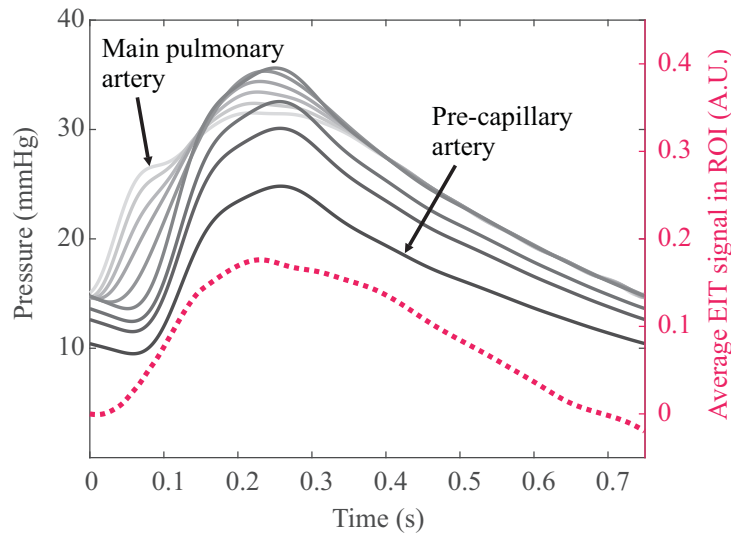


Figure 7.13 – *Solid lines*: Pressure wave propagating through the pulmonary arterial tree in a borderline pre-hypertensive case of CTEPH ($P_A = 24$ mmHg). *Dotted line*: Average EIT signal obtained in the pulmonary ROI in the same pathological condition.

7.4 Discussion

In this study, we have hypothesized that changes in PAP could be monitored non-invasively by tracking changes in pulmonary PTT via EIT. We have tested our approach in an MRI-based 4D bioimpedance model of the human thorax. An anatomical model of the entire pulmonary arterial tree was constructed using contrast-enhanced magnetic resonance angiography scans [141] for the larger arteries, and a geometrically and morphometrically accurate arterial tree growing algorithm [28] (Appendix Section A.1) for the smaller arteries. The pulsatile behavior of each arterial segment of the tree was assessed via validated hemodynamic models of the pulmonary circulation [123, 141] (Appendix Section A.2). The local conductivity change occurring in each pulmonary voxel over time was obtained from the pressure-induced change in pulmonary blood volume. Our method was evaluated in several PH conditions. Simulated EIT measurements were performed on the model and the pulmonary PTT was estimated from the resulting EIT signals.

7.4.1 EIT-based PAP monitoring

On the PTT-PAP relation

Figure 7.12 shows the main findings of the present study: it can be observed that increasing levels of PAP are associated with shorter PTT values for all forms of PH pathologies, as expected from the physiological link between pressure and PWV (higher pressures are associated with faster PWV, and thus shorter PTT). These results suggest

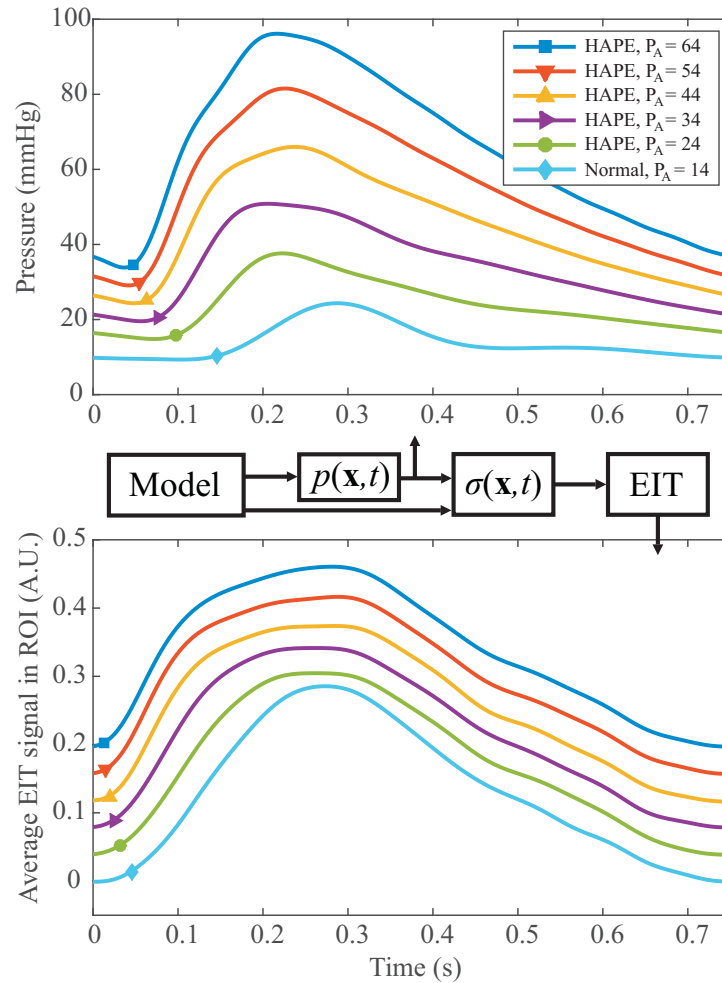


Figure 7.14 – *Top panel*: Example of pressure waveforms found in a distal artery for increasing levels of HAPE, as well as for the normal (nonpathological) case. *Bottom panel*: Corresponding average EIT signals in the pulmonary ROI. In both panels, the PTT of each waveform is highlighted by a marker. Note that the EIT signals have been given arbitrary vertical offsets for easier visualization.

that EIT *can* be used to monitor changes in pulmonary PTT, and therefore in PAP.

It can be observed from the figure that the PTT value at a given PAP level (*e.g.* $P_A = 24$ mmHg) is not necessarily the same for all pathologies. This is due to the physiological link between PWV and the structural properties of the arterial wall [180], which can strongly differ between pathologies. Conversely, in CTEPH, the arteriopathy in the nonoccluded areas strongly resembles that of PAH [128], which explains why the PAP-PTT relation is very similar for both pathologies.

Finally, the inverse exponential nature of the PTT-PAP relation shows that our PWV-based method is particularly indicated for monitoring early changes in pulmonary

Chapter 7. Model-based feasibility study on the EIT-based measurement of PAP

hemodynamics and early stages of PH. Indeed, at lower PAP values, small changes in PAP induce large changes in PTT. This is in line with the expected relationship between the PTT and the PAP, given the PWV–PAP relationship illustrated earlier in Chapter 2 (Figure 2.6). PWV has a high sensitivity to small losses in arterial distensibility at lower pressures. The same observation was drawn in intravascular ultrasound and MRI studies [96, 148], demonstrating that PWV – even more than PAP itself – is a strong predictor of survival [94, 95].

On the pressure and EIT waveforms

Several other observations, listed hereafter, can be drawn from the figures presented in Section 7.3. Although the morphology of the EIT signal roughly resembles that of the various pressure waveforms (Figure 7.13), it does not resemble one of them predominantly. In particular, the slope of the EIT signal is less steep than that of the pressure waveforms, which suggests that arteries of all sizes contribute to the generation of the EIT signal. The contribution of the small arteries is not negligible in comparison to that of the larger arteries as they are much more abundant [74].

Figure 7.14 shows how the PTT-related information carried by the pressure waveforms remains present in the EIT signals despite the aforementioned morphological differences between both types of waveforms. Note that all EIT signals depicted in Figure 7.14 (bottom panel) have similar peak-to-peak amplitudes, despite having been generated by vastly different distending pressures (top panel). This can be explained by the inverse exponential relationship between pressure (p) and arterial distensibility (δ) [180]. As PAP rises to increasingly severe levels, arterial distensibility decreases due to vascular remodeling. As a consequence, the product of p and δ , which determines the extent of arterial distension, remains almost constant throughout the physiological range of pressure values [96, 148]. Nevertheless, an amplitude decrease in the average EIT signal can be expected with an increase in PAP in cases of reduced pulmonary microvascular bed in advanced stages of PH [155].

7.4.2 Model assumptions validity, limitations, and future work

We discuss hereafter the validity of the main assumptions used in the creation of our model, as well as its main limitations and those of our approach. We then mention practical workarounds to overcome some of these limitations, and some suggested future work.

Model assumptions validity

Being based on MRI scans acquired during breath-hold, our 4D bioimpedance model does not take into account impedance changes induced by respiratory activity. Respiration does not only affect the dielectric properties of the lung parenchyma, it also deforms the internal distribution of impedance volumes as well as the external thoracic contour. However, we consider this simplification in our model to be acceptable. Our method being based on timing information (the PTT) rather than on amplitude, respiration-induced conductivity changes have limited effect on our measurement. Besides, several techniques (short apneas, respiration- and ECG-gating, frequency filtering, etc.) allow efficiently minimizing the influence of these respiratory artifacts in practice in cardiac EIT [50, 73]. Moreover, the automatic tracking of the pulmonary ROI (Section 7.2.3) can cope for possible respiration-induced changes in internal impedance distribution.

A second assumption of our model, mentioned earlier, is that the pressure downstream of our pulmonary arterial tree, *i.e.* P_W , is continuous, although it is known to be slightly pulsatile [121]. In this study, we have considered the influence of the pulsatile component of P_W to be minor not only in terms of amplitude, but also because it occurs late in the cardiac cycle: the early systolic part of the $\sigma(x, t)$ waveform (Figure 7.1), which is of interest to estimate the PTT, is not affected by the pulsatility of P_W . For this reason, its pulsatile component can, in our opinion, be neglected without any loss of relevant information.

A third assumption of our model is that the pulmonary arterial wall, known to be much thinner than its systemic counterpart [121], is of negligible thickness. The non-inclusion of the arterial wall in the model is expected to only slightly affect the *baseline* value of lung conductivity, but not its *pulsatile* behavior. The arteries will distend “at the same time” regardless of the presence (or absence) of the wall in the model. Thus only the *amplitude* of the EIT signal $s(t)$ is affected; its *timing* information (its PTT), which is of interest for PAP monitoring, remains unaffected.

Model and method limitations

A first limitation of our method concerns the timing reference used for the estimation of the PTT. In our study, $t = 0$ corresponds to the time of opening of the pulmonary valve. However, in practice, this feature is difficult to estimate non-invasively [117].

A second limitation concerns the possible influence of conductivity changes not related to pulmonary pulsatility in those lung regions close to the heart, in particular sources generating conductivity changes similar to those occurring in the lungs, such as atrial or aortic changes. Heart motion-induced displacements of the pulmonary arteries may also affect the pulmonary EIT signal in the most proximal regions of the lungs [133].

Chapter 7. Model-based feasibility study on the EIT-based measurement of PAP

A third limitation, intrinsic to models describing complex processes, is the use of physiological parameters from multiple different studies, and therefore different sources.

Practical workarounds

It is important to mention that workarounds exist in practice to try and overcome some of these limitations. For instance, PTT-based systemic blood pressure monitoring systems often use the R-wave peak of the electrocardiogram – a robust feature to detect – as surrogate timing reference ($t = 0$) for PTT estimation [117].

Erroneous PTT estimates resulting from the possible artifacts induced in the proximal regions of the lungs by sources not related to pulmonary pulsatility are expected to be automatically discarded by the outlier rejection method (Section 7.2.3) [99]. Alternatively, they could be avoided by limiting the ROI to its most distal part.

Future work

Further improvement to the present model could aim at addressing the aforementioned limitations. However, in our opinion, future work should predominantly focus on evaluating our proposed non-invasive PAP monitoring approach in real EIT data.

7.4.3 Summary and conclusion

There is currently no practical solution for the non-invasive monitoring of PAP in hemodynamically unstable patients and patients with chronic PH. We have previously demonstrated experimentally the feasibility of a novel approach based on the use of EIT for the monitoring of systemic blood pressure [157, 159]. In the present study, we have evaluated its feasibility in the pulmonary circulation for the monitoring of PAP. Our results, obtained from simulations on a 4D bioimpedance model of the human thorax, suggest that changes in PAP can indeed be monitored by EIT under various pathophysiological conditions. If confirmed in clinical data, these findings could open the way for a novel generation of non-invasive PAP monitoring solutions for patients with PH.

8 Experimental study on the EIT-based measurement of PAP

Adapted from the post-print version of [134]:

Non-invasive monitoring of pulmonary artery pressure from timing information by EIT: experimental evaluation during induced hypoxia

Martin Proença^{1,2}, Fabian Braun^{1,2}, Josep Solà¹, Andy Adler³, Mathieu Lemay¹, Jean-Philippe Thiran^{2,4}, and Stefano F. Rimoldi⁵

¹Systems Division, Centre Suisse d'Electronique et de Microtechnique (CSEM), Neuchâtel, Switzerland

²Signal Processing Laboratory (LTS5), Ecole Polytechnique Fédérale de Lausanne (EPFL), Lausanne, Switzerland

³Systems and Computer Engineering, Carleton University, Ottawa, Canada

⁴Department of Radiology, University Hospital Center (CHUV) and University of Lausanne (UNIL), Lausanne, Switzerland

⁵Department of Cardiology and Clinical Research, Inselspital Bern, University Hospital, Bern, Switzerland

Published in **Physiological Measurement**

Physiol. Meas., vol. 37, no. 6, pp. 713–726, 2016

8.1 Introduction

8.1.1 Objectives

In the previous chapter, we have proposed and evaluated the feasibility of a novel method for monitoring changes in PAP by EIT. Our simulations on a 4D bioimpedance model have indicated that EIT was indeed capable of tracking changes in PAP. In the present study, we aim at validating our method experimentally.

8.1.2 Measurement principle

As for our previous model-based study, changes in PAP will be assessed through the physiological relation linking pressure and pulse wave velocity (PWV), by tracking changes in the pulmonary pulse transit time (PTT) using EIT:

$$\text{PAP} \nearrow \iff \text{PWV} \nearrow \iff \text{EIT-derived PTT} \searrow .$$

Formally speaking, the pulmonary PTT is the time it takes for a pressure wave generated at the pulmonary valve to reach a distal arterial location in the lungs. Since the time of opening of the pulmonary valve ($t = 0$) is a feature that is difficult to estimate non-invasively, the PTT can, in practice, be approximated by the pulse arrival time (PAT) [117]. The PAT uses the R-wave peak of the ECG as reference time ($t = 0$) instead of the opening of the pulmonary valve¹. In the present study, an ECG signal will thus be measured along with the EIT data and the PAT will be used as a surrogate measure of the PTT.

8.2 Materials and methods

A summary of the methods and experimental protocol is illustrated in Figure 8.1.

8.2.1 Subjects and experimental protocol

Sixteen healthy volunteers (14 male, 2 female) were enrolled in our study. Tricuspid regurgitation – needed for the estimation of the reference PAP by Doppler echocardiography (see Section 8.2.2) – was not measurable in two of them (1 male, 1 female), leaving us with a total of fourteen subjects (age: 31 ± 6.1 years old, BMI: 24 ± 2.8 kg/m²).

The EIT data were acquired using the 16-electrode Goe-MF II device (CareFusion, Germany). An ECG was recorded using the ECG100C module (Biopac Systems, Inc., USA)

¹This approximation is equivalent to considering $\text{PTT} \propto \text{PAT}_b$ in Figure 2.7.

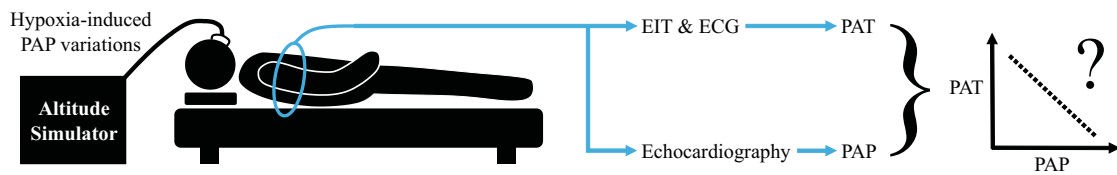


Figure 8.1 – Summary of the methods and experimental protocol. The subjects lie in supine position and pulmonary artery pressure (PAP) variations are induced by means of an altitude simulator. Tomographic (EIT), electrocardiographic (ECG), and echocardiographic measurements are performed. Pulmonary pulse arrival time (PAT) values are obtained from the joint analysis of the EIT and ECG data, whereas reference PAP values are obtained from the echocardiographic measurements. The correlation between the PAP and the EIT-derived PAT is then evaluated.

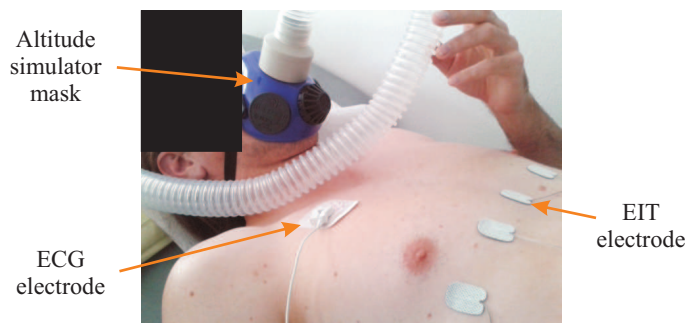


Figure 8.2 – Experimental setup showing the mask of the altitude simulator and the position of the electrodes on the subject's chest area.

and was fed into the auxiliary input of the Goe-MF II device, thus allowing the synchronous acquisition of both the EIT data and the ECG signal. The EIT measurement process is further detailed in Section 8.2.3.

In order to induce PAP variations, during parts of the protocol the subjects were breathing nitrogen-enriched air through a mask connected to an altitude simulator (AltiTrainer, SMTEC, Switzerland), as shown in Figure 8.2. Normobaric hypoxia causes vasoconstriction in the pulmonary arterial tree and therefore induces elevations of PAP. The peripheral capillary oxygen saturation (SpO_2) of the subjects was continuously monitored using the Radical-7 device (Masimo, USA), whereas their systolic pulmonary artery pressure (SPAP) was measured periodically by Doppler echocardiography (as further detailed in Section 8.2.2). Each subject was lying in supine position and underwent seven 2-minute EIT and ECG measurements at various oxygen saturation levels, as depicted and detailed in Figure 8.3. Immediately after each EIT measurement, the subjects were asked to turn on their left side in order for their SPAP to be measured by Doppler echocardiography.

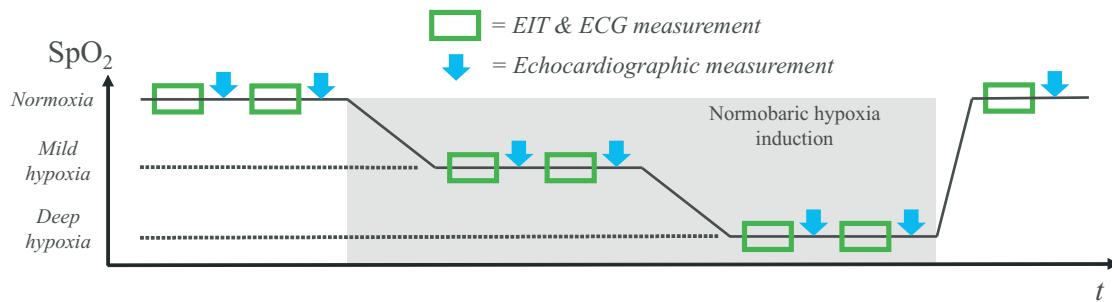


Figure 8.3 – Experimental protocol for inducing PAP variations through normobaric hypoxia: two baseline measurements in normoxia (~ 540 m, $SpO_2 \geq 95\%$), two measurements in mild hypoxia (~ 4200 m, $90\% > SpO_2 \geq 80\%$), two measurements in deep hypoxia (~ 5400 m, $80\% > SpO_2 \geq 65\%$), and one baseline measurement in normoxia. Immediately after each 2-minute EIT and ECG measurement, the subjects were asked to turn on their left side and their SPAP was measured by Doppler echocardiography.

The study was approved by the institutional review boards on human investigation of the University of Bern, Bern, Switzerland (BE 2016-00747) and registered at Clinical-Trial.gov (NCT 0296 9486). All participants provided written informed consent.

8.2.2 Echocardiographic measurements

The echocardiographic measurements were performed with a real-time, phased-array sector scanner (Acuson Sequoia 512, Siemens, Germany) with an integrated color Doppler system and transducers containing crystal sets for 2-dimensional imaging (5.0 MHz with second harmonic technology) and for continuous-wave Doppler recording (2.5 MHz). After localization of tricuspid regurgitation via Doppler color flow imaging, the maximal tricuspid regurgitation velocity v_{\max} was measured by means of continuous-wave Doppler ultrasound. As previously validated by our group in hypoxia against invasive measurements [10], the right atrioventricular pressure gradient ΔP was estimated using the modified Bernoulli equation ($\Delta P = 4v_{\max}^2$). The SPAP was estimated as $\Delta P + RAP$, where RAP (right atrial pressure) was assumed to be 10 mmHg [112]. Each reported SPAP value is the average of at least three measurements. The maximal deviation among averaged values was found to be systematically ≤ 4 mmHg.

8.2.3 EIT measurements and image reconstruction

The EIT data were acquired with 16 gel electrodes (Ambu BR-50-K, Ambu, Denmark) placed around the subjects' chest in a transversal plane at the level of the fifth intercostal space. The EIT device was configured to inject currents at 100 kHz and acquire 25 images per second. The ECG signal at the auxiliary input was sampled at 325 Hz. The EIT data were reconstructed into images of 64×64 pixels with Matlab (MathWorks, Natick, USA)

using the framework of the EIDORS toolbox [4]. The reconstruction was performed using the 2.5D human thorax model of EIDORS and the GREIT algorithm with the recommended settings [5].

8.2.4 EIT data processing

The following three sections describe the proposed automatic signal processing method for estimating one global pulmonary PAT value from each 2-minute EIT recording.

Pixel-wise signal processing. As a first step, the EIT time signal at each pixel was filtered using a high-pass (0.65 Hz) fourth-order Butterworth filter and zero-phase filtering in order to reduce the influence of respiration-related impedance changes. These components and noise were then further attenuated through ECG-gated ensemble averaging. As a result, each 2-minute EIT signal at each pixel was summarized by one representative cardiovascular-related pulse $s(t)$.

Automatic identification of the pulmonary ROI. Then, the pulmonary ROI was automatically identified using the approach previously described in Section 7.2.3. In short, at each pixel, the cardiac frequency Fourier coefficient z_T of $s(t)$ was computed (equation 7.10). As the pulmonary conductivity increases after cardiac ejection, the first harmonic of $s(t)$ was expected to resemble a sine wave in the lungs, *i.e.* $\arg(z_T) \approx \pi/2$, whereas it was expected to resemble an antiphase sine wave in the heart, *i.e.* $\arg(z_T) \approx -\pi/2$. Both types of pixels (pulmonary and cardiac) were thus separated by using a threshold value of 0 on $\arg(z_T)$. The pulmonary ROI was then defined as those pulmonary pixels ($\arg(z_T) > 0$) with a significant pulsatile amplitude, *i.e.* those where the modulus $|z_T|$ of the first cardiac harmonic was larger than an amplitude threshold automatically set using Otsu's method [125].

Estimation of the pulmonary PAT. The pulmonary PAT was also estimated as previously described in Section 7.2.3. In short, a PAT value was estimated at each pixel from $s(t)$ using the intersection tangent method [33]. With M pixels contained within the ROI, M estimates of the pulmonary PAT were thus obtained. Possible outliers were then automatically rejected using the median absolute deviation method [99]. The final pulmonary PAT was obtained by averaging all non-rejected PAT estimates.

8.3 Results

8.3.1 EIT data processing

Before presenting the comparison between the EIT-derived PAT and the reference echocardiography-derived SPAP (Section 8.3.2), the present section illustrates the various steps of the proposed EIT data processing method for estimating a pulmonary

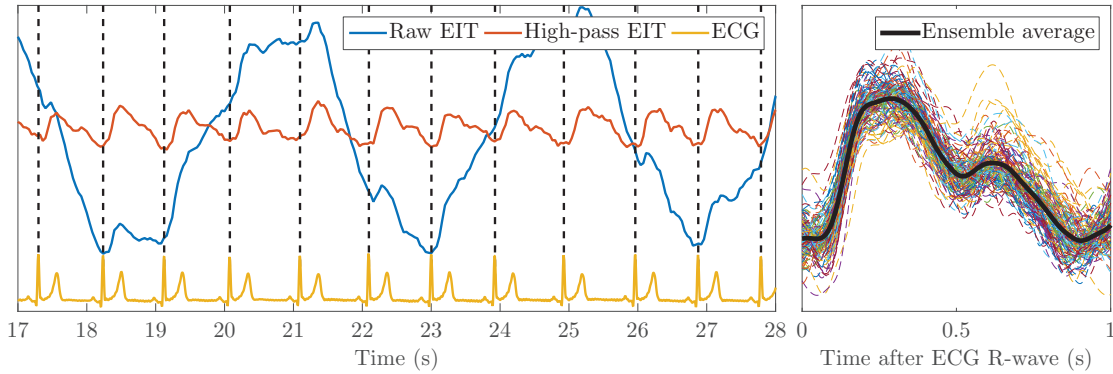


Figure 8.4 – Example of ECG-gated ensemble averaging. The “Raw EIT” curve depicts an example of EIT time signal at a given pixel in the lung region. Its large fluctuations are due to respiration, while its smaller-amplitude oscillations are induced by pulmonary arterial pulsatility. The main respiratory components of the signal are first strongly attenuated using a high-pass filter (“High-pass EIT” curve). Then, using the R-wave peak of the ECG as cardiosynchronous trigger, all cardiovascular-related pulses are aligned in time and averaged, leading to one “ensemble average” waveform representative of pulmonary arterial pulsatility in that pixel.

PAT.

Pixel-wise signal processing. Figure 8.4 illustrates the process based on ECG-gated ensemble averaging used for summarizing each 2-minute EIT time signal by one representative cardiovascular-related pulse $s(t)$ at each pixel.

Automatic identification of the pulmonary ROI. Figure 8.5 shows examples of ensemble average signals in the lung and heart regions and illustrates the discrimination between both types of waveforms using the phase shift of the first cardiac harmonic. In the lung region, the harmonic is almost in phase with a sine wave at the cardiac frequency, *i.e.* $\arg(z_T)$ is slightly above $\pi/2$. In the heart region, the opposite occurs.

Figure 8.6 illustrates an example of pulmonary ROI segmentation (dotted lines). The left panel depicts the pixel-wise modulus $|z_T|$ of the first cardiac harmonic, and the right panel its pixel-wise phase shift $\arg(z_T)$.

Estimation of the pulmonary PAT. Figure 8.7 shows examples of pulmonary ensemble average signals $s(t)$ with their corresponding PAT estimations. Small vertical offsets have been given to the signals for easier visualization.

8.3.2 EIT-based PAP monitoring

Figure 8.8 (left panels) shows the relation obtained between the EIT-derived PAT and the reference echocardiography-derived SPAP ($SPAP_{\text{echo}}$) for each subject. Figure 8.8

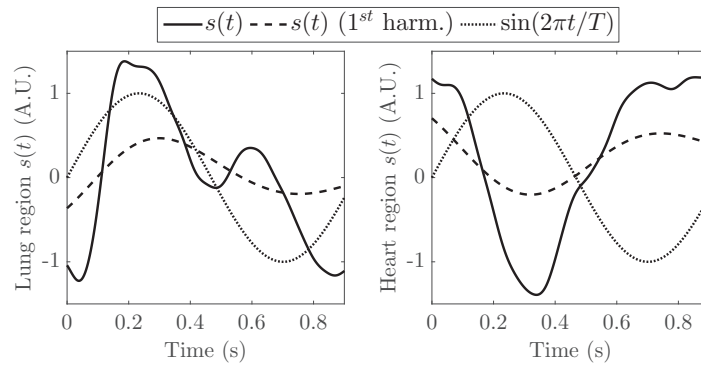


Figure 8.5 – Examples of ensemble average signals $s(t)$ in the lung (left) and heart (right) regions, along with their first cardiac harmonics. The phase shift $\arg(z_T)$ is slightly above $\pi/2$ in the lung region, where the harmonic resembles a sine wave at the cardiac frequency. The opposite occurs in the heart region, where the harmonic resembles an antiphase sine wave.

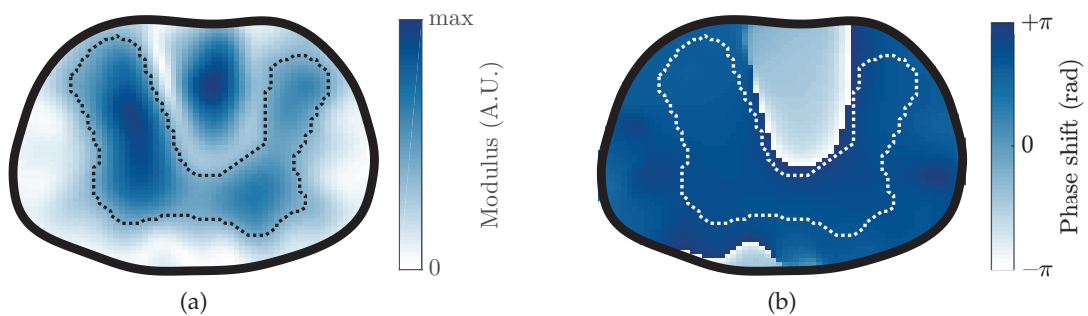


Figure 8.6 – Examples of maps depicting (a) the pixel-wise modulus $|z_T|$ of the first cardiac harmonic and (b) its phase shift $\arg(z_T)$. The dotted lines represent the automatically extracted pulmonary region of interest. The medical image orientation (right side on the left) is used.

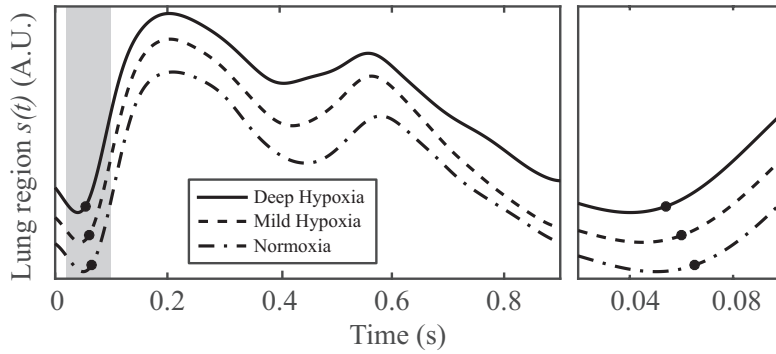


Figure 8.7 – *Left panel*: examples of pulmonary ensemble average signals in normoxia, mild hypoxia and deep hypoxia. The estimated PAT of each curve is indicated by a dot. Small vertical offsets have been added to the curves for easier visualization. *Right panel*: zoom on the shaded area of the left panel.

(center panels) shows the relation between $SPAP_{\text{echo}}$ and $SPAP_{\text{EIT}}$, the EIT-derived SPAP estimate obtained using a least-square linear fit of the PAT onto $SPAP_{\text{echo}}$. Finally, Figure 8.8 (right panels) shows the agreement between $SPAP_{\text{echo}}$ and $SPAP_{\text{EIT}}$ using a Bland-Altman plot [19].

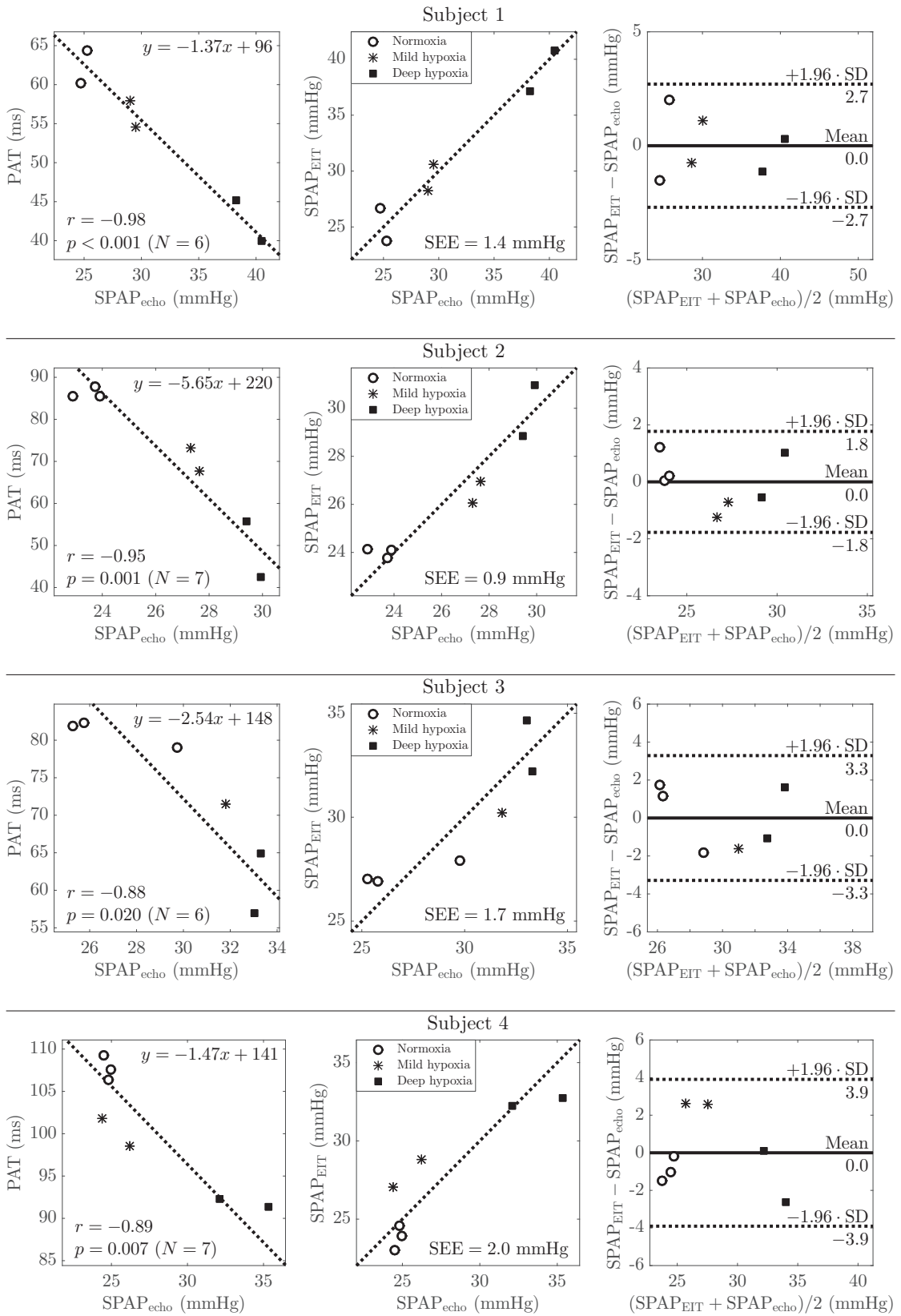
Each data point represents a 2-minute EIT recording and its corresponding echocardiographic measurement. Note that the first recording (first measurement in normoxia) in subject 1 and the third recording (first measurement in mild hypoxia) in subject 3 could not be used due to ECG and EIT recording issues, respectively. As summarized in Table 8.1, Pearson’s correlation coefficients (r) in the range $[-0.70, -0.98]$ (average: -0.89) were obtained between the PAT and $SPAP_{\text{echo}}$. Standard errors of the estimate (SEE) in the range $[0.9, 6.3]$ mmHg (average: 2.4 mmHg) were obtained between $SPAP_{\text{EIT}}$ and $SPAP_{\text{echo}}$.

Finally, Figure 8.9 shows the relation and agreement between $SPAP_{\text{EIT}}$ and $SPAP_{\text{echo}}$ for all subjects together.

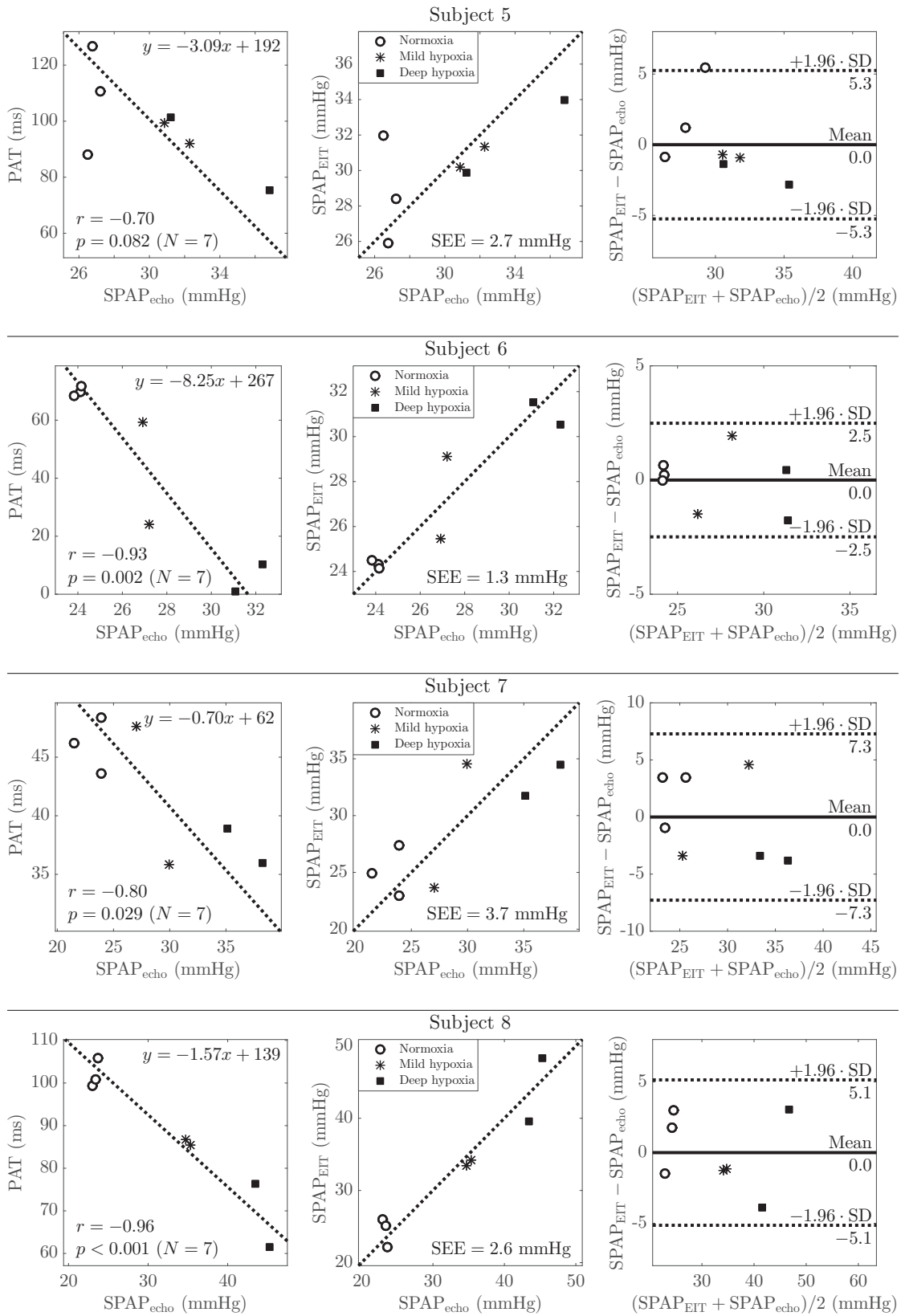
8.4 Discussion

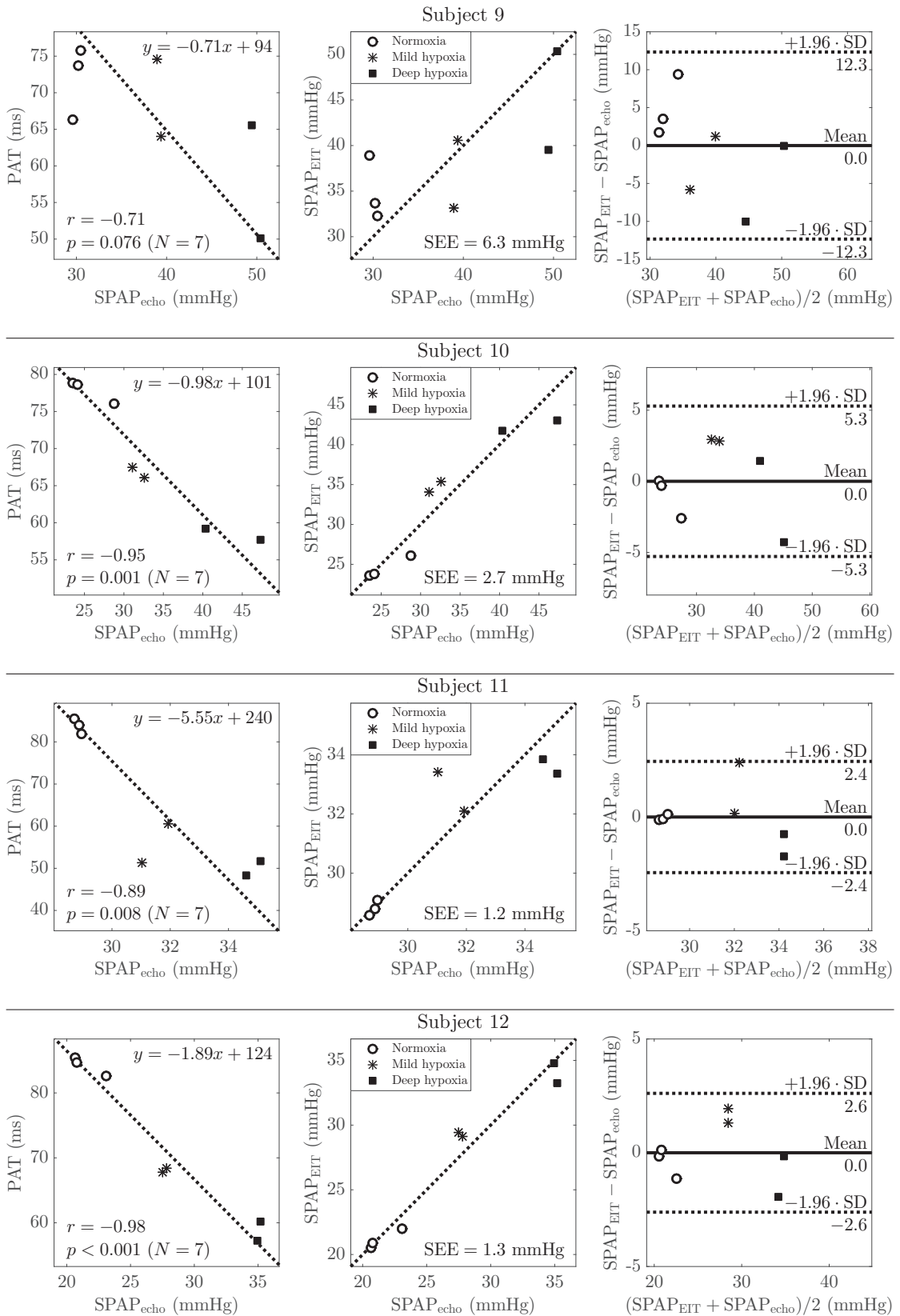
8.4.1 Unsupervised and non-invasive PAP monitoring

In this study, we have presented experimental evidence of the feasibility of tracking changes in PAP non-invasively via EIT. Changes in PAP were induced by hypoxic vasoconstriction in fourteen healthy subjects, and reference SPAP values were obtained from echocardiographic measurements.



Chapter 8. Experimental study on the EIT-based measurement of PAP





Chapter 8. Experimental study on the EIT-based measurement of PAP

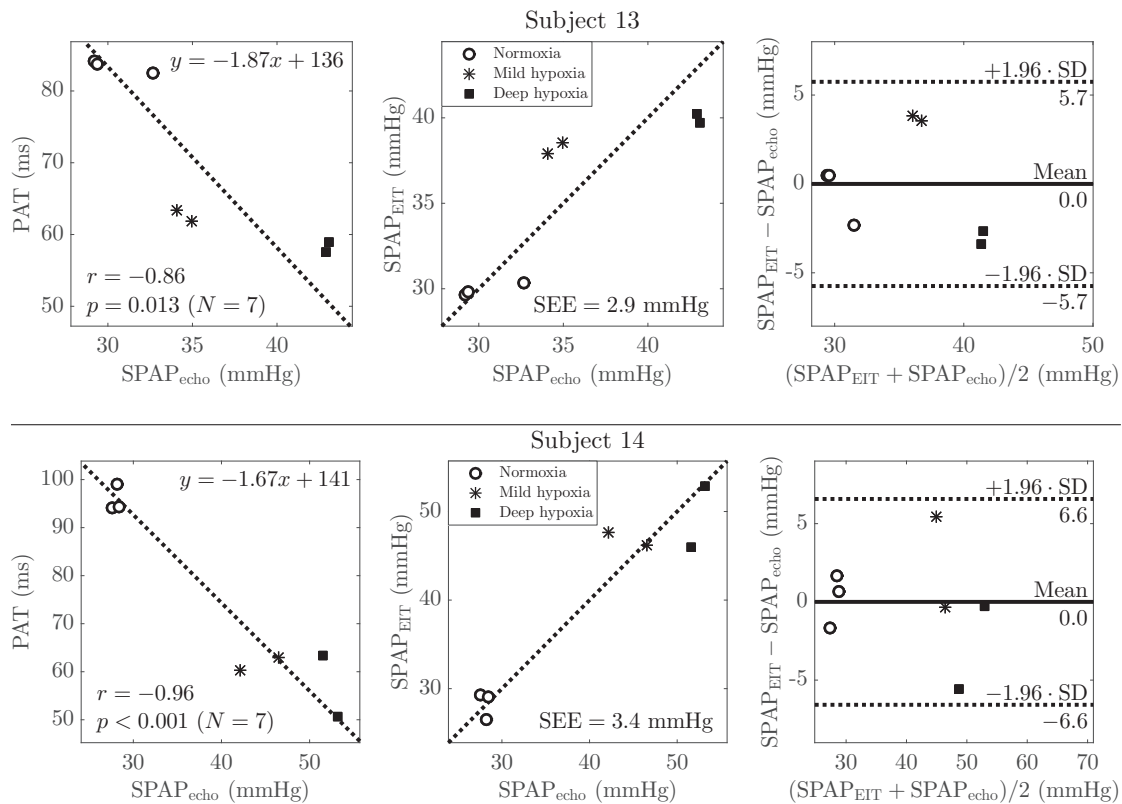


Figure 8.8 – EIT-based PAP monitoring: experimental results for each subject. *Left-side panels:* comparison of the EIT-derived pulse arrival time (PAT) against the echocardiography-derived systolic pulmonary artery pressure (SPAP_{echo}). The Pearson’s correlation coefficient (r) between both quantities is indicated. The dotted lines depict least-square linear fits and their equations ($y = a \cdot x + b$) are given. *Center panels:* comparison of SPAP_{EIT} – the EIT-derived estimate of SPAP obtained via a least-square linear fit of the PAT onto SPAP_{echo} – with SPAP_{echo}. The standard error of the estimate (SEE) is indicated. *Right-side panels:* Bland-Altman plot [19] between SPAP_{EIT} and SPAP_{echo}. The dotted lines indicate the 95 % limits of agreement.

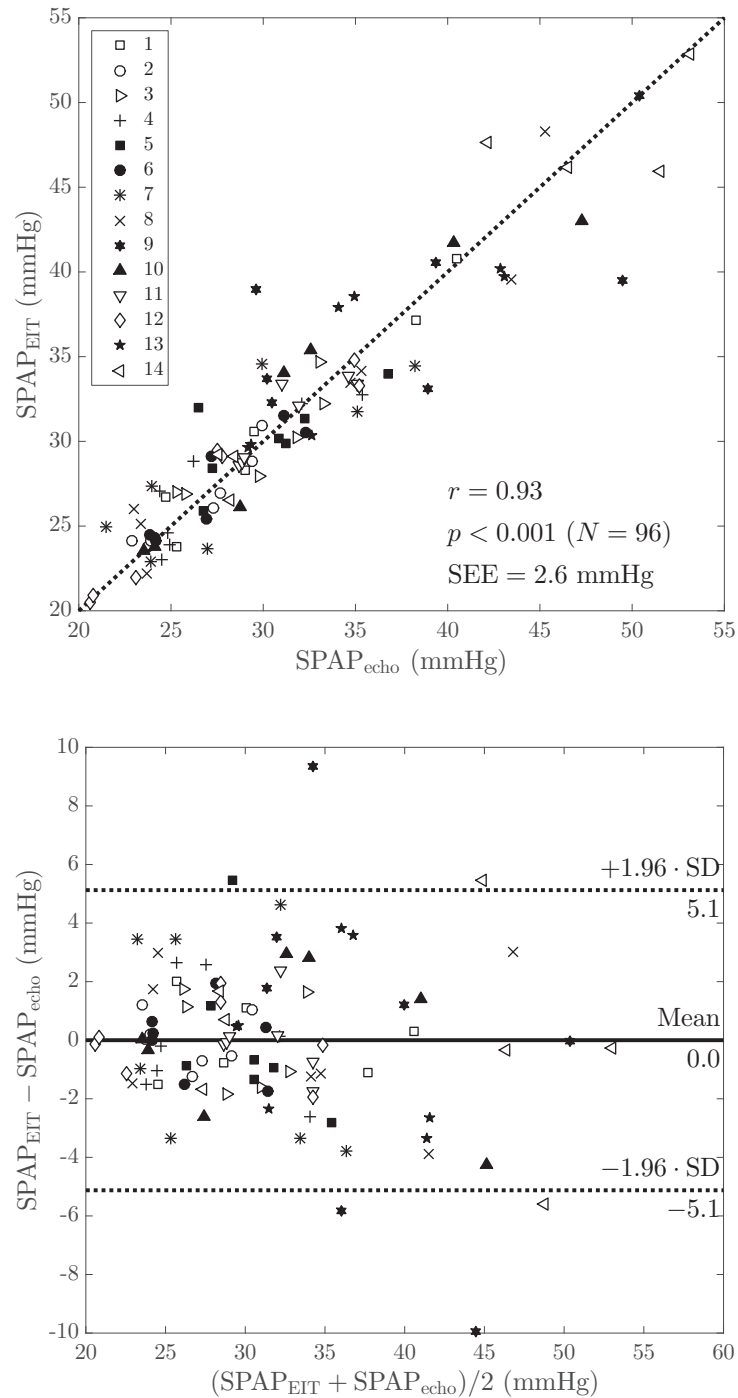


Figure 8.9 – EIT-based PAP monitoring: experimental results for all subjects. *Top panel:* comparison of $SPAP_{EIT}$ with $SPAP_{echo}$. Each type of marker corresponds to a subject. The Pearson's correlation coefficient (r) and the standard error of the estimate (SEE) between both quantities are indicated. *Bottom panel:* Bland-Altman plot [19] between $SPAP_{EIT}$ and $SPAP_{echo}$. The dotted lines indicate the 95 % limits of agreement.

Chapter 8. Experimental study on the EIT-based measurement of PAP

Table 8.1 – EIT-based PAP monitoring: experimental results for all subjects. “Pearson’s r ” column: Pearson’s correlation coefficient between the EIT-derived PAT and the reference echocardiography-derived SPAP ($SPAP_{\text{echo}}$). “SEE (mmHg)” column: standard error of the estimate between $SPAP_{\text{EIT}}$ and $SPAP_{\text{echo}}$ ($SPAP_{\text{EIT}}$: EIT-based SPAP estimate obtained via a per-subject linear least-square fit of the PAT onto $SPAP_{\text{echo}}$).

Subject	Pearson’s r PAT vs. $SPAP_{\text{echo}}$	SEE (mmHg) $SPAP_{\text{EIT}}$ vs. $SPAP_{\text{echo}}$
1	−0.98	1.4
2	−0.95	0.9
3	−0.88	1.7
4	−0.89	2.0
5	−0.70*	2.7
6	−0.93	1.3
7	−0.80	3.7
8	−0.96	2.6
9	−0.71*	6.3
10	−0.95	2.7
11	−0.89	1.2
12	−0.98	1.3
13	−0.86	2.9
14	−0.96	3.4
Average	−0.89	2.4
Range	[−0.70, −0.98]	[0.9, 6.3]

* $p < 0.1$ ($p < 0.05$ otherwise).

Performance

For all subjects high correlation scores ($r \in [-0.70, -0.98]$, average: -0.89) were found between our EIT-derived PAT estimates and the reference $SPAP_{\text{echo}}$ values. Despite the relatively small range of PAP variations induced through normobaric hypoxia (< 10 mmHg in several subjects), the sensitivity of the EIT-derived PAT has shown to be sufficient for tracking these small variations.

For all subjects small standard errors of the estimate ($SEE \in [0.9, 6.3]$ mmHg, average: 2.4 mmHg) were found between $SPAP_{\text{EIT}}$ and $SPAP_{\text{echo}}$. In our study, $SPAP_{\text{EIT}}$ was obtained using a least-square linear fit of the PAT onto $SPAP_{\text{echo}}$. Therefore, the reported SEE values are the best achievable given the PAT values obtained. In practice, converting measured PAT values to $SPAP_{\text{EIT}}$ would require an individual calibration to be trained beforehand, possibly using three or four paired PAT- $SPAP_{\text{echo}}$ measurements to estimate the regression line.

Subject dependence of the PAT-SPAP relation

From Figure 8.8 (left panels), it can be observed that the relation between the PAT and $\text{SPAP}_{\text{echo}}$ ($y = a \cdot x + b$) is different for each subject. This can be explained by several subject-dependent factors influencing the PAT, in particular:

- a) *The duration of the pre-ejection period (PEP).* As mentioned in Section 8.1, the PAT is an approximation of the PTT and, formally speaking, is equal to $\text{PEP} + \text{PTT}$ [117]. The duration of the PEP is subject-dependent.
- b) *The dimensions of the lungs.* The PAT depends on the length of the arterial pathway traveled by the pressure pulse. This distance depends on the dimensions of the lungs, which are also subject-dependent.
- c) *The compliance of the arteries.* Arterial compliance, which is also subject-dependent, affects both the PAP (by affecting the cardiac afterload) and the PAT (through its link with PWV).

This is the reason why our approach is better suited for monitoring intra-subject *trends* in PAP rather than absolute pressure values, which require an individual calibration procedure to be performed.

Signal processing method

In this work we have proposed a fully unsupervised EIT-based method for the estimation of the pulmonary PAT. This method makes heavy use of the cardiosynchronicity offered by the ECG signal. ECG-gated ensemble averaging significantly increases the signal-to-noise ratio of the EIT signals without distorting them [139], while the use of the phase shift with respect to the R-wave peak of the ECG for the segmentation of the pulmonary ROI is simple, effective, and physiologically consistent. Furthermore, the proposed method is resilient to erroneous or inaccurate PAT estimates through the use of the median absolute deviation method in the estimation of the pulmonary PAT. In this respect, one particular source of erroneous PAT estimates may be the thoracic aorta, which is known to produce impedance changes that are detectable by EIT [157]. Their quasi-synchronicity with the pulmonary cardiovascular-related impedance changes might allow some pixels depicting aortic influence to be mistakenly included in the pulmonary ROI. Our approach is expected to be resilient against such pixels for two reasons: (1) as mentioned above, pixel-wise PAT estimates that are not consistent with the majority are rejected by the median absolute deviation method; (2) because of the small size (in the transverse EIT plane) of the thoracic aorta in comparison with the lungs, only a small percentage of all ROI pixels will/might be influenced by the aortic signal. Therefore, if not rejected as outliers, their influence is severely reduced by the averaging of all non-rejected PAT estimates.

8.4.2 Limitations and future work

Even though this study reveals novel and promising results, it is mainly limited by the use of Doppler echocardiography as reference instead of the invasive pulmonary artery catheter. In some subjects, echocardiography-derived SPAP measurements can be inaccurate, depending on the strength of the tricuspid regurgitation signal [56]. A future clinical validation of our approach should therefore use the gold standard pulmonary artery catheter as reference.

Furthermore, it would also be interesting to investigate the long-term monitoring capabilities of our EIT-based PAP estimation method. In particular, the two following aspects should be examined:

- a) *The influence of the position of the EIT belt.* We can assume that a belt positioned slightly higher or lower would influence the PAT since the average distance traveled by the pressure waves to reach the EIT plane would have changed. For instance, assuming that a 2 cm vertical belt displacement changes the average traveled distance by the same extent, a pressure wave traveling at 2 m/s would see its PAT change by 10 ms. Given the PAT-SPAP relations found in this study, this would translate to an error of 4.8 ± 2.8 mmHg in SPAP. We believe that quantifying this error experimentally is of particular importance, as it is probably the main factor impacting the repeatability of EIT measurements.
- b) *The stability of the PAT-to-SPAP calibration over time.* Many systemic blood pressure monitors based on the measurement of PWV require to be frequently recalibrated due to their dependence on signals measured at the periphery [158]. Peripheral arteries are subjected to vasomotion (spontaneous change in vascular tone), which affects the PWV by a change in arterial compliance. Conversely, central elastic arteries – such as the aorta or the pulmonary arteries – are *not* subjected to vasomotion [121]. The PAT-to-SPAP calibration should therefore – in theory – remain unaffected over days/weeks. Again, we believe that verifying this assumption experimentally is of particular importance.

8.4.3 Summary and conclusion

The measurement of PAP in hemodynamically unstable patients or patient with chronic pulmonary hypertension is currently limited to invasive solutions (pulmonary artery catheter) or solutions that are not conducive with continuous monitoring (Doppler echocardiography). We have proposed a novel non-invasive and unsupervised PAP monitoring method based on the use of EIT. The feasibility of our approach was evaluated in fourteen healthy subjects undergoing hypoxia-induced PAP variations. Strong correlation scores ($r \in [-0.70, -0.98]$) between echocardiography-derived SPAP measurements and our EIT-derived parameter were found in all subjects, suggesting that

EIT is a candidate technology for the non-invasive and continuous monitoring of PAP.

Conclusions **Part IV**

9 Synthesis

The purpose of this thesis was to investigate the clinical potential of electrical impedance tomography (EIT) as an hemodynamic monitor for the measurement of cardiac output (CO) and pulmonary artery pressure (PAP).

More precisely, this thesis aimed at determining and quantifying the influence of heart motion and belt position/displacement on the accuracy of the EIT-based measurement of CO (Part II). Furthermore, this thesis aimed at proposing and investigating the feasibility of a novel method for the EIT-based measurement of PAP, and to test it *in vivo* (Part III).

9.1 On the EIT-based monitoring of cardiac output

Over the course of this dissertation, we have highlighted the clinical importance of being able to continuously monitor changes in CO – particularly in hemodynamically unstable patients – and the need for a non-invasive alternative to the controversial pulmonary artery catheter (PAC). We have then emphasized the limitations of current non-invasive CO monitors, especially their dependence on *peripheral* signals, resulting in the requirement of frequent recalibration. In this context, EIT – which measures *central* signals – appeared as an attractive alternative solution.

9.1.1 Influence of heart motion

In the literature, the measurement of CO by EIT is implicitly based on the hypothesis that the *EIT heart signal* (the ventricular component of the EIT signals) is generated exclusively by changes in blood volume in the ventricles. However, *heart motion* (cardiobalistic effects) is suspected to have a non-negligible influence in the genesis of this signal due to its ability to generate ventricular-like impedance changes. Therefore, in Chapter 5, we aimed at quantifying the contribution of heart motion in the genesis of the EIT heart signal and at determining its impact on the accuracy of EIT-based stroke volume (SV)

estimation. Our investigations have revealed that heart motion, through the interaction of the myocardium with its surrounding tissues, is the main contributor to the genesis of the EIT heart signal (by $\sim 56\%$). Moreover, our simulations showed that a strong correlation ($r > 0.97$) exists between the impedance changes induced by heart motion and those induced by the variations in ventricular blood volume. We explained this correlation by the quasi-incompressibility of blood and myocardial tissue, which forces these two effects to act in concert. As a result – although dominated by effects related to heart motion – the amplitude of the EIT heart signal was found to remain strongly correlated with changes in SV ($r > 0.99$), thereby demonstrating the feasibility of monitoring CO changes using EIT with high accuracy (error of 0.57 ± 2.19 mL, or $1.02 \pm 2.62\%$, on the estimation of SV).

Besides, our observations suggested that the amplitude of the motion-related component of the EIT heart signal is modulated by respiratory activity, which could affect the accuracy of the EIT-based measurement of SV. As a practical workaround, we have suggested the use of respiration-gated EIT measurements. Such a solution could solve the aforementioned issues, at the cost of limiting the responsiveness of EIT for CO monitoring, of particular importance during hemodynamic instability.

Importantly, our results also suggest that the EIT-based measurement of CO may be compromised in particular pathological conditions, such as large pericardial effusion. In such cases, heart motion is not limited to the normal deformation of the myocardium, but also to its *displacements* in the pericardial cavity. The resulting mechanical interactions of the heart with its surrounding tissues – unrelated to SV – are likely to significantly affect the EIT heart signal. We have also explained that other pathologies, such as valvular insufficiencies, are likely to compromise the EIT-based measurement of CO, as the EIT heart signal does not account for the volume of blood being pushed back through the faulty valve.

9.1.2 Influence of belt position and displacement

In Chapter 6, we investigated a practical difficulty inherent to the measurement of CO by EIT, namely the adequate placement of the belt along the long axis of the heart. This position is assumed to minimize the influence of pulsatile sources unrelated to ventricular activity on the EIT heart signal [171], but is hardly achievable in practice without the use of another imaging modality to verify the placement.

For less optimal belt placements commonly used in cardiac EIT, our experiments have shown that the EIT heart signal is still dominated by ventricular activity, but is also influenced by non-negligible pulmonary, atrial and – to a lesser extent – aortic pulsatile components. According to our preliminary findings, these non-ventricular influences on the EIT heart signal do not compromise the measurement of CO by EIT.

9.2. On the EIT-based monitoring of pulmonary artery pressure

Our investigations have also revealed a limiting aspect concerning the placement of the belt, namely the influence of a *displacement* on the accuracy of the estimation of CO. This influence was found *not* to be negligible, with errors up to 30 mL on the estimation of SV. Our results suggest that even small displacements (1-2 cm) may require the EIT signal to be recalibrated if absolute CO values are necessary.

9.1.3 Summary

In summary, our CO-related studies indicate that:

- a) It is possible to monitor changes in CO non-invasively by EIT, despite the dominantly motion-related origin of the EIT heart signal.
- b) The accuracy of EIT-based CO estimation may be affected by respiratory activity. Furthermore, the measurement could even be compromised under specific pathological conditions such as severe pericardial effusion and valvular insufficiencies.
- c) Belt placements commonly used in cardiac EIT – although suboptimal for the measurement of CO – can reliably track changes in SV. Oblique placements, which allow obtaining a larger ventricular contribution in the EIT heart signal, should be preferred over transverse placements.
- d) When absolute CO values (rather than just trends) are needed, a recalibration of the measurement is strongly advised in events of displacement or repositioning of the EIT belt.

9.2 On the EIT-based monitoring of pulmonary artery pressure

In clinical settings, the continuous monitoring of PAP is currently limited to the invasive PAC, with the known non-negligible risks associated with its use. Doppler echocardiography, although non-invasive, is not conducive with continuous monitoring due to its dependence on a medical doctor to perform the measurement. Moreover, only 50–80 % of patients have sufficient tricuspid regurgitation for the measurement to be performed [37, 40]. Thus, the clinical need for a non-invasive and unsupervised solution to monitor the PAP is strong.

9.2.1 Feasibility of a novel non-invasive method

We have proposed a novel method for monitoring the PAP from EIT measurements. The method is based on the physiological relation linking blood pressure and the pulse wave velocity (PWV), the speed of propagation of the pressure waves in the arteries.

In Chapter 7, we demonstrated via simulations the validity of our method for several types of pulmonary hypertensive conditions and various degrees of disease severity. Our results, which demonstrate a logarithmic relation between the pulmonary PWV and the PAP, are in line with physiological expectations (see Section 2.5). PWV has a high sensitivity to small losses in arterial distensibility at lower pressures. The same observation was drawn in intravascular ultrasound and MRI studies [96, 148], demonstrating that PWV – even more than PAP itself – is a strong predictor of survival [94, 95]. Our PWV-based method is therefore particularly indicated for monitoring early changes in pulmonary hemodynamics.

9.2.2 *In vivo* evaluation

In Chapter 8, we tested our novel PAP monitoring method *in vivo*. To that end, we induced elevations in PAP in fourteen healthy volunteers by subjecting them to various levels of normobaric hypoxia. Our results demonstrated strong correlations ($r \in [-0.70, -0.98]$, average: -0.89) between our EIT-derived PWV-related parameter – the pulse arrival time (PAT) – and measurements of systolic PAP obtained by echocardiography, thereby allowing a first experimental validation of our method. When converting the measured PAT values to pressure units using per-subject calibrations, small standard errors of the estimate were obtained ($SEE \in [0.9, 6.3]$ mmHg, average: 2.4 mmHg).

From a signal processing perspective, the proposed method has the advantage of being simple, robust and fully unsupervised, particularly regarding the selection of the region of interest – often a critical task in EIT given the fact that electrical tomographs are poor anatomical references.

Besides, it is important to note the subject-dependent relation between the PAT and the PAP, which prevents any inter-subject PAT comparison at similar PAP levels. We explained these differences by the anatomical (*e.g.* lung dimensions) and physiological (*e.g.* duration of the pre-ejection period, compliance of the pulmonary arteries) differences existing between individuals.

Finally, it is worth mentioning that our studies on PAP have not investigated the influence of a displacement of the EIT belt, likely to be the main factor affecting the repeatability of the measurement. We can assume that the PAT would be different since the average distance traveled by the pressure waves to reach the EIT plane would have changed. The extent of this difference – that we roughly estimated to be ~ 5 mmHg for a 2 cm vertical belt displacement – remains to be formally quantified experimentally. Similarly, the stability of the per-subject PAT-to-PAP calibration over time – hypothesized to be guaranteed due to the absence of vasomotion (spontaneous changes in vascular tone) in the pulmonary arteries – remains to be verified experimentally.

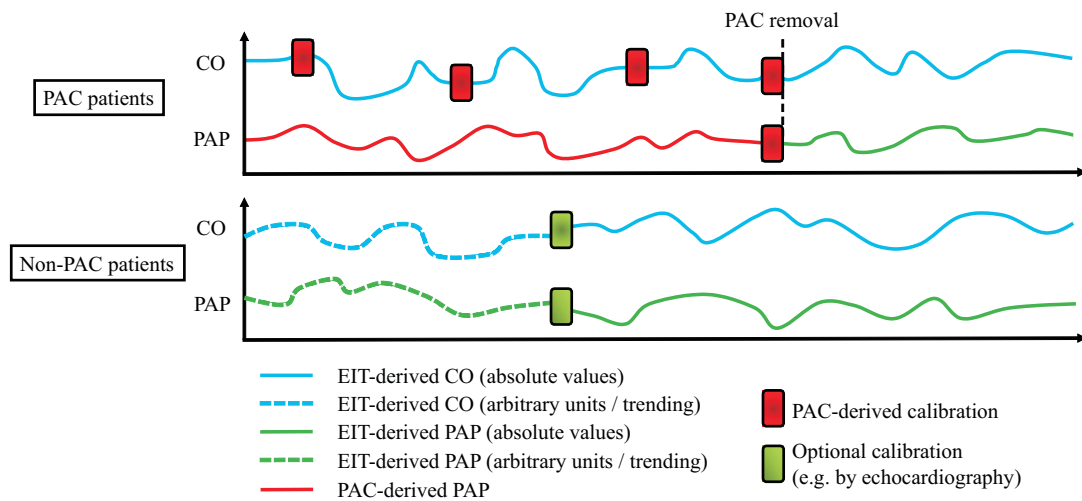


Figure 9.1 – Perspectives of EIT in intensive care units for the monitoring of CO and PAP. In patients undergoing right heart catheterization (“PAC patients”), EIT could be used to extend the measurement after removal of the PAC, and to allow the monitoring of short-term trends in-between the intermittent CO measurements by the PAC. In patients *not* undergoing right heart catheterization (“Non-PAC patients”), EIT could be used to monitor otherwise unknown trends and, when possible and necessary, could be calibrated using a non-invasive modality such as transthoracic echocardiography to provide absolute values of CO or PAP.

9.2.3 Summary

In summary, our PAP-related studies indicate that:

- a) It is possible to monitor changes in PAP non-invasively by EIT.
- b) The pulmonary PWV being a strong predictor of survival [94, 95], our PWV-based method is particularly indicated for the detection of early changes in pulmonary hemodynamics. In contrast, our method is likely to be less sensitive to small changes in PAP at higher pressures (*i.e.* in case of severe pulmonary hypertension).
- c) The monitoring of absolute pressure values requires an individual calibration (*e.g.* by echocardiography). A universal (population-wise) calibration is unlikely to be found given the numerous subject-specific factors influencing the PAT.
- d) The effects of a displacement of the EIT belt on the estimation of the PAP and the stability of per-subject PAT-to-PAP calibrations remain to be investigated experimentally.

9.3 Perspectives in intensive care units

The use of EIT in clinical settings is still in its early stages. In this section we aim at determining what its main area of use could be as a non-invasive CO and/or PAP monitor, particularly in intensive care units. Figure 9.1 illustrates this concept. We consider two situations/scenarios, depending whether the patient is equipped with a PAC (“PAC patients”) or not (“Non-PAC patients”).

In PAC patients, CO is obtained intermittently from the PAC. EIT could therefore be used to track short-term CO variations in-between consecutive PAC measurements, using the latter as a calibration means to provide continuous absolute CO trends. Furthermore, EIT could allow extending the monitoring after removal of the PAC. Its calibration being independent of peripheral effects such as vasomotion, it is expected to remain valid over a sustained period of time.

Regarding the measurement of PAP in PAC patients, the utility of EIT would be to provide a continuous monitoring after removal of the PAC, using the latter as a calibration means to provide continuous absolute PAP trends. Here also, the calibration is expected to remain valid over a sustained period of time, as the pulmonary arteries are not subjected to vasomotion [97].

In non-PAC patients, EIT by itself (uncalibrated) could be used to provide otherwise unavailable CO and PAP *trends*. Trends (rather than absolute values) are of particular clinical importance in events of circulatory shock. A non-invasive access to such trends could also have a significant impact for vulnerable patients, such as newborns or children. For instance, for conditions such as persistent newborn pulmonary hypertension, there is a strong reluctance in exposing the patients to invasive procedures, and alternatives are limited [51]. When needed and possible, a calibration by means of an alternative modality (*e.g.* transthoracic echocardiography) could allow translating the measured EIT values to absolute units of CO or PAP (green blocks in Figure 9.1).

9.4 Original contributions

The original contributions of the present thesis can be summarized as follows.

- a) The creation of a dynamic 2.5D bioimpedance model dedicated to investigating the influence of cardiobalistic effects (heart motion) on the EIT heart signal.
- b) The demonstration via simulations on the model of the feasibility of tracking changes in CO by means of EIT with good accuracy – despite the dominantly cardiobalistic origin of the EIT heart signal – and the identification of factors that may affect this accuracy.

- c) The creation of a 4D bioimpedance model of the pulmonary vasculature capable of realistically simulating pulmonary hemodynamics in various cases of pulmonary hypertension.
- d) The development of a novel non-invasive and unsupervised PAP monitoring method based on the use of EIT and the measurement of changes in pulmonary pulse wave velocity.
- e) The demonstration, via simulations on the aforementioned model, of the feasibility of tracking changes in PAP by means of the proposed method in various cases of pulmonary hypertension.
- f) The validation *in vivo* of the proposed method in healthy subjects undergoing acute changes in PAP through hypoxia.

9.5 Limitations and future work

9.5.1 EIT-based CO monitoring

Our investigations have provided novel insights about the genesis of the EIT heart signal, and helped to determine the physiological and metrological requirements for an accurate measurement of CO by EIT. However, our observations remain limited by the absence of experimental validation. In our opinion, future work should therefore mainly focus on carrying out a clinical trial, *e.g.* before and after anesthesia in patients undergoing cardiac surgery, using PAC thermodilution CO measurements as reference. Patients with valvular insufficiencies or large pericardial effusion should be excluded.

Changes in SV could be induced using the passive leg raising maneuver, used to predict fluid responsiveness in critically ill patients [116]. This maneuver consists in elevating the legs of the patient from the supine position by a 30–60° angle, which allows increasing the cardiac preload and thereby increasing SV. The so-called semi-recumbent position has the opposite effect: the patient's trunk is raised from the supine position by a 30–60° angle, thus decreasing the cardiac preload and thereby decreasing SV. Using these two maneuvers along with the baseline supine position would therefore allow generating SV variations to evaluate the trending ability of EIT. These maneuvers are non-invasive and easy to perform, and could therefore be repeated twice to increase the number of paired EIT-PAC measurements. Furthermore, they could also be repeated after anesthesia, as the baseline CO is likely to have changed. As a results, a series of 6 to 12 paired EIT-PAC measurements would be obtained for each patient, which is sufficient to assess trending ability [36].

According to our observations, careful consideration should be given to the following aspects regarding the EIT measurements:

- a) The EIT belt should be placed in the oblique plane as described in [171] to maximize ventricular contribution to the EIT heart signal.
- b) If feasible during the experimental protocol, typically before anesthesia at baseline condition, the belt should initially be placed ~ 1.5 cm below the desired position, then ~ 1.5 cm above, and finally at the desired position. At each position, EIT measurements paired with PAC measurements should be performed. These measurements should allow quantifying the influence of belt displacements on SV estimation experimentally.
- c) During the remainder of the protocol, particular attention should be paid to minimize the displacements of the belt.
- d) During data analysis, we suggest the use of respiration-gating. The influence of respiratory activity on the accuracy of the EIT-based measurement of CO should be formally quantified by comparing the estimation errors obtained when respiration-gating is or not used.

9.5.2 EIT-based PAP monitoring

A novel method for the non-invasive monitoring of PAP by EIT has been proposed and validated both through simulations and experimentally. However, our experimental study comprises some limitations, such as the use of Doppler echocardiography as reference instead of the gold standard PAC. Although validated against PAC measurements [10, 37, 108], echocardiographic measurements of the PAP can still be inaccurate in the individual patient [56]. A future clinical study in patients should therefore use the PAC as reference.

In such a study, PAP variations could for instance be induced after anesthesia by decreasing the inspired oxygen fraction in the ventilator, causing hypoxic pulmonary vasoconstriction and increases in PAP. Alternatively, decreases in PAP could be induced via inhaled nitric oxide, a selective pulmonary vasodilator used for the treatment of patients with pulmonary hypertension and hypoxemia [76]. As the PAC and EIT both provide continuous beat-to-beat readings, a large amount of paired PAC-EIT measurements could thus be obtained and allow testing the beat-to-beat trending ability of EIT for PAP monitoring.

Another particularly important aspect to be investigated is the stability over time of the PAT-to-PAP calibration, in particular for the long-term monitoring of patients with chronic pulmonary hypertension. This implies testing:

- a) The influence of a different positioning of the EIT belt, which directly affects the calibration itself as it affects the PAT;

- b) The repeatability of the calibration at intervals of weeks/months on a same subject.

To test both of these aspects, a study should be conducted in patients with chronic pulmonary hypertension undergoing right heart catheterization during at least two different visits at the clinic. During the first visit, the following experimental protocol should be performed:

- a) The belt placement should be precise and easily reproducible. We suggest a placement at the level of the fifth intercostal space, as was done in our experimental study. Distance measurements between the belt and anatomical reference points should be performed, in order to facilitate the placement of the belt at the exact same location during the next visit.
- b) Once the belt in place, simultaneous PAC and EIT measurements should be performed.
- c) If not occurring naturally, small PAP variations should be induced in order for a calibration function to be trainable. To do so, using the aforementioned passive leg raising maneuver and semi-recumbent positions may be sufficient to induce small PAP variations (~ 6 mmHg) [97, 98]. Alternatively, inhalation of nitric oxide via a face mask could be performed. During the procedure, PAC and EIT measurements should be performed continuously and a PAT-to-PAP calibration function trained.
- d) Then, the belt should be shifted vertically by a small amount (*e.g.* 1.5 cm) above the original position, and simultaneous PAC and EIT measurements should be performed. The procedure should be repeated with a downward shift of the belt. The measured PAT values should then be converted to pressure units using the previously trained calibration function, and compared with the PAC-derived PAP values. This should allow quantifying the influence of changes in belt position on the accuracy of EIT-based PAP estimation.
- e) Finally, during the next visit of the patient to the clinic, the belt should be positioned as close as possible to the initial placement. EIT measurements should be performed and the PAT values obtained – converted to PAP values using the previously trained calibration function – should be compared to the PAC-derived PAP values. This should allow assessing the long-term stability of the calibration function.

9.6 Conclusion

In conclusion, this thesis has – on the one hand – identified the dominantly cardiobalistic origin of the EIT heart signal. We have described how the impedance changes induced by these cardiobalistic effects correlate with ventricular volume, and identified several

factors and conditions susceptible to affect the accuracy of the measurement. The influence of belt position and displacements on the accuracy of the measurement of CO have also been described and quantified. We have laid the foundation for future investigations, and identified the clinical perspectives and main challenges ahead in the EIT-based measurement of CO.

On the other hand, this thesis has proposed a novel non-invasive method for the EIT-based measurement of PAP. We have developed a 4D model of the human thorax and demonstrated the validity of our approach in various pulmonary hypertensive disorders. We have explained its capability of being a stronger predictor of outcomes than PAP itself due to its high sensitivity to small pressure changes in mild to moderate pulmonary hypertension. Finally, we have demonstrated the validity of our method *in vivo*, thereby paving the way for the development of a new branch of non-invasive PAP monitors based on the use of EIT.

A Anatomical and circulatory models of the pulmonary arterial tree

The 4D bioimpedance model of the pulmonary arterial tree created in the present thesis is based on the junction of two models:

- a) A 3D anatomical model of the pulmonary arterial tree;
- b) A 1D circulatory model of the pulmonary circulation.

In Section A.1, we present the algorithm on which our method for the creation of the 3D geometrical model is based. In Section A.2, we introduce two circulatory models, our circulatory model being based on the junction of both.

A.1 Anatomical model

A.1.1 Volume-filling branching algorithm

Let us suppose that we segment CT scans to extract the outer contour of the lungs and the major pulmonary arteries of a subject. The limited resolution of medical imagery techniques does not allow the segmentation of the entire pulmonary arterial tree. It is therefore necessary to “generate” the remaining arteries in an automatic manner. In other terms, if the incomplete imagery-obtained tree contains N terminal arterial segments, the remainder of the tree can be grown in the unoccupied pulmonary volume by using these N terminal segments as seed points for the tree growing procedure. This is the principle behind the so-called *volume-filling branching* algorithm proposed by Burrowes *et al* [28]. Its working principle is explained in detail in Figure A.1.

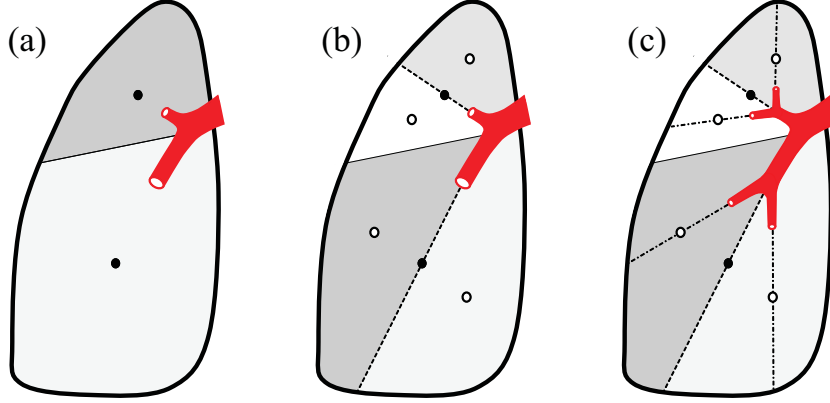


Figure A.1 – Schematic illustration of the volume-filling branching algorithm [28] with $N = 2$ terminal arterial segments. (a) The pulmonary cavities are filled with a uniform 3D grid of points (not shown). Each grid point is assigned to the closest terminal segment, resulting in N clusters of points (separated by the straight line in the figure). The center of mass of each cluster is calculated (black dots). (b) Each cluster is divided into two subclusters using the plan (here, a dashed line) that contains its center of mass and the terminal segment it is assigned to, resulting in a total of $2N$ subclusters. The center of mass of each subcluster is calculated (white dots). (c) The, the two daughter arteries of each terminal segment are generated by connecting its extremity to the centers of mass of the two corresponding subclusters and by stopping at 40 % of the distance. The $2N$ newly generated arterial segments are then considered as the new terminal segments, and the whole procedure can start all over again. The procedure stops for a given terminal segment when its length goes below a predefined threshold l_{\min} or when the cluster it is assigned to contains less than two grid points.

A.1.2 Geometry and morphometry of the tree

Although the length and the spatial distribution of the arteries in the volume of the lungs are determined by the volume-filling branching algorithm itself, their radius is not. The relationship between the radiuses r_{d_1} and r_{d_2} of two sister arteries with the radius r_p of their parent artery is controlled by three parameters, namely an asymmetry ratio γ , an area ratio η and a branching ratio ξ [123]:

$$\gamma = \frac{r_{d_2}^2}{r_{d_1}^2}, \quad \eta = \frac{r_{d_1}^2 + r_{d_2}^2}{r_p^2}, \quad r_p^\xi = r_{d_1}^\xi + r_{d_2}^\xi. \quad (\text{A.1})$$

These parameters are not independent as:

$$\eta = \frac{1 + \gamma}{(1 + \gamma^{\xi/2})^{2/\xi}}. \quad (\text{A.2})$$

From (A.1) it follows:

$$r_{d_1} = r_p \cdot (1 + \gamma^{\xi/2})^{-1/\xi}, \quad r_{d_2} = r_{d_1} \cdot \sqrt{\gamma}. \quad (\text{A.3})$$

Thus, as the radiuses of the first arteries of the tree are known (by imaging), it is possible to deduce iteratively the radiuses of all arteries in the tree, provided that γ , η and ξ are known as well. The values of these parameters are adjusted such that the morphometry of the generated tree matches that of actual pulmonary arterial trees.

Another important geometrical aspect of the arteries is their tapering (radius narrowing along their length), a characteristic that is particularly significant in the larger pulmonary arteries [123, 154]. Their tapering follows an exponential curve of the form [124]:

$$r(x) = r_{in} \cdot \exp(-kx), \quad (\text{A.4})$$

where $k = \ln(r_{out}/r_{in})/l$ is the tapering factor, r_{in} and r_{out} are the radiuses of the artery at its input and output, l is its length, and x is the location along the artery. The factor k is determined empirically using average values from morphometrical data of the pulmonary arteries [17, 124].

A.2 Circulatory models

As mentioned in the previous section, a 1D circulatory model of the pulmonary circulation is used in the present thesis. The purpose of so-called *1D distributed parameter models* is to describe the propagation and distribution of pressure and flow waves in the arterial tree. The main idea behind these models is to solve the Navier-Stokes equations describing the motion of a viscous fluid (blood) in tubes (arteries) as a function of pressure and flow in each arterial segment of the tree. Comparing the pulmonary arterial tree to a vast network of interconnected segments through which pressure and flow waves propagate, parallels with transmission line theory can be drawn, where:

- a) Each arterial segment is a transmission line and can be modeled using a longitudinal (fluid resistance and inertance) and a transverse (wall compliance) impedance (see Figure A.2);
- b) The pressure gradient across an arterial segment is analogous to electrical voltage;
- c) The flow running through the segment is analogous to electrical current.

The relationship between voltage and current in transmission line theory is described by the so-called Telegrapher's equations, which have analytical solutions in case of sinusoidal steady state. Thus, assuming the pressure gradient (voltage) and the flow

Appendix A. Anatomical and circulatory models of the pulmonary arterial tree

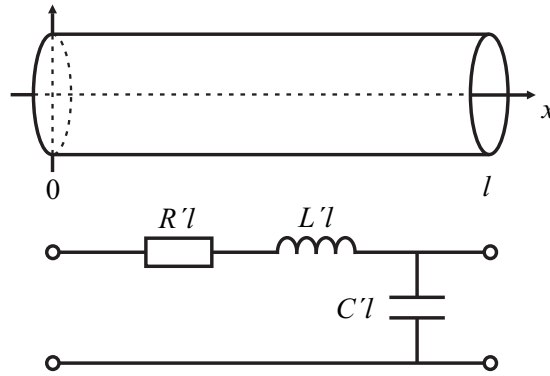


Figure A.2 – Upper panel: Model of a non-tapering arterial segment of length l . Lower panel: Electrical analog, with R' , L' and C' the electrical resistance, inductance and capacitance per unit length, respectively mimicking their hydraulic counterparts.

(current) to be periodic in the cardiovascular system, analytical solutions can be found for pressure and flow. However, this implies that each arterial segment can be represented as in Figure A.2, *i.e.* with uniform anatomical and structural properties (resistance, inertance, compliance) over the entire segment. This is not true in the larger pulmonary arteries, which – as mentioned earlier – taper significantly along their length. The tapering of the large arteries induces non-linear effects (convective acceleration), which prevent the direct use of transmission line theory [123]. Numerical approaches are therefore required to solve the Navier-Stokes equations in these segments of the tree. However, the aforementioned non-linear effects tend to become negligible at smaller scales [167]. Analytical solutions based on transmission line theory can therefore be used for the smaller arteries of the pulmonary tree, which is convenient as solving the problem numerically in the smaller vasculature becomes computationally infeasible due to the size of the tree [123].

We introduce hereafter the 1D distributed parameter model developed by Reymond [141] for the systemic circulation, and adapted by Billiet [17] for the pulmonary circulation. This model focuses on the larger segments of the arterial tree and uses a numerical solving scheme. We will then introduce the linearized model for the smaller arteries and its analytical solutions based on transmission line theory. In the present thesis, both model are jointly used to assess the distribution of pressure and flow in the entire pulmonary arterial tree.

A.2.1 Non-linear model for the large arteries

In 1D distributed parameter models for the large arteries such as Reymond's [141], the arteries are considered as long straight tapering segments of constant length l and time- and location-dependent cross-sectional area $A(x, t) = \pi R(x, t)^2$ (see Figure A.3). The blood running through the artery is subjected to a pressure $p(x, t)$ and flows at a rate

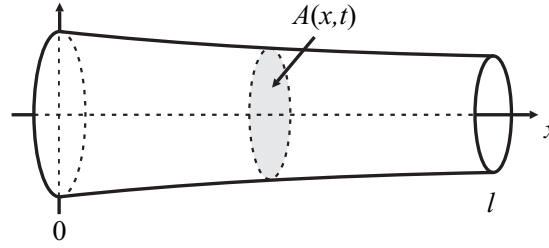


Figure A.3 – Model of a large arterial segment (tapering tube) of length l and cross-sectional area $A(x, t)$.

$q(x, t)$. Both quantities are assessed by solving the integral form of the continuity and x -momentum Navier-Stokes equations in each arterial segment [123, 141]:

$$\frac{\partial q}{\partial x} + \frac{\partial A}{\partial t} = 0, \quad (\text{A.5})$$

$$\frac{\partial q}{\partial t} + \frac{\partial}{\partial x} \left(\int_A u^2 dA \right) + \frac{A}{\rho} \frac{\partial p}{\partial x} - 2\pi R \mu \frac{\partial u}{\partial r} \Big|_{r=R} = 0, \quad (\text{A.6})$$

where μ and ρ are the dynamic viscosity and the density of blood, respectively. Both the convective acceleration term $\frac{\partial}{\partial x} \left(\int_A u^2 dA \right)$ and the wall shear stress term $\mu \frac{\partial u}{\partial r} \Big|_{r=R}$ depend on blood velocity $u(x, r, t)$, which is a priori unknown. In his model, Reymond uses *oscillatory flow theory* (see the next section) to obtain good approximations of these terms [141]. The system of equations (A.5+A.6) then only consists of three unknowns, namely pressure (p), flow (q) and arterial cross-sectional area (A). A so-called state equation describing the sensitivity of the cross-sectional area of an artery to a change in its distending pressure is used to complete the system [123]:

$$\frac{\partial A}{\partial p} = f(A, p), \quad (\text{A.7})$$

where $C' = \frac{\partial A}{\partial p}$ is a quantity known as area compliance (or capacitance per unit length) [180], and $f(\cdot)$ is an empirically-derived non-linear relation describing the viscoelastic properties of the arterial wall [17, 141]. The three-unknown system (A.5+A.6+A.7) is then solved numerically, using appropriate boundary conditions.

Boundary conditions. The concept of boundary conditions for 1D distributed parameter models is illustrated in Figure A.4. As *inflow* boundary condition, an “excitation” signal (typically a flow waveform) is inputted at the entry of the arterial tree. Alternatively, a pressure waveform or a model of the right ventricle (varying elastance model) can be used instead [141], but only one of them in order not to overdetermine the system [123].

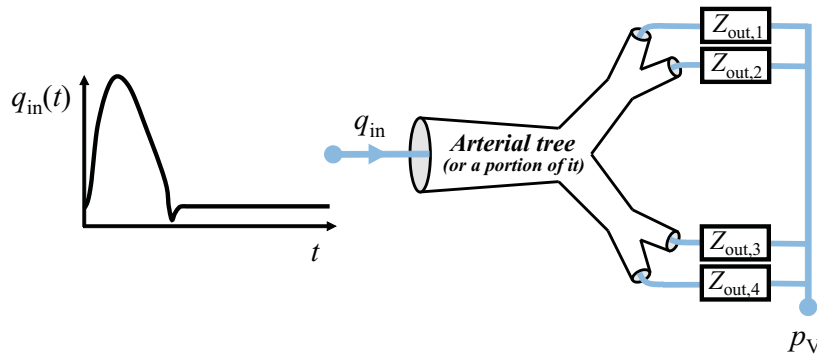


Figure A.4 – Boundary conditions for 1D distributed parameter models. As inflow boundary condition, a flow waveform (q_{in}) is typically used. As outflow boundary conditions, each terminal segment of the arterial tree is connected to an output impedance ($Z_{out,i}$) which mimics the hydraulic load “seen” beyond each segment down to venous pressure (p_v).

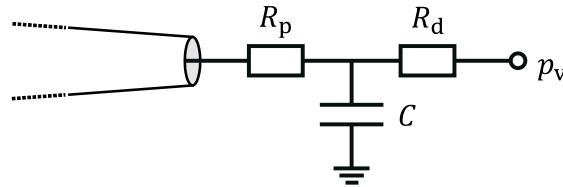


Figure A.5 – Electrical representation of the 3-element Windkessel (WK3) model. The WK3 model mimics the load “seen” downstream from a given arterial site. R_p is the so-called proximal resistance and represents the characteristic impedance of the arterial site [141]. R_d (the distal resistance) and C respectively represent the global resistance and compliance attributed to all peripheral arteries downstream of the site [179].

Reymond’s model can use both a flow waveform and a varying elastance model [141].

As outflow boundary conditions, a typical choice is the use of output impedances at the leaves of the tree [123]. Each impedance mimics the load “seen” beyond the arterial tree (or portion of the tree) under consideration. These impedances, referred to as zero-dimensional (lumped parameter) models, consist of resistive, capacitive and inertial components connected in series and parallel, by analogy with electrical circuit theory. One example is the 3-element Windkessel model (see Figure A.5), which consists of two resistive and a capacitive element, and is capable of accurately mimicking the cardiac afterload [179]. This is the choice made by Reymond in his model [141].

A.2.2 Linear model for the small arteries

For the small arteries, the complexity required for solving the aforementioned three-unknown system (A.5+A.6+A.7) becomes computationally infeasible due to the size of the arterial tree [123]. However, as smaller arteries do not taper significantly, the

convective acceleration term in the x -momentum Navier-Stokes equation (second term in (A.6)) becomes negligible [35, 154]. Furthermore the state equation (A.7) can be simplified [123]. The linearization of the governing equations becomes possible [123] and an analytical solution for pressure and flow can be found in every small arterial segment of the tree, as will be detailed hereafter. These solutions make heavy use of transmission line theory (by analogy with electrical circuits) and *oscillatory flow theory* (also known as Witzig-Womersley theory, or simply Womersley theory) [167].

Let us start with the simplification of the state equation (A.7). As small arterial segments do not taper, their cross-sectional area is constant. Neglecting viscoelastic effects [123], the area compliance $C' = \frac{\partial A}{\partial p}$ can be obtained using [180]:

$$C' = \delta A_0, \quad (\text{A.8})$$

where A_0 is the zero-pressure cross-sectional area of the arterial segment and δ is the distensibility of its wall. For the small arteries, the continuity equation (A.5) remains unchanged and can be merged with (A.8) since $\frac{\partial A}{\partial t} = \frac{\partial A}{\partial p} \frac{\partial p}{\partial t} = C' \frac{\partial p}{\partial t}$ [123, 181]:

$$\frac{\partial q}{\partial x} + C' \frac{\partial p}{\partial t} = 0. \quad (\text{A.9})$$

Furthermore, neglecting the convective acceleration term [35, 154], the linearized version of the x -momentum equation (A.6) can be rewritten as [123, 181]:

$$R' q + L' \frac{\partial q}{\partial t} + \frac{\partial p}{\partial x} = 0, \quad (\text{A.10})$$

where R' and L' are the fluid resistance and inertance per unit length, respectively. Based on pioneering work by Witzig [182], Womersley showed, in his *oscillatory flow theory*, that R' and L' are given by [181, 183]:

$$R' = \frac{\rho \omega}{A_0 M} \sin(\theta), \quad (\text{A.11})$$

$$L' = \frac{\rho}{A_0 M} \cos(\theta), \quad (\text{A.12})$$

where ω is the angular frequency. The quantities M and θ were defined by Womersley as follows:

$$Me^{i\theta} = 1 - \frac{2J_1(\alpha i^{3/2})}{\alpha i^{3/2} J_0(\alpha i^{3/2})}, \quad (\text{A.13})$$

Appendix A. Anatomical and circulatory models of the pulmonary arterial tree

where J_0 and J_1 are the zeroth and first order Bessel functions, $i = \sqrt{-1}$ is the imaginary unit, and α is the so-called Womersley number [167]. In an arterial segment of radius r_0 , $\alpha = r_0(\rho\omega/\mu)^{1/2}$.

Equations (A.9) and (A.10) are analogous to the Telegrapher's equations in transmission line theory, which describe the relationship between voltage and current along a transmission line [146]. The problem can be formulated in the frequency domain because of the pulsatile nature of pressure and flow waveforms. Let us first rewrite both equations:

$$\frac{\partial Q}{\partial x} + C'i\omega P = 0, \quad (\text{A.14})$$

$$Q(R' + i\omega L') + \frac{\partial P}{\partial x} = 0. \quad (\text{A.15})$$

where $P = P(x, \omega)$ and $Q = Q(x, \omega)$ are the complex Fourier series of $p(x, t)$ and $q(x, t)$, respectively. The sinusoidal steady-state solutions of the system of equations (A.14+A.15) are [146]:

$$P(x, \omega) = P(0, \omega) \left[\frac{Z(0, \omega) + Z_c}{2Z(0, \omega)} e^{-\gamma x} + \frac{Z(0, \omega) - Z_c}{2Z(0, \omega)} e^{\gamma x} \right], \quad (\text{A.16})$$

$$Q(x, \omega) = Q(0, \omega) \left[\frac{Z(0, \omega) + Z_c}{2Z_c} e^{-\gamma x} + \frac{Z_c - Z(0, \omega)}{2Z_c} e^{\gamma x} \right], \quad (\text{A.17})$$

where $Z(x, \omega) = P(x, \omega)/Q(x, \omega)$. The quantities Z_c and γ are the characteristic impedance and the propagation coefficient of the arterial segment, respectively. From transmission line theory, these two quantities are given by [146]:

$$Z_c = \sqrt{\frac{R' + i\omega L'}{i\omega C'}}, \quad (\text{A.18})$$

$$\gamma = \sqrt{i\omega C'(R' + i\omega L')}. \quad (\text{A.19})$$

The relation linking the input impedance $Z(0, \omega)$ of any arterial segment of length l to its output impedance $Z(l, \omega)$ is derived from transmission line theory by combining

equations (A.16) and (A.17). It follows that:

$$Z(0, \omega) = Z_c \frac{Z_c + Z(l, \omega) - [Z_c - Z(l, \omega)] e^{-2\gamma l}}{Z_c + Z(l, \omega) + [Z_c - Z(l, \omega)] e^{-2\gamma l}}. \quad (\text{A.20})$$

Furthermore, by analogy with electrical circuit theory, the relation linking the output impedance $Z(l, \omega)_p$ of a parent artery to the input impedances $Z(0, \omega)_{d_j}$ ($j = \{1, 2\}$) of its two daughters is given by:

$$\frac{1}{Z(l, \omega)_p} = \frac{1}{Z(0, \omega)_{d_1}} + \frac{1}{Z(0, \omega)_{d_2}}. \quad (\text{A.21})$$

Therefore, provided that proper outflow boundary conditions have been defined, as previously described for the large arteries, we can iteratively apply equations (A.20) and (A.21) and recursively compute the input and output impedances of all small arterial segments in the tree in a bottom-up fashion.

Finally, using an appropriate inflow boundary condition at the entry of the small arterial vasculature, such as flow or pressure waveforms, the distribution of pressure and flow in all small arterial segments can be obtained.

Bibliography

- [1] W. T. Abraham, et al. Wireless pulmonary artery haemodynamic monitoring in chronic heart failure: a randomised controlled trial. *Lancet*, 377(9766):658–666, 2011.
- [2] W. T. Abraham, P. B. Adamson, A. Hasan, R. C. Bourge, S. V. Pamboukian, M. F. Aaron, N. Y. Raval. Safety and accuracy of a wireless pulmonary artery pressure monitoring system in patients with heart failure. *Am. Heart J.*, 161(3):558–566, 2011.
- [3] P. B. Adamson. Pathophysiology of the transition from chronic compensated and acute decompensated heart failure: new insights from continuous monitoring devices. *Curr. Heart Fail. Rep.*, 6(4):287–292, 2009.
- [4] A. Adler and W. R. B. Lionheart. Uses and abuses of EIDORS: an extensible software base for EIT. *Physiol. Meas.*, 27(5):S25–S42, 2006.
- [5] A. Adler, et al. GREIT: a unified approach to 2D linear EIT reconstruction of lung images. *Physiol. Meas.*, 30(6):S35–S55, 2009.
- [6] A. Adler, et al. Whither lung EIT: Where are we, where do we want to go and what do we need to get there? *Physiol. Meas.*, 33(5):679–694, 2012.
- [7] A. Adler, R. Gaburro, W. Lionheart. Electrical impedance tomography. In: O. Scherzer (ed) *Handbook of mathematical methods in imaging*. Springer Science+Business Media. New York, USA, pp. 599–654, 2011.
- [8] A. Adler. Measurement of pulmonary function with electrical impedance tomography. Ph.D. dissertation. IGB, Montreal Univ., Montreal, Canada, 1995.
- [9] M. Afshar, F. Collado, R. Doukky. Pulmonary hypertension in elderly patients with diastolic dysfunction and preserved ejection fraction. *Open Cardiovasc. Med. J.*, 6:1–8, 2012.
- [10] Y. Allemann, C. Sartori, M. Lepori, S. Pierre, C. Mélot, R. Naeije, U. Scherrer, M. Maggiorini. Echocardiographic and invasive measurements of pulmonary artery pressure correlate closely at high altitude. *Am. J. Physiol.-Heart C.*, 279(4):H2013–H2016, 2000.

Bibliography

- [11] D. C. Barber and B. H. Brown. Applied potential tomography. *J. Phys. E: Sci. Instrum.*, 17(9):723–733, 1984.
- [12] R. Bayford. Bioimpedance tomography (electrical impedance tomography). *Annu. Rev. Biomed. Eng.*, 8:63–91, 2006.
- [13] R. Bayford and A. Tizzard. Bioimpedance imaging: an overview of potential clinical applications. *Analyst*, 137(20):4635–4643, 2012.
- [14] B. Bein, P. Meybohm, E. Cavus, J. Renner, P. H. Tonner, M. Steinfath, J. Scholz, V. Doerges. The reliability of pulse contour-derived cardiac output during hemorrhage and after vasopressor administration. *Anesth. Analg.*, 105(1):107–113, 2007.
- [15] R. L. Benza, et al. Pulmonary hypertension related to left heart disease: insight from a wireless implantable hemodynamic monitor. *J. Heart Lung Transpl.*, 34(3):329–337, 2015.
- [16] M. Berger, S. R. Hecht, A. van Tosh, U. Lingam. Pulsed and continuous wave Doppler echocardiographic assessment of valvular regurgitation in normal subjects. *J. Am. Coll. Cardiol.*, 13(7):1540–1545, 1989.
- [17] T. Billiet. Computational modeling of the hemodynamics in the pulmonary arterial tree: application to the human. M.S. thesis. Fac. Eng. Arch., Ghent Univ., Ghent, Belgium, 2009.
- [18] A. Bistoquet, J. Oshinski, O. Škrinjar. Myocardial deformation recovery from cine MRI using a nearly incompressible biventricular model. *Med. Image Anal.*, 12(1):69–85, 2008.
- [19] J. M. Bland and D. Altman. Statistical methods for assessing agreement between two methods of clinical measurement. *Lancet*, 327(8476):307–310, 1986.
- [20] L. Borcea. Electrical impedance tomography. *Inverse Probl.*, 18(6):R99–R136, 2002.
- [21] J. B. Borges, et al. Regional lung perfusion estimated by electrical impedance tomography in a piglet model of lung collapse. *J. Appl. Physiol.*, 112(1):225–236, 2012.
- [22] F. Braun, M. Proença, M. Rapin, M. Lemay, A. Adler, B. Grychtol, J. Solà, J.-Ph. Thiran. Aortic blood pressure measured via EIT: investigation of different measurement settings. *Physiol. Meas.*, 36(6):1147–1159, 2015.
- [23] F. Braun, M. Proença, B. Grychtol, A. Adler, J.-Ph. Thiran, J. Solà, F. Suarez-Sipmann, S. H. Böhm. Investigation on the origin of cardiogenic activity in electrical impedance tomography (EIT). In: *ESICM 2013 Annual Congress*. Paris, France, 2013.

- [24] F. Braun, et al. 4D heart model helps unveiling contributors to cardiac EIT signal. In: *EIT 2015 International Conference*. Neuchâtel, Switzerland, p. 107, 2015.
- [25] F. Braun, M. Proença, J. Solà, M. Lemay, J.-Ph. Thiran. EIT-derived stroke volume is impaired by belt displacement. In: *EIT 2016 International Conference*. Stockholm, Sweden, p. 74, 2016.
- [26] B. H. Brown, A. Leathard, A. Sinton, F. J. McArdle, R. W. Smith, D. C. Barber. Blood flow imaging using electrical impedance tomography. *Clin. Phys. Physiol. Meas.*, 13:175–179, 1992.
- [27] B. H. Brown, A. M. Sinton, D. C. Barber, A. D. Leathard, F. J. McArdle. Simultaneous display of lung ventilation and perfusion on a real-time EIT system. In: *IEEE EMBS 1992 Annual International Conference*. Paris, France, pp. 1710–1711, 1992.
- [28] K. S. Burrowes, P. J. Hunter, M. H. Tawhai. Anatomically based finite element models of the human pulmonary arterial and venous trees including supernumerary vessels. *J. Appl. Physiol.*, 99(2):731–738, 2005.
- [29] M. Carlsson, P. Cain, C. Holmqvist, F. Stahlberg, S. Lundback, H. Arheden. Total heart volume variation throughout the cardiac cycle in humans. *Am. J. Physiol.-Heart C.*, 287(1):H243–H250, 2004.
- [30] K. L. Chan, P. J. Currie, J. B. Seward, D. J. Hagler, D. D. Mair, A. D. Tajik. Comparison of three Doppler ultrasound methods in the prediction of pulmonary artery pressure. *J. Am. Coll. Cardiol.*, 9(3):549–554, 1987.
- [31] D. Chen, P. Pibarot, G. Honos, L. G. Durand. Estimation of pulmonary artery pressure by spectral analysis of the second heart sound. *Am. J. Cardiol.*, 78(7):785–789, 1996.
- [32] M. Cheney, D. Isaacson, J. C. Newell, S. Simske, J. Goble. NOSER: An algorithm for solving the inverse conductivity problem. *Int. J. Imaging Syst. Technol.*, 2(2):66–75, 1990.
- [33] Y. C. Chiu, P. W. Arand, S. G. Shroff, T. Feldman, J. D. Carroll. Determination of pulse wave velocities with computerized algorithms. *Am. Heart J.*, 121(5):1460–1470, 1991.
- [34] A. F. Connors, et al. The effectiveness of right heart catheterization in the initial care of critically ill patients. *Jama-J. Am. Med. Assoc.*, 276(11):889–897, 1996.
- [35] R. H. Cox. Wave propagation through a Newtonian fluid contained within a thick-walled, viscoelastic tube. *Biophys. J.*, 8(6):691–709, 1968.
- [36] L. A. H. Critchley. Minimally invasive cardiac output monitoring in the year 2012. In: W. S. Aronow (ed) *Artery bypass*. InTech. Rijeka, Croatia, pp. 45–80, 2013.

Bibliography

- [37] P. J. Currie, et al. Continuous wave Doppler determination of right ventricular pressure: a simultaneous Doppler-catheterization study in 127 patients. *J. Am. Coll. Cardiol.*, 6(4):750–756, 1985.
- [38] J. E. Dalen and R. C. Bone. Is it time to pull the pulmonary artery catheter? *Jama-J. Am. Med. Assoc.*, 276(11):916–918, 1996.
- [39] D. De Backer, et al. Comparison of dopamine and norepinephrine in the treatment of shock. *New Engl. J. Med.*, 362(9):779–789, 2010.
- [40] P. De Meester, A. Van De Bruaene, P. Herijgers, J. U. Voigt, W. Budts. Tricuspid valve regurgitation: prevalence and relationship with different types of heart disease. *Acta Cardiol.*, 67(5):549–556, 2012.
- [41] J. M. Deibele, H. Luepschen, S. Leonhardt. Dynamic separation of pulmonary and cardiac changes in electrical impedance tomography. *Physiol. Meas.*, 29(16):S1–S14, 2008.
- [42] D. Du Bois and E. F. Du Bois. A formula to estimate the approximate surface area if height and weight be known. 1916. *Nutrition*, 5(5):303–311, 1989.
- [43] P. Escribano-Subias, et al. Survival in pulmonary hypertension in Spain: insights from the Spanish registry. *Eur. Respir. J.*, 40(3):596–603, 2012.
- [44] D. Fagnoul, J. L. Vincent, D. De Backer. Cardiac output measurements using the bioreactance technique in critically ill patients. *Crit. Care*, 16(6):460, 2012.
- [45] D. Ferrario, B. Grychtol, A. Adler, J. Solà, S. H. Böhm, M. Bodenstein. Toward morphological thoracic EIT: major signal sources correspond to respective organ locations in CT. *IEEE T. Bio-Med. Eng.*, 59(11):3000–3008, 2012.
- [46] L. G. Fischer, H. Van Aken, H. Bürkle. Management of pulmonary hypertension: physiological and pharmacological considerations for anesthesiologists. *Anesth. Analg.*, 96(6):1603–1616, 2003.
- [47] K. R. Foster and H. C. Lukaski. Whole-body impedance – what does it measure? *Am. J. Clin. Nutr.*, 64(3):388S–396S, 1996.
- [48] R. P. Frantz, R. L. Benza, B. Kjellström, R. C. Bourge, R. J. Barst, T. D. Bennett, M. D. McGoon. Continuous hemodynamic monitoring in patients with pulmonary arterial hypertension. *J. Heart Lung Transpl.*, 27(7):780–788, 2008.
- [49] I. Frerichs, J. Hinz, P. Herrmann, G. Weisser, G. Hahn, M. Quintel, G. Hellige. Regional lung perfusion as determined by electrical impedance tomography in comparison with electron beam CT imaging. *IEEE T. Med. Imaging*, 21(6):646–652, 2002.

- [50] I. Frerichs, S. Pulletz, G. Elke, F. Reifferscheid, D. Schädler, J. Scholz, N. Weiler. Assessment of changes in distribution of lung perfusion by electrical impedance tomography. *Respiration*, 77(3):282–291, 2009.
- [51] I. Frerichs, T. Becher, N. Weiler. Electrical impedance tomography imaging of the cardiopulmonary system. *Curr. Opin. Crit. Care*, 20(3):323–332, 2014.
- [52] I. Frerichs, et al. Chest electrical impedance tomography examination, data analysis, terminology, clinical use and recommendations: consensus statement of the TRanslational EIT developmeNt stuDY group. *Thorax*, in press. Published Online First: 5 September 2016, doi: 10.1136/thoraxjnl-2016-208357, 2016.
- [53] F. M. Fruhwald, B. Kjellström, W. Perthold, N. Watzinger, R. Maier, P. A. Grandjean, W. Klein. Continuous hemodynamic monitoring in pulmonary hypertensive patients treated with inhaled iloprost. *Chest*, 124(1):351–359, 2003.
- [54] D. J. Funk, E. W. Moretti, T. J. Gan. Minimally invasive cardiac output monitoring in the perioperative setting. *Anesth. Analg.*, 108(3):887–897, 2009.
- [55] P. O. Gaggero. Miniaturization and distinguishability limits of electrical impedance tomography for biomedical application. Ph.D. dissertation no. 2207. LTF, Neuchâtel Univ., Neuchâtel, Switzerland, 2011.
- [56] N. Galiè, et al. 2015 ESC/ERS Guidelines for the diagnosis and treatment of pulmonary hypertension. *Eur. Heart J.*, 37(1):67–119, 2016.
- [57] R. M. Gardner. Direct blood pressure measurement - Dynamic response requirements. *Anesthesiology*, 54(3):227–236, 1981.
- [58] S. Ghio, et al. Independent and additive prognostic value of right ventricular systolic function and pulmonary artery pressure in patients with chronic heart failure. *J. Am. Coll. Cardiol.*, 37(1):183–188, 2001.
- [59] A. Graham and A. Adler. Objective selection of hyperparameter for EIT. *Physiol. Meas.*, 27(5):S65–S79, 2006.
- [60] C. A. Grant, T. Pham, J. Hough, T. Riedel, C. Stocker, A. Schibler. Measurement of ventilation and cardiac related impedance changes with electrical impedance tomography. *Crit. Care*, 15(1):R37, 2011.
- [61] B. M. Groves, et al. Operation Everest II: elevated high-altitude pulmonary resistance unresponsive to oxygen. *J. Appl. Physiol.*, 63(2):521–530, 1987.
- [62] B. Grychtol, W. R. B. Lionheart, M. Bodenstern, G. K. Wolf, A. Adler. Impact of model shape mismatch on reconstruction quality in electrical impedance tomography. *IEEE T. Med. Imaging*, 31(9):1754–1760, 2012.

Bibliography

- [63] B. Grychtol and A. Adler. FEM electrode refinement for electrical impedance tomography. In: *IEEE EMBS 2013 Annual International Conference*. Osaka, Japan, pp. 6429–6432, 2013.
- [64] M. Guazzi and B. A. Borlaug. Pulmonary hypertension due to left heart disease. *Circulation*, 126(8):975–990, 2012.
- [65] A. C. Guyton and J. E. Hall. *Textbook of medical physiology*. W. B. Saunders Company, 10th edn. Philadelphia, USA, 2010.
- [66] A. E. Hartinger, R. Guardo, A. Adler, H. Gagnon. Real-time management of faulty electrodes in electrical impedance tomography. *IEEE T. Bio-Med. Eng.*, 56(2):369–377, 2009.
- [67] S. Harvey, et al. Assessment of the clinical effectiveness of pulmonary artery catheters in management of patients in intensive care (PAC-Man): a randomised controlled trial. *Lancet*, 366(9484):472–477, 2005.
- [68] P. A. Hasgall, F. Di Gennaro, C. Baumgartner, E. Neufeld, M. C. Gosselin, D. Payne, A. Klingenböck, N. Kuster. IT'IS Database for thermal and electromagnetic parameters of biological tissues. Version 3.0, September 2015. Available: www.itis.ethz.ch/database, 2015.
- [69] G. Hellige and G. Hahn. Cardiac-related impedance changes obtained by electrical impedance tomography: an acceptable parameter for assessment of pulmonary perfusion? *Crit. Care*, 15:430, 2011.
- [70] R. P. Henderson and J. G. Webster. An impedance camera for spatially specific measurements of the thorax. *IEEE T. Bio-Med. Eng.*, 25(3):250–254, 1978.
- [71] D. A. Hett and M. M. Jonas. Non-invasive cardiac output monitoring. *Intensive Crit. Care Nurs.*, 20(2):103–108, 2004.
- [72] M. M. Hoeper and B. A. Borlaug. Chronic thromboembolic pulmonary hypertension. *Circulation*, 113(16):2011–2020, 2006.
- [73] D. S. Holder (ed). *Electrical impedance tomography: methods, history and applications*. Institute of Physics Publishing. Bristol, UK, 2005.
- [74] W. Huang, R. T. Yen, M. McLaurine, G. Bledsoe. Morphometry of the human pulmonary vasculature. *J. Appl. Physiol.*, 81(5):2123–2133, 1996.
- [75] M. Humbert, et al. Pulmonary arterial hypertension in France: results from a national registry. *Am. J. Resp. Crit. Care*, 173(9):1023–1030, 2006.
- [76] F. Ichinose, J. D. Roberts, W. M. Zapol. Inhaled nitric oxide: a selective pulmonary vasodilator: current uses and therapeutic potential. *Circulation*, 109(25):3106–3111, 2004.

- [77] IEC 60601-1:2005. *Medical Electrical Equipment – Part 1: General Requirements for Basic Safety and Essential Performance*. International Electrotechnical Commission (IEC), Geneva, Switzerland, 2005.
- [78] R. S. Irwin and J. M. Rippe (eds). *Irwin and Rippe's intensive care medicine*. Lippincott Williams & Wilkins, 6th edn. Philadelphia, USA, 2008.
- [79] M. B. Jaffe. Partial CO₂ rebreathing cardiac output–operating principles of the NICO™ system. *J. Clin. Monitor. Comp.*, 15(6):387–401, 1999.
- [80] J. R. C. Jansen, J. J. Schreuder, J. J. Settels, J. J. Kloek, A. Versprille. An adequate strategy for the thermodilution technique in patients during mechanical ventilation. *Intensive Care Med.*, 16(7):422–425, 1990.
- [81] P. Kauppinen, J. Hyttinen, J. Malmivuo. Sensitivity distribution simulations of impedance tomography electrode combinations. *IJBEM*, 7(1):344–347, 2005.
- [82] L. L. Kee, J. S. Simonson, N. A. Stotts, P. Skov, N. B. Schiller. Echocardiographic determination of valid zero reference levels in supine and lateral positions. *Am. J. Crit. Care*, 2(1):72–80, 1993.
- [83] T. Kenner, H. Leopold, H. Hinghofer-Szalkay. The continuous high-precision measurement of the density of flowing blood. *Pflug. Arch.*, 370(1):25–29, 1977.
- [84] D. W. Kim, L. E. Baker, J. A. Pearce, W. K. Kim. Origins of the impedance change in impedance cardiography by a three-dimensional finite element model. *IEEE T. Bio-Med. Eng.*, 35(12):993–1000, 1988.
- [85] A. Kitabatake, et al. Noninvasive evaluation of pulmonary hypertension by a pulsed Doppler technique. *Circulation*, 68(2):302–309, 1983.
- [86] R. Klabunde. *Cardiovascular physiology concepts*. Lippincott Williams & Wilkins, 2nd edn. Baltimore, USA, 2011.
- [87] M. Y. Koledintseva, R. E. DuBroff, R. W. Schwartz. A Maxwell Garnett model for dielectric mixtures containing conducting particles at optical frequencies. *Prog. Electromagn. Res.*, 63:223–242, 2006.
- [88] G. Kovacs, A. Berghold, S. Scheidl, H. Olschewski. Pulmonary arterial pressure during rest and exercise in healthy subjects: a systematic review. *Eur. Respir. J.*, 34(4):888–894, 2009.
- [89] G. Kovacs, A. Avian, A. Olschewski, H. Olschewski. Zero reference level for right heart catheterisation. *Eur. Respir. J.*, 42(6):1586–1594, 2013.
- [90] G. S. Krenz and C. A. Dawson. Flow and pressure distributions in vascular networks consisting of distensible vessels. *Am. J. Physiol.-Heart C.*, 284(6):H2192–H2203, 2003.

Bibliography

- [91] E. Kupersztych-Hagege, J. L. Teboul, A. Artigas, A. Talbot, C. Sabatier, C. Richard, X. Monnet. Bioreactance is not reliable for estimating cardiac output and the effects of passive leg raising in critically ill patients. *Brit. J. Anaesth.*, 111(6):961–966, 2013.
- [92] Y. C. Lai, K. C. Potoka, H. C. Champion, A. L. Mora, M. T. Gladwin. Pulmonary arterial hypertension: the clinical syndrome. *Circ. Res.*, 115(1):115–130, 2014.
- [93] J. W. Lankhaar, N. Westerhof, T. J. Faes, K. M. Marques, J. T. Marcus, P. E. Postmus, A. Vonk-Noordegraaf. Quantification of right ventricular afterload in patients with and without pulmonary hypertension. *Am. J. Physiol.-Heart C.*, 291(4):H1731–H1737, 2006.
- [94] J. W. Lankhaar, et al. Pulmonary vascular resistance and compliance stay inversely related during treatment of pulmonary hypertension. *Eur. Heart J.*, 29(13):1688–1695, 2008.
- [95] E. M. Lau, A. Manes, D. S. Celermajer, N. Galiè. Early detection of pulmonary vascular disease in pulmonary arterial hypertension: time to move forward. *Eur. Heart J.*, 32(20):2489–2498, 2011.
- [96] E. M. Lau, N. Iyer, R. Ihsar, B. P. Bailey, M. R. Adams, D. S. Celermajer. Abnormal pulmonary artery stiffness in pulmonary arterial hypertension: in vivo study with intravascular ultrasound. *PLoS One*, 7(3):e33331, 2012.
- [97] J. R. Levick. *An introduction to cardiovascular physiology*. Hodder Arnold, 5th edn. London, UK, 2010.
- [98] M. L. Lewis and L. C. Christianson. Behavior of the human pulmonary circulation during head-up tilt. *J. Appl. Physiol.*, 45(2):249–254, 1978.
- [99] C. Leys, C. Ley, O. Klein, P. Bernard, L. Licata. Detecting outliers: do not use standard deviation around the mean, use absolute deviation around the median. *J. Exp. Soc. Psychol.*, 49(4):764–766, 2013.
- [100] W. R. B. Lionheart. EIT reconstruction algorithms: pitfalls, challenges and recent developments. *Physiol. Meas.*, 25(1):125–142, 2004.
- [101] M. Maggiorini, et al. High-altitude pulmonary edema is initially caused by an increase in capillary pressure. *Circulation*, 103(16):2078–2083, 2001.
- [102] S. Mahapatra, R. A. Nishimura, P. Sorajja, S. Cha, M. D. McGoan. Relationship of pulmonary arterial capacitance and mortality in idiopathic pulmonary arterial hypertension. *J. Am. Coll. Cardiol.*, 47(4):799–803, 2006.
- [103] B. Maisch, et al. Guidelines on the diagnosis and management of pericardial diseases executive summary: the task force on the diagnosis and management of pericardial diseases of the European Society of Cardiology. *Eur. Heart J.*, 25(7):587–610, 2004.

- [104] S. Maisch, et al. Heart-lung interactions measured by electrical impedance tomography. *Crit. Care Med.*, 39(9):2173–2176, 2011.
- [105] J. Malmivuo and R. Plonsey. Impedance tomography. In: *Bioelectromagnetism: principles and applications of bioelectric and biomagnetic fields*. Oxford University Press. New York, USA, pp. 420–426, 1995.
- [106] P. E. Marik. Noninvasive cardiac output monitors: a state-of-the-art review. *J. Cardiothorac. Vasc. Anesth.*, 27(1):121–134, 2013.
- [107] P. E. Marik. Obituary: pulmonary artery catheter 1970 to 2013. *Ann. Intensive Care*, 3:38, 2013.
- [108] T. Masuyama, K. Kodama, A. Kitabatake, H. Sato, S. Nanto, M. Inoue. Continuous-wave Doppler echocardiographic detection of pulmonary regurgitation and its application to noninvasive estimation of pulmonary artery pressure. *Circulation*, 74(3):484–492, 1986.
- [109] J. P. Mathew and M. F. Newman. Hemodynamic and related monitoring. In: F. G. Estafanous, P. G. Barash, J. G. Reves (eds) *Cardiac anesthesia: principles and clinical practice*. Lippincott Williams & Wilkins, 2nd edn. Philadelphia, USA, pp. 195–236, 2001.
- [110] B. H. McGhee and E. J. Bridges. Monitoring arterial blood pressure: what you may not know. *Crit. Care Nurse*, 22(2):60–79, 2002.
- [111] M. D. McGoon and G. C. Kane. Pulmonary hypertension: diagnosis and management. *Mayo Clin. Proc.*, 84(2):191–207, 2009.
- [112] B. M. McQuillan, M. H. Picard, M. Leavitt, A. E. Weyman. Clinical correlates and reference intervals for pulmonary artery systolic pressure among echocardiographically normal subjects. *Circulation*, 104(23):2797–2802, 2001.
- [113] F. Meyer. Topographic distance and watershed lines. *Signal Process.*, 38(1):113–125, 1994.
- [114] W. R. Milnor, C. R. Conti, K. B. Lewis, M. F. O'Rourke. Pulmonary arterial pulse wave velocity and impedance in man. *Circ. Res.*, 25(6):637–649, 1969.
- [115] W. R. Milnor. *Hemodynamics*. Lippincott Williams & Wilkins, 2nd edn. Baltimore, USA, p. 148, 1989.
- [116] X. Monnet, M. Rienzo, D. Osman, N. Anguel, C. Richard, M. R. Pinsky, J. L. Teboul. Passive leg raising predicts fluid responsiveness in the critically ill. *Crit. Care Med.*, 34(5):1402–1407, 2006.

Bibliography

- [117] R. Mukkamala, J. O. Hahn, O. T. Inan, L. K. Mestha, C. S. Kim, H. Toreyin, S. Kyal. Towards ubiquitous blood pressure monitoring via pulse transit time: theory and practice. *IEEE T. Bio-Med. Eng.*, 62(8):1879–1901, 2015.
- [118] N. Nagaya, M. Ando, H. Oya, Y. Ohkita, S. Kyotani, F. Sakamaki, N. Nakanishi. Plasma brain natriuretic peptide as a noninvasive marker for efficacy of pulmonary thromboendarterectomy. *Ann. Thorac. Surg.*, 74(1):180–184, 2002.
- [119] J. H. Newman and A. R. Hemnes. Pulmonary hypertension. In: D. E. Schraufnagel (ed) *Breathing in America: diseases, progress, and hope*. American Thoracic Society. New York, USA, pp. 175–184, 2010.
- [120] D. T. Nguyen, C. Jin, A. Thiagalingam, A. L. McEwan. A review on electrical impedance tomography for pulmonary perfusion imaging. *Physiol. Meas.*, 33(5):695–706, 2012.
- [121] W. W. Nichols and M. F. O'Rourke. *McDonald's blood flow in arteries: theoretical, experimental and clinical principles*. Hodder Arnold, 5th edn. London, UK, 2005.
- [122] P. Nopp, E. Rapp, H. Pfutzner, H. Nakesch, C. Rusham. Dielectric properties of lung tissue as a function of air content. *Phys. Med. Biol.*, 38(6):699–716, 1993.
- [123] M. S. Olufsen. Modeling flow and pressure in the systemic arteries. In: *Applied mathematical models in human physiology*. SIAM. Philadelphia, USA, pp. 91–136, 2004.
- [124] M. S. Olufsen. Modeling the arterial system with reference to an anesthesia simulator. Ph.D. dissertation no. 345. IMFUFA, Roskilde Univ., Roskilde, Denmark, 1998.
- [125] N. Otsu. A threshold selection method from gray-level histograms. *IEEE Trans. Syst. Man Cybern.*, 9(1):62–66, 1979.
- [126] R. P. Patterson. Sources of the thoracic cardiogenic electrical impedance signal as determined by a model. *Med. Biol. Eng. Comput.*, 23(5):411–417, 1985.
- [127] R. P. Patterson. Impedance cardiography: what is the source of the signal? *J. Phys. Conf. Ser.*, 224:012118, 2010.
- [128] J. Pepke-Zaba, et al. Chronic thromboembolic pulmonary hypertension (CTEPH): results from an international prospective registry. *Circulation*, 124(18):1973–1981, 2011.
- [129] R. Pikkemaat, S. Lundin, O. Stenqvist, R. D. Hilgers, S. Leonhardt. Recent advances in and limitations of cardiac output monitoring by means of electrical impedance tomography. *Anesth. Analg.*, 119(1):76–83, 2014.

- [130] R. Pikkemaat. Kardiopulmonales Monitoring mit Hilfe der elektrischen Impedanztomographie. Ph.D. dissertation. MedIT, RWTH Aachen Univ., Aachen, Germany, 2015.
- [131] M. R. Pinsky and D. Payen (eds). *Functional hemodynamic monitoring*. Springer Science+Business Media. Heidelberg, Germany, 2005.
- [132] T. R. Porter, S. K. Shillcutt, M. S. Adams, G. Desjardins, K. E. Glas, J. J. Olson, R. W. Troughton. Guidelines for the use of echocardiography as a monitor for therapeutic intervention in adults: a report from the American Society of Echocardiography. *J. Am. Soc. Echocardiogr.*, 28(1):40–56, 2015.
- [133] M. Proença, et al. Influence of heart motion on cardiac output estimation by means of electrical impedance tomography: a case study. *Physiol. Meas.*, 36(6):1075–1091, 2015.
- [134] M. Proença, F. Braun, J. Solà, A. Adler, M. Lemay, J.-Ph. Thiran, S. F. Rimoldi. Non-invasive monitoring of pulmonary artery pressure from timing information by EIT: experimental evaluation during induced hypoxia. *Physiol. Meas.*, 37(6):713–726, 2016.
- [135] M. Proença, F. Braun, M. Rapin, J. Solà, M. Lemay, J.-Ph. Thiran. Feasibility of EIT-based pulmonary arterial pressure monitoring. In: *EIT 2015 International Conference*. Neuchâtel, Switzerland, p. 108, 2015.
- [136] M. Proença, F. Braun, J. Solà, J.-Ph. Thiran, M. Lemay. Noninvasive pulmonary artery pressure monitoring by EIT: a model-based feasibility study. *Med. Biol. Eng. Comput.*, in press. Published Online First: 17 September 2016, doi: 10.1007/s11517-016-1570-1, 2016.
- [137] M. U. Qureshi, G. D. Vaughan, C. Sainsbury, M. Johnson, C. S. Peskin, M. S. Olufsen, N. A. Hill. Numerical simulation of blood flow and pressure drop in the pulmonary arterial and venous circulation. *Biomed. Model. Mechan.*, 13(5):1137–1154, 2014.
- [138] E. Raaijmakers, J. T. Marcus, H. G. Goovaerts, P. M. J. M. de Vries, T. J. C. Faes, R. M. Heethaar. The influence of pulsatile flow on blood resistivity in impedance cardiography. In: *IEEE EMBS 1996 Annual International Conference*. Amsterdam, The Netherlands, pp. 1957–1958, 1996.
- [139] R. M. Rangayyan. Filtering for removal of artifacts. In: *Biomedical signal analysis: a case-study approach*. Wiley. Ney York, USA, pp. 73–173, 2002.
- [140] A. Rashid, B. S. Kim, A. K. Khambampati, D. Liu, S. Kim, K. Y. Kim. Dynamic boundary estimation of human heart within a complete cardiac cycle using electrical impedance tomography. *J. Phys. Conf. Ser.*, 224(1):012042, 2010.

Bibliography

- [141] Ph. Reymond. Pressure and flow wave propagation in patient-specific models of the arterial tree. Ph.D. dissertation no. 5029. LHTC, EPFL, Lausanne, Switzerland, 2011.
- [142] S. Rich, G. E. D’Alonzo, D. R. Dantzker, P. S. Levy. Magnitude and implications of spontaneous hemodynamic variability in primary pulmonary hypertension. *Am. J. Cardiol.*, 55(1):159–163, 1985.
- [143] C. Richard, et al. Early use of the pulmonary artery catheter and outcomes in patients with shock and acute respiratory distress syndrome: a randomized controlled trial. *Jama-J. Am. Med. Assoc.*, 290(20):2713–2720, 2003.
- [144] J. Rosell, J. Colominas, P. Riu, R. Pallas-Areny, J. G. Webster. Skin impedance from 1 Hz to 1 MHz. *IEEE T. Bio-Med. Eng.*, 35(8):649–651, 1988.
- [145] C. J. Roth, A. Ehrl, T. Becher, I. Frerichs, J. C. Schittny, N. Weiler, W. A. Wall. Correlation between alveolar ventilation and electrical properties of lung parenchyma. *Physiol. Meas.*, 36(6):1211–1226, 2015.
- [146] M. N. O. Sadiku. Transmission lines. In: *Elements of Electromagnetics*. Oxford University Press. Oxford, UK, pp. 473–541, 2001.
- [147] J. D. Sandham, et al. A randomized, controlled trial of the use of pulmonary-artery catheters in high-risk surgical patients. *New Engl. J. Med.*, 348(1):5–14, 2003.
- [148] J. Sanz, M. Kariisa, S. Dellegrottaglie, S. Prat-González, M. J. Garcia, V. Fuster, S. Rajagopalan. Evaluation of pulmonary artery stiffness in pulmonary hypertension with cardiac magnetic resonance. *JACC Cardiovasc. Imaging*, 2(3):286–295, 2009.
- [149] N. Saouti, N. Westerhof, P. E. Postmus, A. Vonk-Noordegraaf. The arterial load in pulmonary hypertension. *Eur. Respir. Rev.*, 19(117):197–203, 2010.
- [150] N. Saouti, N. Westerhof, F. Helderma, T. J. Marcus, A. Boonstra, P. E. Postmus, A. Vonk-Noordegraaf. Right ventricular oscillatory power is a constant fraction of total power irrespective of pulmonary artery pressure. *Am. J. Resp. Crit. Care*, 182(10):1315–1320, 2010.
- [151] T. Schlebusch, S. Nienke, S. Leonhardt, M. Walter. Bladder volume estimation from electrical impedance tomography. *Physiol. Meas.*, 35(9):1813–1823, 2014.
- [152] D. P. Schuster, C. Anderson, J. Kozlowski, N. Lange. Regional pulmonary perfusion in patients with acute pulmonary edema. *J. Nucl. Med.*, 43(7):863–870, 2002.
- [153] J. N. Shephard, S. J. Brecker, T. W. Evans. Bedside assessment of myocardial performance in the critically ill. *Intensive Care Med.*, 20(7):513–521, 1994.
- [154] Y. Shi, P. Lawford, R. Hose. Review of zero-D and 1-D models of blood flow in the cardiovascular system. *Biomed. Eng. Online*, 10(33):1–38, 2011.

- [155] H. J. Smit, A. Vonk-Noordegraaf, A. Boonstra, P. M. de Vries, P. E. Postmus. Assessment of the pulmonary volume pulse in idiopathic pulmonary arterial hypertension by means of electrical impedance tomography. *Respiration*, 73(5):597–602, 2006.
- [156] R. Smith and D. Ventura. A general model for continuous noninvasive pulmonary artery pressure estimation. *Comput. Biol. Med.*, 43(7):904–913, 2013.
- [157] J. Solà, A. Adler, A. Santos, G. Tusman, F. Suarez-Sipmann, S. H. Böhm. Non-invasive monitoring of central blood pressure by electrical impedance tomography: first experimental evidence. *Med. Biol. Eng. Comput.*, 49(4):409–415, 2011.
- [158] J. Solà, S. F. Rimoldi, Y. Allemann. Ambulatory monitoring of the cardiovascular system: the role of pulse wave velocity. In: *New developments in biomedical engineering*. InTech. Rijeka, Croatia, pp. 391–424, 2010.
- [159] J. Solà, A. Adler, J. X. Brunner, D. Ferrario, M. Proença. Method and apparatus for the non-invasive measurement of pulse transit times (PTT). *European Patent*. EP2593006 B1, 4th Dec. 2013.
- [160] G. Strange, D. Playford, S. Stewart, J. A. Deague, H. Nelson, A. Kent, E. Gabbay. Pulmonary hypertension: prevalence and mortality in the Armadale echocardiography cohort. *Heart*, 98(24):1805–1811, 2012.
- [161] B. C. Su, Y. F. Tsai, C. Y. Chen, H. P. Yu, M. W. Yang, W. C. Lee, C. C. Lin. Cardiac output derived from arterial pressure waveform analysis in patients undergoing liver transplantation: validity of a third-generation device. *Transpl. P.*, 44(2):424–428, 2012.
- [162] H. J. C. Swan, W. Ganz, J. Forrester, H. Marcus, G. Diamond, D. Chonette. Catheterization of the heart in man with use of a flow-directed balloon-tipped catheter. *New Engl. J. Med.*, 283(9):447–451, 1970.
- [163] R. Syyed, J. T. Reeves, D. Welsh, D. Raeside, M. K. Johnson, A. J. Peacock. The relationship between the components of pulmonary artery pressure remains constant under all conditions in both health and disease. *Chest*, 133(3):633–639, 2008.
- [164] R. J. Tedford, et al. Pulmonary capillary wedge pressure augments right ventricular pulsatile loading. *Circulation*, 125(2):289–297, 2012.
- [165] M. Ulbrich, J. Mühlsteff, S. Leonhardt, M. Walter. Influence of physiological sources on the impedance cardiogram analyzed using 4D FEM simulations. *Physiol. Meas.*, 35(7):1451–1468, 2014.
- [166] S. R. Underwood, C. R. Gill, D. N. Firmin, R. H. Klipstein, R. H. Mohiaddin, R. S. Rees, D. B. Longmore. Left ventricular volume measured rapidly by oblique magnetic resonance imaging. *Br. Heart J.*, 60(3):188–195, 1988.

Bibliography

- [167] F. N. van de Vosse and N. Stergiopoulos. Pulse wave propagation in the arterial tree. *Annu. Rev. Fluid Mech.*, 43:467–499, 2011.
- [168] M. Vauhkonen, D. Vadasz, P. A. Karjalainen, E. Somersalo, J. P. Kaipio. Tikhonov regularization and prior information in electrical impedance tomography. *IEEE T. Med. Imaging*, 17(2):285–293, 1998.
- [169] J. L. Vincent and D. De Backer. Circulatory shock. *New Engl. J. Med.*, 369(18):1726–1734, 2013.
- [170] I. K. R. Visser. Electric properties of flowing blood and impedance cardiography. *Ann. Biomed. Eng.*, 17(5):463–473, 1989.
- [171] A. Vonk-Noordegraaf, T. J. C. Faes, A. Janse, J. T. Marcus, R. M. Heethaar, P. E. Postmus, P. M. J. M. de Vries. Improvement of cardiac imaging in electrical impedance tomography by means of a new electrode configuration. *Physiol. Meas.*, 17(3):179–188, 1996.
- [172] A. Vonk-Noordegraaf, P. W. A. Kunst, A. Janse, R. A. Smulders, R. M. Heethaar, P. E. Postmus, T. J. C. Faes, P. M. J. M. de Vries. Validity and reproducibility of electrical impedance tomography for measurement of calf blood flow in healthy subjects. *Med. Biol. Eng. Comput.*, 35(2):107–112, 1997.
- [173] A. Vonk-Noordegraaf, P. W. A. Kunst, A. Janse, J. T. Marcus, P. E. Postmus, T. J. C. Faes, P. M. J. M. de Vries. Pulmonary perfusion measured by means of electrical impedance tomography. *Physiol. Meas.*, 19(2):263–273, 1998.
- [174] A. Vonk-Noordegraaf, A. Janse, J. T. Marcus, J. G. F. Bronzwaer, P. E. Postmus, T. J. C. Faes, P. M. J. M. de Vries. Determination of stroke volume by means of electrical impedance tomography. *Physiol. Meas.*, 21(2):285–293, 2000.
- [175] L. Wang and R. P. Patterson. Multiple sources of the impedance cardiogram based on 3-D finite difference human thorax models. *IEEE T. Bio-Med. Eng.*, 42(2):141–148, 1995.
- [176] Z. J. Wang, G. P. Reddy, M. B. Gotway, B. M. Yeh, S. W. Hetts, C. B. Higgins. CT and MR imaging of pericardial disease. *Radiographics*, 23:S167–S180, 2003.
- [177] D. J. Wang and S. S. Gottlieb. Impedance cardiography: more questions than answers. *Curr. Heart Fail. Rep.*, 3(3):107–113, 2006.
- [178] J. B. West, R. B. Schoene, J. S. Milledge. High altitude pulmonary edema. In: *High altitude medicine and physiology*. Hodder Arnold, 4th edn. London, UK, pp. 279–298, 2007.
- [179] N. Westerhof, J. W. Lankhaar, B. E. Westerhof. The arterial windkessel. *Med. Biol. Eng. Comput.*, 47(2):131–141, 2009.

- [180] N. Westerhof, N. Stergiopoulos, M. I. M. Noble. *Snapshots of hemodynamics: an aid for clinical research and graduate education*. Springer Science+Business Media, 2nd edn. New York, USA, 2010.
- [181] F. Wiener, E. Morkin, R. Skalak, A. P. Fishman. Wave propagation in the pulmonary circulation. *Circ. Res.*, 19(4):834–850, 1966.
- [182] S. Witzig. Über erzwungene Wellenbewegungen zäher, inkompressibler Flüssigkeiten in elastischen Röhren. Ph.D. dissertation. Bern Univ., Bern, Switzerland, 1914.
- [183] J. R. Womersley. Method for the calculation of velocity, rate of flow and viscous drag in arteries when the pressure gradient is known. *J. Physiol.*, 127(3):553–563, 1955.
- [184] J. Xu, L. G. Durand, P. Pibarot. A new, simple, and accurate method for non-invasive estimation of pulmonary arterial pressure. *Heart*, 88(1):76–80, 2002.
- [185] S. Zlochiver, D. Freimark, M. Arad, A. Adunsky, S. Abboud. Parametric EIT for monitoring cardiac stroke volume. *Physiol. Meas.*, 27(5):S139–S146, 2006.

MARTIN PROENÇA

Private address

Martin Proença
Chemin des Epinettes 65
CH-1723 Marly
Tel: +41 79 399 74 06
E-mail: martin.proenca@gmail.com

Professional address

CSEM SA, Martin Proença
Jaquet-Droz 1
CH-2002 Neuchâtel
Tel: +41 32 720 54 10
E-mail: martin.proenca@csem.ch

Born in Fribourg, Switzerland, on the 17th of May 1986.
Single, Swiss citizenship.

RESEARCH INTERESTS

Application of signal processing and cardiovascular modeling techniques for the non-invasive estimation of central hemodynamic parameters.

EDUCATION

2012 – 2016

PhD Thesis in Electrical Engineering

Ecole Polytechnique Fédérale de Lausanne (EPFL), Lausanne, Switzerland
Centre Suisse d'Electronique et de Microtechnique (CSEM), Neuchâtel, Switzerland
PhD Thesis in industry under the supervision of Prof. Dr. Jean-Philippe Thiran (EPFL) and Dr. Mathieu Lemay (CSEM). Thesis title: “Non-invasive hemodynamic monitoring by electrical impedance tomography”.

2006 – 2011

Master of Science in Electrical Engineering

Major in Information Technology & Minor in Biomedical Technology (EPFL)
Master Thesis in industry under the supervision of Prof. Dr. Jean-Philippe Thiran (EPFL) and Dr. Josep Solà (CSEM). Thesis title: “Unsupervised identification of organs through thoracic electrical impedance tomography”.

PROFESSIONAL EXPERIENCE

2011 – present

R&D Biomedical Engineer, CSEM

Development of biomedical signal processing algorithms and hemodynamic models for the unsupervised estimation of cardiovascular parameters (such as pulmonary artery pressure, cardiac output, systemic blood pressure, oxygen saturation, or heart rate variability) by means of non-invasive modalities (such as electrical impedance tomography, photoplethysmography, impedance cardiography, or electrocardiography).

2010

Teaching Assistant, EPFL

Electrotechnics (for undergraduate students, Electrical Engineering section).

RESEARCH EXPERIENCE

- Grants* Acquisition of a three-year grant and a six-month supplementary grant from the Swiss National Science Foundation (“Subject-adapted 3D dynamic bio-impedance models: application to blood pressure monitoring”, no. 205321-153364).
- Clinical trials* Participation in data acquisition in clinical trials in and out of the operating room (“Etude de validation de l’utilisation de la mesure du débit cardiaque via tomographie par impédance électrique”, no. 2015-00203; “Non-invasive estimation of pulmonary artery pressure in healthy subjects by electrical impedance tomography”, no. 2016-00747), and in the design and description of a clinical study protocol (no. 2016-00747).
- Reviewing activity* Expert Review of Cardiovascular Therapy and EIT 2015 International Conference.

LANGUAGES

- French* Native language
English Advanced
German Intermediate

SKILLS

- IT* MATLAB, EIDORS, C/C++, OpenCV, Java, ImageJ, L^AT_EX

PUBLICATION LIST

JOURNAL PAPERS

- **Proença M.**, Braun F., Solà J., Adler A., Lemay M., Thiran J.-Ph., Rimoldi S.F., “Non-invasive monitoring of pulmonary artery pressure from timing information by EIT: experimental evaluation during induced hypoxia”, *Physiological Measurement*, vol. 37, no. 6, pp. 713-726, 2016
- **Proença M.**, Braun F., Solà J., Thiran J.-Ph., Lemay M., “Noninvasive pulmonary artery pressure monitoring by EIT: a model-based feasibility study”, *Medical & Biological Engineering & Computing*, in press, 2016. DOI: 10.1007/s11517-016-1570-1
- **Proença M.**, Braun F., Rapin M., Solà J., Adler A., Grychtol B., Böhm S.H., Lemay M., Thiran J.-Ph., “Influence of heart motion on cardiac output estimation by means of electrical impedance tomography: a case study”, *Physiological Measurement*, vol. 36, no. 6, pp. 1075-1091, 2015
- Braun F., **Proença M.**, Rapin M., Lemay M., Adler A., Grychtol B., Solà J., Thiran J.-Ph., “Aortic blood pressure measured via EIT: investigation of different measurement settings”, *Physiological Measurement*, vol. 36, no. 6, pp. 1147-1159, 2015
- Rapin M., **Proença M.**, Braun F., Meier C., Solà J., Ferrario D., Grossenbacher O., Porchet J.-A., Chételat O., “Cooperative dry-electrode sensors for multi-lead biopotential and bioimpedance monitoring”, *Physiological Measurement*, vol. 36, no. 4, pp. 767-783, 2015
- Solà J., **Proença M.**, Ferrario D., Porchet J.-A., Falhi A., Grossenbacher O., Allemann Y., Rimoldi S.F., “Non-invasive and non-occlusive blood pressure estimation via a chest sensor”, *IEEE Transactions on Biomedical Engineering*, vol. 60, no. 12, pp. 3505-3513, 2013

PATENTS

- **Proença M.**, Solà J., Lemay M., Verjus C., “Method, apparatus and computer program for determining a blood pressure value”, WO 2016 138965 A1, 9th of September 2016
- Dunki-Jacobs A., Harris J.L., Lemay M., Pfeleiderer M., **Proença M.**, Utard T., “Meal detection devices and methods”, WO 2014 163784 A1, 9th of October 2014
- Adler A., Brunner J.X., Ferrario D., Solà J., **Proença M.**, “Method and apparatus for the non-invasive measurement of Pulse Transit Times (PTT)”, WO 2012 007423 A1, 19th of January 2012

CONFERENCE PAPERS AND ABSTRACTS

- Solà J., **Proença M.**, Braun F., Pierrel N., Degiorgis Y., Verjus C., Lemay M., Bertschi M., Schoettker P., “Continuous non-invasive monitoring of blood pressure in the operating room: a cuffless optical technology at the fingertip”, *in* BMT 2016 Annual Conference, Basel, Switzerland
- **Proença M.**, Braun F., Muntané E., Solà J., Adler A., Lemay M., Thiran J.-Ph., Rimoldi S.F., “Non-invasive monitoring of pulmonary artery pressure at the bedside”, *in* IEEE EMBC 2016 Annual International Conference, Orlando, USA
- Solà J., **Proença M.**, Braun F., Muntané E., Verjus C., Lemay M., Schoettker P., Bertschi M., “Cuffless blood pressure monitoring: experimental evidences of a beat-to-beat PPG technique”, *in* IEEE EMBC 2016 Annual International Conference, Orlando, USA
- **Proença M.**, Braun F., Solà J., Adler A., Lemay M., Thiran J.-Ph., Rimoldi S.F., “Pulmonary artery pressure by EIT: experimental evaluation”, *in* EIT 2016 International Conference, Stockholm, Sweden
- Braun F., **Proença M.**, Solà J., Lemay M., Thiran J.-Ph., “EIT-derived stroke volume is sensitive to belt displacement”, *in* EIT 2016 International Conference, Stockholm, Sweden
- **Proença M.**, Braun F., Rapin M., Solà J., Lemay M., Thiran J.-Ph., “Feasibility of EIT-based pulmonary arterial pressure monitoring”, *in* EIT 2015 International Conference, Neuchâtel, Switzerland
- Braun F., **Proença M.**, Rapin M., Alba X., Lekadir K., Lemay M., Solà J., Frangi A., Thiran J.-Ph., “4D Heart Model Helps Unveiling Contributors to Cardiac EIT Signal”, *in* EIT 2015 International Conference, Neuchâtel, Switzerland
- Rapin M., **Proença M.**, Braun F., Solà J., Chételat O., “Cooperative sensors: a new approach towards wearable EIT systems”, *in* EIT 2015 International Conference, Neuchâtel, Switzerland
- **Proença M.**, Braun F., Rapin M., Solà J., Lemay M., Thiran J.-Ph., “Non-invasive pulmonary artery pressure monitoring: a pulse wave velocity approach”, *in* SSBE 2015 Annual Meeting, Neuchâtel, Switzerland. **Best Poster Award from the Swiss Society of Biomedical Engineering (SSBE)**
- Braun F., **Proença M.**, Rapin M., Alba X., Lekadir K., Lemay M., Solà J., Frangi A., Thiran J.-Ph., “Stroke volume measured via electrical impedance tomography (EIT): a simulation-based feasibility study”, *in* SSBE 2015 Annual Meeting, Neuchâtel, Switzerland

- Rapin M., Braun F., **Proença M.**, Wacker J., Chételat O., “Wearable 12-lead ECG monitoring system by means of cooperative sensors”, *in* SSBE 2015 Annual Meeting, Neuchâtel, Switzerland
- Chételat O., Ferrario D., **Proença M.**, Porchet J.-A., Falhi A., Grossenbacher O., Delgado-Gonzalo R., Della Ricca N., Sartori C., “Clinical validation of LTMS-S: a wearable system for vital signs monitoring”, *in* IEEE EMBC 2015 Annual International Conference, Milan, Italy
- **Proença M.**, Braun F., Lemay M., Grychtol B., Bühler M., Rapin M., Krammer P., Böhm S.H., Solà J., Thiran J.-Ph., “Understanding the genesis of cardiac signals in electrical impedance tomography”, *in* BIOSTEC 2014 International Conference, Angers, France
- **Proença M.**, Rapin M., Solà J., Lemay M., Thiran J.-Ph., “Cardiac output measured by electrical impedance tomography: applications and limitations”, *in* IEEE BioCAS 2014 International Conference, Lausanne, Switzerland
- **Proença M.**, Braun F., Rapin M., Solà J., Adler A., Grychtol B., Bühler M., Krammer P., Böhm S.H., Lemay M., Thiran J.-Ph., “Influence of heart motion on EIT-based stroke volume estimation”, *in* EIT 2014 International Conference, Gananoque, Canada
- Braun F., **Proença M.**, Rapin M., Grychtol B., Bühler M., Krammer P., Böhm S.H., Lemay M., Solà J., Thiran J.-Ph., “Comparing belt positions for monitoring the descending aorta by EIT”, *in* EIT 2014 International Conference, Gananoque, Canada
- Rapin M., **Proença M.**, Braun F., Solà J., Gaggero P.O., Adler A., Correvon M., Chételat O., “Discarding the Direct Component in Electrical Impedance Tomography”, *in* EIT 2014 International Conference, Gananoque, Canada
- **Proença M.**, Braun F., Rapin M., Solà J., Adler A., Grychtol B., Bühler M., Krammer P., Böhm S.H., Lemay M., Thiran J.-Ph., “Non-invasive stroke volume estimation via electrical impedance tomography: influence of heart motion”, *in* SSBE 2014 Annual Meeting, Zurich, Switzerland
- Braun F., **Proença M.**, Rapin M., Grychtol B., Bühler M., Krammer P., Böhm S.H., Lemay M., Solà J., Thiran J.-Ph., “Non-invasive blood pressure estimation via electrical impedance tomography (EIT): influence of belt position”, *in* SSBE 2014 Annual Meeting, Zurich, Switzerland
- Solà J., **Proença M.**, Chételat O., “Wearable PWV technologies to measure blood pressure: eliminating brachial cuffs”, *in* IEEE EMBC 2013 Annual International Conference, Osaka, Japan
- Braun F., **Proença M.**, Grychtol B., Adler A., Thiran J.-Ph., Solà J., Suarez-Sipmann F., Böhm S.H., “Investigation on the origin of cardiogenic activity in electrical impedance tomography (EIT)”, *in* ESICM 2013 Annual Congress, Paris, France
- **Proença M.**, Falhi A., Ferrario D., Grossenbacher O., Porchet J.-A., Krauss J., Solà J., “Continuous non-occlusive blood pressure monitoring at the sternum”, *in* BMT 2012 Annual Conference, Jena, Germany
- Solà J., **Proença M.**, Ferrario D., Porchet J.-A., Grossenbacher O., Chételat O., Bertschi M., Krauss J., “Continuous, non-invasive and non-occlusive blood pressure monitoring”, *in* SSBE 2012 Annual Meeting, Lausanne, Switzerland

